EXPERIMENTAL INVESTIGATION OF HOSPITAL OPERATING ROOM AIR DISTRIBUTION

A Thesis
Presented to
The Academic Faculty

by

Tyler C. Stevenson

In Partial Fulfillment
of the Requirements for the Degree
Masters of Science in the
School of Mechanical Engineering

Georgia Institute of Technology
May 2008

EXPERIMENTAL INVESTIGATION OF HOSPITAL OPERATING ROOM AIR DISTRIBUTION

Approved by:

Dr. Sheldon Jeter, Advisor
School of Mechanical Engineering
Georgia Institute of Technology

Dr. Yogendra Joshi
School of Mechanical Engineering
Georgia Institute of Technology

Dr. S. Mostafa Ghiaasiaan
School of Mechanical Engineering
Georgia Institute of Technology

Date Approved: January 8, 2008

To my wife Lee Ann

ACKNOWLEDGEMENTS

I would like to thank my advisor, Dr. Sheldon Jeter, for all his help and guidance. I would also like to acknowledge my reading committee, Dr. Yogendra Joshi and Dr. Mostafa Ghiaasiaan for reviewing my thesis.

In addition, I would like to thank Dr. Milton Goldman and Dr. Farhad Memarzadeh for their help with the background information. Indeed Dr. Goldman, who sadly passed away very recently, strongly encouraged and contributed to this research. He was a long-time advocate of research to mitigate airborne infections.

Thank you to Brian Lockwood for all the work he did with the initial operating room setup and camera positioning system. I also want to acknowledge Rich Wojcio and Craig Green for helping me with the experimental runs. I could not have done it without your help. I sincerely appreciate all the help. Finally, a very special thanks go to Rachel Valade for all of her help with classes and making my time in graduate school enjoyable.

TABLE OF CONTENTS

	Page
Acknowledgements	iv
List of Tables	vii
List of Figures	viii
List of Symbols and Abbreviations	xi
Summary	xiii
1. Introduction	1
1.1. History of Operating Room Ventilation	2
1.2. ASHRAE Guidelines For Hospital Operating Rooms	4
1.3. Buoyancy	5
2. Georgia Tech Operating Room Simulator	9
2.1. Operating Room Simulator	9
2.2. Air Flow Rate	17
2.3. Camera Positioning System	21
3. Particle Image Velocimetry	26
3.1. PIV Background	26
3.2. Camera and Laser Settings for a Run	28
3.3. PIV Verification	28
3.3.1. Verification Device	28
3.3.2. Verification Test Runs	30
3.3.3. Verification Results	31
4. Experimental Test Runs	35
4.1. Additional Test Runs	40
5. Computational Fluid Dynamics Analysis	43
5.1. Computational Fluid Dynamics Background	43
5.1.1. Continuity and Momentum Equations	43
5.1.2. Energy Continuity Equation	43
5.1.3. Turbulence Modeling	44

5.2. Computational Fluid Dynamics Analysis Methodology 45
5.3. Computational Fluid Dynamics Analysis Results 50
5.4. Comparison with Experimental Results 52

6. Conclusion 57

Appendix A – Experimental Test Run Results 59

Appendix B – Average Plots for the Four Cases 71

Appendix C – CFD Results 75

Appendix D – Complete PIV Procedure 79

Appendix E – Stepper Motor Controller 93

Appendix F – Heat Flux Calculations 94

References 95

LIST OF TABLES

Page

Table 2.1: Channel Settings in Data Logger 17

Table 2.2: Locations Used for Flow Rate Traverse Measurements 19

Table 3.1: Camera and Laser Settings 28

Table 5.1: Operating Conditions 46

Table 5.2: Root-Mean Squared Error Between Experimental Results and CFD Results 56

LIST OF FIGURES

Page

Figure 1.1: Example Parallel (Laminar) Air Flow Configuration 3

Figure 1.2: Illustration of Aiding Buoyant Flow 7

Figure 2.1: ORS in Comparison to Entire Hospital Operating Room 9

Figure 2.2: Simplified Schematic of the Georgia Tech Operating Room Simulator (ORS) 10

Figure 2.3: ORS Flow Schematic 11

Figure 2.4: Modified Laskin Nozzle Installed in ORS 12

Figure 2.5: Schematic of Fog Generating System 13

Figure 2.6: Arrangement of Fog Nozzles Inside ORS Diffuser 13

Figure 2.7: Illustration of Insulation Addition 14

Figure 2.8: Operating Room Simulator Before the Addition of Glass Fiber Insulating Panels 15

Figure 2.9: Operating Room Simulator After the Addition of Glass Fiber Insulating Panels 15

Figure 2.10: Thermocouple Locations in the ORS 16

Figure 2.11: Locations of Flow Measurements [17] 18

Figure 2.12: Plot of Measured Flow Rate Versus the Square Root of q_D 19

Figure 2.13: Flow Balance Through Each Diffuser at Calculated Flow Rate of 330 CFM 20

Figure 2.14: Flow Balance Through Each Diffuser at Calculated Flow Rate of 420 CFM 20

Figure 2.15: Camera Positioning System 21

Figure 2.16: Camera Positioning System 22

Figure 2.17: Stepper Motor Controller Wiring Diagram 23

Figure 2.18: Locations of Zones for 25-Point Run 24

Figure 3.1: Particle Movement Between Pulses Results In Vector Shown on the Right 26

Figure 3.2: Example Vector Field from PIV Results 27

Figure 3.3: Gear Motor with Rotating Verification Disc 29

Figure 3.4: Rotating Disc Positioned in the Plane of the PIV Laser 29

Figure 3.5: PIV Verification Run 1 30

Figure 3.6: PIV Verification Run 2 31

Figure 3.7: Plot of Velocity Vector Field for Verification Run 1 32

Figure 3.8: Plot of Velocity Vector Field of Verification Run 2 32

Figure 3.9: Radius versus Measured Velocity for PIV Verification Run 1 33

Figure 3.10: Radius versus Measured Velocity for PIV Verification Run 2 34

Figure 4.1: Representative Plot of 330 CFM, Patient Cold Case 36

Figure 4.2: Representative Plot of 330 CFM, Patient Warm Case 36

Figure 4.3: Representative Plot of 420 CFM, Patient Cold Case 37

Figure 4.4: Representative Plot of 420 CFM, Patient Warm Case 37

Figure 4.5: Contour Plot of Patient Region for 330 CFM, Patient Cold Case 38

Figure 4.6: Contour Plot of Patient Region for 330 CFM, Patient Warm Case 39

Figure 4.7: Contour Plot of Patient Region for 420 CFM, Patient Cold Case 39

Figure 4.8: Contour Plot of Patient Region for 420 CFM, Patient Warm Case 40

Figure 4.9: Experimental Results from 330 CFM, Patient 100°F 41

Figure 4.10: Experimental Results from 420 CFM, Patient 100°F 41

Figure 4.11: Contour Plot of Patient Region for 330 CFM, Patient 100°F 42

Figure 4.12: Contour Plot of Patient Region for 420 CFM, Patient 100°F 42

Figure 5.1: Definition of Boundary Conditions Used for Analysis 48

Figure 5.2: Gambit Mesh of ORS 49

Figure 5.3: CFD Results for 330 CFM, Patient Cold in Region of Experimental Results 50

Figure 5.4: CFD Results for 330 CFM, Patient Warm in Region of Experimental Results 51

Figure 5.5: CFD Results for 420 CFM, Patient Cold in Region of Experimental Results 51

Figure 5.6: CFD Results for 420 CFM, Patient Warm in Region of Experimental Results 52

Figure 5.7: Comparison of CFD Zone Averages with Experimental Zone Averages for 330 CFM, Patient Cold Case 53

Figure 5.8: Comparison of CFD Zone Averages with Experimental Zone Averages for 330 CFM, Patient Warm Case 54

Figure 5.9: Comparison of CFD Zone Averages with Experimental Zone Averages for 420 CFM, Patient Cold Case 54

Figure 5.10: Comparison of CFD Zone Averages with Experimental Zone Averages for 420 CFM, Patient Warm Case 55

LIST OF SYMBOLS AND ABBREVIATIONS

A_c	Cross Sectional Area
Ar	Archimedes Number
ASHRAE	American Society of Heating, Refrigerating, and Air-Conditioning Engineers
β	Thermal Expansion Coefficient
CCD	Charge-Coupled Device
CDC	Centers for Disease Control
CFD	Computational Fluid Dynamics
CFM	Cubic Feet Per Minute
C_p	Specific Heat at Constant Pressure
ε	Realizable Turbulent Transport Condition
FPM	Feet Per Minute
g	Gravitational Constant
Gr	Grashof Number
GUI	Graphical User Interface
HEPA	High Efficiency Particulate Air
HVAC	Heating, Ventilating, and Air-Conditioning
k	Turbulence Kinetic Energy
k_t	Thermal Conductivity
L	Characteristic Length
M_t	Turbulent Mach Number
ω	Angular Velocity
OR	Operating Room
ORS	Operating Room Simulator

PIV	Particle Image Velocimetry
Q	Volumetric Flow Rate
$\dot{q}$	Heat Transfer Rate per Unit Area
$\dot{Q}$	Total Heat Transfer Rate
q_D	Dynamic Pressure
R	Thermal Resistance, R-Value
Re	Reynold's Number
ρ_B	Boussinesq Density
SSI	Surgical Site Infection(s)
T_s	Surface Temperature
T_∞	Upstream Temperature
u	Velocity in the x-Direction
u_{in}	Diffuser Face Velocity
V	Magnitude of Velocity
$\vec{v}$	Velocity Vector
v	Velocity in the y-Direction
VAV	Variable Air Volume

SUMMARY

Surgical site infections are an area of concern for hospitals, doctors, and surgical patients. Several years ago, sophisticated computational fluid dynamics (CFD) research conducted by the National Institutes of Health concluded that a buoyant flow generated from the patient's body heat would be able to sufficiently prevent airflow, which could carry infectious particles, from impinging directly on the surgical site under recommended conditions. The suspected buoyant thermal was found to be a stagnation region of warm air or a slowly circulating three-dimensional vortex driven by a temperature gradient. The study presented in this thesis aimed to experimentally determine the airflow patterns around a patient in an operating room and to determine the effect, if any, of the buoyant flow. In addition, independent CFD analysis was conducted to compare with the experimental results and determine if standard CFD simulations can reliably predict the airflow around the surgical site.

The results from both the experimental data and the CFD analysis indicate that the buoyant flow probably does not play a dominant role in protecting the surgical site under normal operating room conditions. Further research should be done utilizing particle tracking to determine to flow of particles within the airflow of the hospital operating room.

1. INTRODUCTION

Surgical Site Infections (SSI) are a significant and potentially preventable source of illness and death for surgical patients. A study done by the Centers for Disease Control (CDC) reported that 2.6% of all operations were complicated due to SSI [1]. This means that of the 27 million surgical procedures done in the United States every year [2], almost 700,000 will lead to SSI for the patient. It has been estimated that each occurrence of SSI increases the procedure costs by $5,000 [3]. This means SSI are responsible for an approximately $3.5 billion drain on the health care industry, and this is only the amount the hospital experiences. The full cost, including time away from work, degraded lifestyle, suffering, and death, is surely much higher. Surgeons and other health professionals have focused on more effective medical approaches to preventing infections, such as proper hygienic practices and prophylactic antibiotics. These techniques have proven very effective, but SSI still occur in surgery patients. An unknown, but probably substantial, number of those infections are caused due to airborne bacteria present in the operating room (OR), which could be minimized with an optimal configuration of the OR ventilation system.

Microorganisms from within or on the patient's body cause many infections for surgical patients, but a significant number of the remaining cases are attributed to airborne exogenous (external to the body) organisms. The most common pathogen responsible for SSI is Staphylococcus aureus, which was isolated in 48% of patients with SSI in a study done by Kirkland [3]. Staphylococcus aureas is a Gram-positive spherical bacteria, meaning it retains a crystal violet dye during the Gram stain process [4].

Staphylococcus aureas is commonly found on normal human skin [5]. The transmission of Staphylococcus aureas is especially troubling due to the fact that in recent years, several strands of the bacteria have been found that are resistant to traditional antibiotics [5].

Released skin flakes, or squames, from exposed regions of the surgical staff and patient are the primary transportation mechanism for bacteria in the OR [6]. These squames have been found to be approximately 25 microns (μm) in diameter by 3 to 5 microns thick. It has been estimated that approximately 1.15 million to 90 million squames are released into the OR during a typical two hour surgery [6]. The traditional Heating, Ventilating, and Air-Conditioning (HVAC) solution to prevent the transmission of infections in this fashion has been to dilute and remove infectious particles from the OR by increasing the air flow rate into the room [7].

Various OR ventilation techniques have been developed and implemented through the years. The most prominent OR configuration is vertically downward flow, but horizontal parallel flow and trumpet-shaped down and outward diffusing flow are also represented. The recommended air speeds in these different configurations vary significantly from 30 feet per minute (FPM) to as much as 100 FPM. This wide disparity in recommended flow rates, as well as the abundance of ventilation configurations, has led to confusion over which HVAC system is the most effective at preventing infections.

1.1. History of Operating Room Ventilation

The first “clean rooms” were established by the United States Air Force during World War II for the assembly of gyroscopes and bomb-sights [8]. With the advent of atomic weaponry came the need for even cleaner clean rooms. This led to the

development of the laminar air flow "ultra-clean" room in 1960 [8]. Laminar air flow is referred to as such in the medical field, but a more accurate description is parallel air flow. The first parallel air flow clean room was a horizontal flow room built at Sandia Laboratories in Albuquerque, NM [8]. Parallel flow was produced by forcing air through high efficiency particulate air (HEPA) filters, which was able to filter out 99.97% of particulates 0.3 micrometers or more in diameter [8].

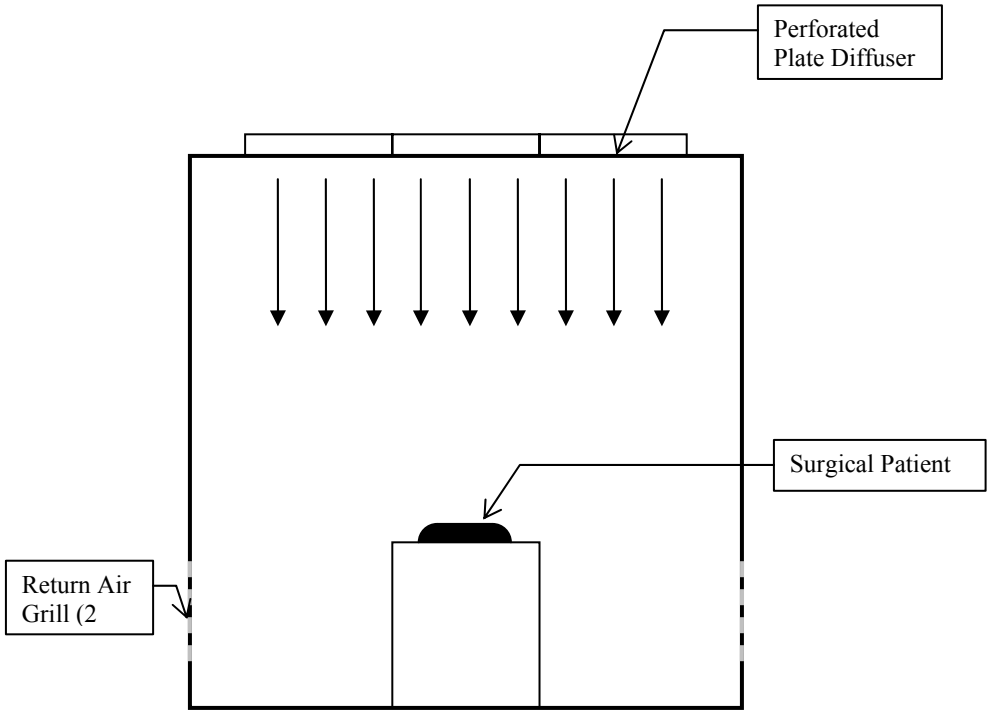

Figure 1.1: Example Parallel (Laminar) Air Flow Configuration

In December 1961, discussions began to use the newly developed clean room for medical applications. Bacterial studies were started in April 1962 in the parallel air flow clean room at Sandia Laboratory and were reported in 1965 [8]. These studies concluded that a parallel air flow operating room configuration would reduce the possibility of airborne contamination from pathogenic bacteria. On the basis of those studies, the first vertical parallel air flow system was installed in an OR in Bataan Memorial Hospital in Albuquerque, New Mexico and began operating on January 3, 1966 [8]. Since that time,

parallel air flow systems have become the dominant airflow configuration for hospital operating rooms; however, a number of different configurations are represented and confusion exists as to which configuration is optimal to prevent infections.

1.2. ASHRAE Guidelines For Hospital Operating Rooms

In 2003, the American Society of Heating, Refrigerating and Air-Conditioning Engineers (ASHRAE) published guidelines on OR air distribution in its HVAC Design Manual for Hospitals and Clinics. These guidelines were based on innovative computational fluid dynamics (CFD) modeling and simulations done by Dr. Farhad Memarzadeh and Dr. Andrew Manning [9]. This CFD research found that a buoyant flow, generated by the patient's body heat, could play a significant role in protecting the surgical site from pathogens present in the operating room [9]. The conclusion of the research was that vertically downward parallel flow with a face velocity of 30-35 FPM (0.15-0.18 m/s) at the ceiling-mounted diffuser exit and low returns or a combination of low and high returns is the best OR air distribution design [9]. The CFD simulations, however, were not confirmed by direct experimental work.

This paper focuses on experimentally determining the airflow patterns around a patient in an OR and the influence of buoyancy. Particle Image Velocimetry (PIV) technology was used extensively in this study in order to generate the flow data around a simulated patient. The experimental work was conducted in an operating room simulator. A considerable amount of work was put in to constructing the operating room and calibrating the flow rate entering the room. The experimental setup is described in Section 2, and information about the experimental runs is given in Section 4.

Independent CFD analysis was also performed as part of this investigation into the influence of buoyancy above a surgical site during normal operating room conditions. This independent CFD analysis was done using a standard commercial CFD program both to help guide and interpret the experimental results and to test the performance of a more readily available tool in predicting the experimental findings. The CFD analysis is detailed in Section 5.

Four different cases were considered as part of this study. Runs were done for two different flow rates: 330 cubic feet per minute (CFM) and 420 CFM. These two flow rates correlate to inlet velocities of 12.56 FPM (.064 m/s) and 15.99 FPM (.081 m/s), which is lower than the face velocity recommended by Dr. Memarzadeh. A simulated patient in the center of the experimental setup was either heated or left at ambient temperature in order to determine the effect, if any, of buoyancy above the surgical site. In Dr. Memarzadeh's analysis, the surgical site was assumed to be 100°F (37.8°C) [9], which is close to the typical body core temperature of 98.6°F (37°C) [10]. This temperature, however, was found to be inaccurate. Field tests performed by Dr. Jeter and Dr. Goldman found that the surgical site temperature was approximately 85°F (29.4°C) during surgery [11]. For the experimental runs, the simulated patient was heated to 85°F (29.4°). The buoyant flow should dominate with the patient heated under the described flow conditions.

1.3. Buoyancy

Two separate forms of convective transport exist: natural and forced. Both of these transportation modes exist in the air flow around a patient in an operating room, which results in a mixed convection flow regime. Buoyant flows, or natural convection,

are driven by a density gradient between the source fluid and its surroundings. Buoyant flows are generally divided into two groups: plumes or thermals. A plume is defined a continuous buoyant flow between the source and the level of interest [27]. A thermal is a sudden release of a buoyant region of fluid. The buoyancy, in the case of a thermal, remains confined to a limited volume, which rises and loses its connection with the source [27]. Detailed observations show that the flux from a heated boundary is intermittent rather than steady. Buoyant fluid tends to slowly accumulate at the surface and then break away, either as a thermal, or as an unsteady plume that wanders about the surface [27]. The flow seen by Dr. Memarzadeh in his CFD research would indicate the existence of a stable buoyant plume above the surgical site.

Much of the research done in the field of buoyancy has focused on aiding forced and natural convection effects. The opposing effects, like those seen in an operating room, have not been considered in comparable detail [26]. A derivation of the effect buoyancy has on a mixed flow was shown by Gebhart [26]. Consider an upward laminar flow of a uniform stream (U_∞, T_∞) over a flat vertical surface with a length of L. The surface temperature, Ts, is taken as a uniform temperature greater than T_∞. The buoyancy forces will aid the forced flow in this situation. The flow is illustrated in the following figure.

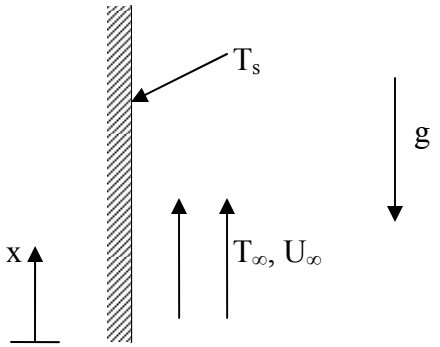

Figure 1.2: Illustration of Aiding Buoyant Flow

The coordinates are defined such that x is positive up. Gravity, g, is defined as being downward. The x-direction component of the Navier-Stokes equation, with uniform properties except for buoyancy, can be defined as [26]:

$$u\frac{\partial u}{\partial x}+v\frac{du}{dy}=-\frac{1}{\rho}\frac{\partial p}{\partial x}+\nu\nabla^2 u-g\beta(T_s-T_\infty) \tag{1.1}$$

This equation can be normalized by introducing several dimensionless parameters [26].

$$X=\frac{x}{L} \qquad Y=\frac{y}{L} \qquad \phi=\frac{T-T_\infty}{T_s-T_\infty} \qquad P=\frac{\rho-\rho_\infty}{\rho U_\infty^2/2} \tag{1.2}$$

$$u'=\frac{u}{U_\infty} \qquad v'=\frac{v}{U_\infty} \qquad \nabla'^2=L^2\nabla^2$$

Substituting in the dimensionless parameters and simplifying results in the following equation [26].

$$u'\frac{\partial u}{\partial X}+v'\frac{\partial u}{\partial Y}=-\frac{1}{2}\frac{\partial P}{\partial X}+\frac{\upsilon}{U_\infty L}\nabla'^2 u'+\frac{g\beta L^3(T_s-T_\infty)}{\upsilon^2}\frac{\upsilon^2}{U_\infty^2 L^2}\phi \tag{1.3}$$

The last term of the equation can be recognized as the Grashof number divided by the Reynold's number squared. This indicates that the buoyancy effect will be comparable to the forced flow effects if the coefficient is of the order 1, as well as the convective terms. The ratio of the Grashof number to the Reynold's number squared is

also defined as the Archimedes number, which simplifies as shown in the equation below.

$$Ar = \frac{Gr}{Re^2} = \frac{\dfrac{g\beta(T_s - T_\infty)L^3}{\nu^2}}{\left(\dfrac{uL}{\nu}\right)^2} = \frac{g\beta(T_s - T_\infty)L}{u^2} \qquad \textbf{(1.4)}$$

The magnitude of the Archimedes number indicates the relative effect of buoyancy on forced convection. High values of this quantity, on the order of 10 or above, indicate significant buoyant effects in the flow [26]. The calculation of this number, however, can be fairly ambiguous. The length scale that should be used is undefined. In addition, the upstream velocity is not completely defined. For the purposes of this research, the face velocity at the diffuser exit was used; however, due to recirculation regions within the experimental setup, which will constrict the flow above the patient, the velocity upstream of the patient is surely higher than the face velocity. The Archimedes numbers were calculated for each of the four experimental cases, but are presented in this thesis for reference only.

2. GEORGIA TECH OPERATING ROOM SIMULATOR

The research presented in this thesis made extensive use of the Georgia Tech Operating Room Simulator (ORS). The ORS simulates the area around a patient during surgery, called the surgical zone, not an entire operating room (OR), as shown internally in Figure 2.1. The ORS was designed and built to investigate the airflow patterns above a surgical patient in an operating room with a vertically downward parallel air distribution system, which can be found in a large number of hospital operating rooms in the United States. Particle Image Velocimetry (PIV) measurements were used to determine velocity fields of particles above the surgical site.

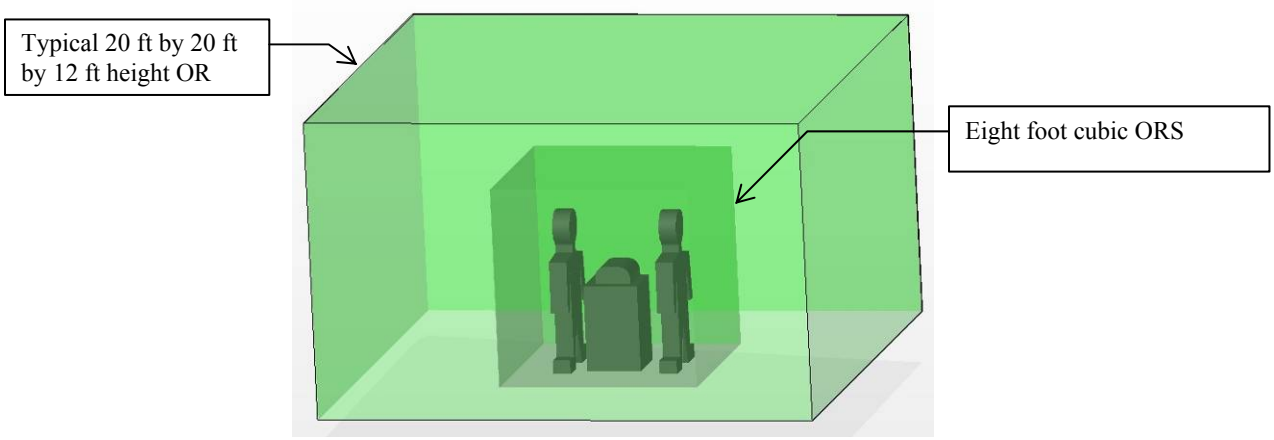

Figure 2.1: ORS in Comparison to Entire Hospital Operating Room

2.1. Operating Room Simulator

The ORS consists of an approximately 8 foot cubic room that is supplied with air via a 3 x 3 array of 24 inch diffusers installed in the center of the room ceiling. The inlet diffusers are perforated plate diffusers which are commonly used in ORS construction. Air is exhausted from the room through two 21 inch (height) x 96 inch (width) return air grilles, which are installed 8.5 inches from the ground on either side of the ORS.

The rate of airflow into the room is controlled by a Titus PESV-12 pneumatic single-duct Variable Air Volume (VAV) terminal unit installed in the air supply duct, which can be adjusted up to 1200 cubic feet per minute (CFM) airflow. Each diffuser is supplied with a dedicated line that branches off of a main plenum. Each diffuser supply line contains a damper and averaging Pitot tube flow measuring station to monitor and control the air flow to each perforated diffuser. A simplified 2-dimensional schematic of the ORS is shown in Figure 2.2.

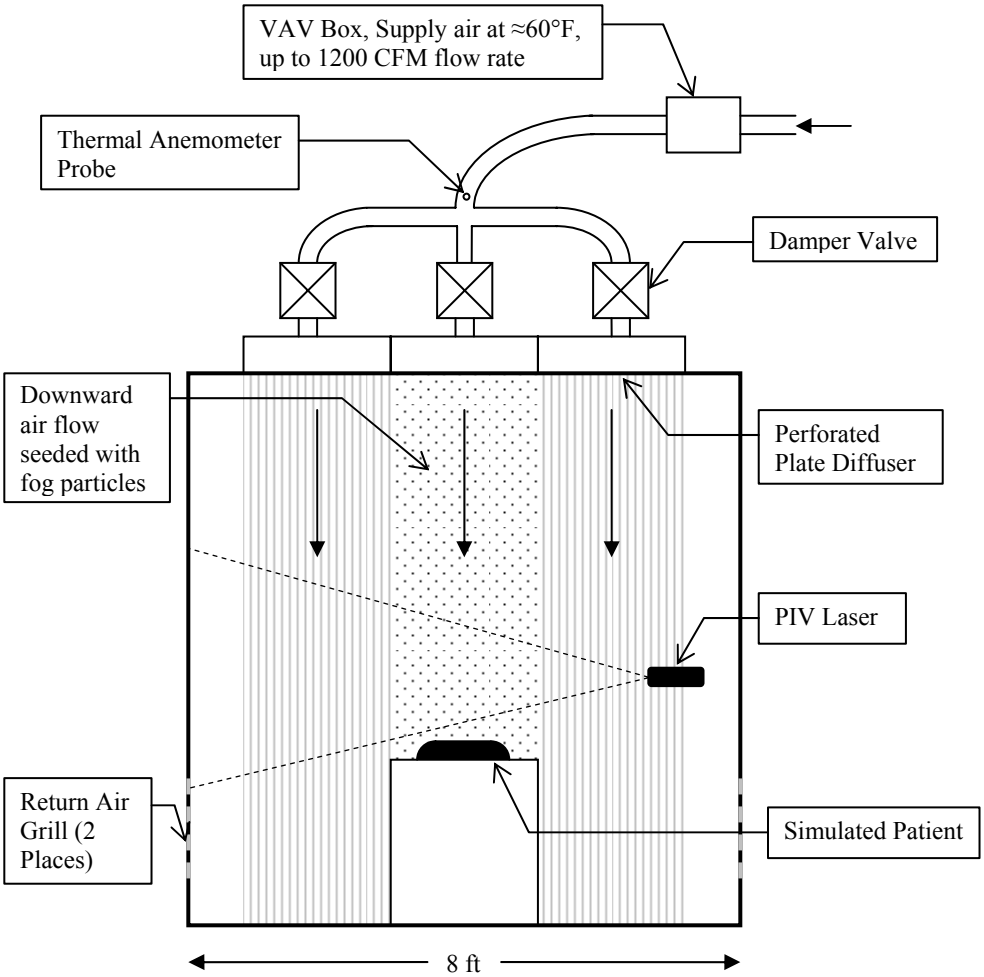

Figure 2.2: Simplified Schematic of the Georgia Tech Operating Room Simulator (ORS)

A flow schematic that shows which damper valve supplies each diffuser in the ORS is illustrated in the following figure. In addition, the fog injection points, which are described in the next section, are shown.

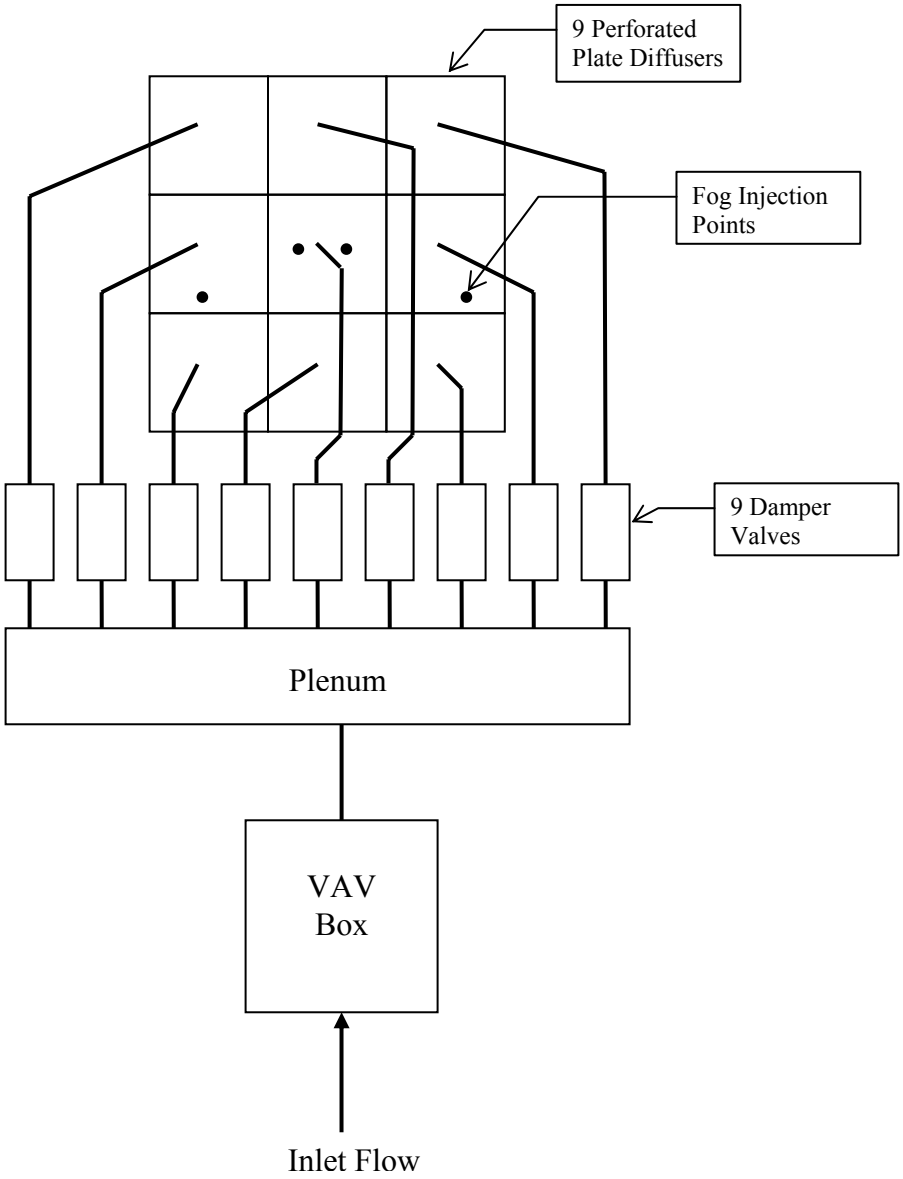

Figure 2.3: ORS Flow Schematic

In the center of the ORS is a water-filled aluminum vessel, which simulates a patient's chest cavity. The simulated patient is located 56 inches (1.4 m) downstream of the ceiling inlet diffusers. The temperature of the simulated patient can be adjusted by using a water heater pump (Brookfield EX-200), which is installed outside the room and

connected to the patient via plastic tubing. For a run in which the surface temperature of the patient was to be approximately 85°F (29.4°C), the water inside the patient is warmed to approximately 100°F (37.7°C).

In order to use a particle image velocimetry technique to evaluate the velocity fields of the flow above the patient's surgical site, the air must be seeded with neutrally-buoyant particles. Seeding the flow without influencing flow patterns is a significant challenge. The flow into the ORS is seeded by feeding a low-pressure flow through a copper tube, which is submerged in a fog-generating fluid. The submerged tube end is crimped, which forces the air to pass through 4 1/32-inch (0.79 mm) holes that are drilled into the tube. This method is very similar to fog generation with a Laskin Nozzle [12], which is commonly used for PIV measurements. A photo showing the modified Laskin Nozzle installed on the ORS is shown in the figure below.

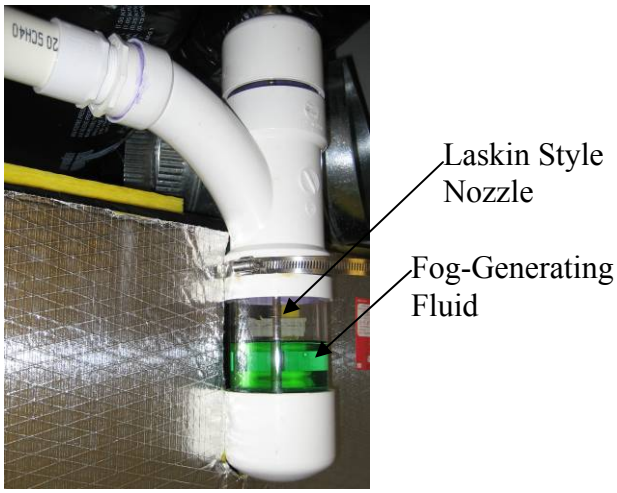

Figure 2.4: Modified Laskin Nozzle Installed in ORS

For the Georgia Tech ORS, Rosco Fog Fluid is used as the fog-generating fluid. As the air bubbles up through the fog-generating fluid, small particles of the fog are separated from the fluid reservoir turning the flow into an aerosol. The aerosol fluid is then injected into three diffusers in the room – in two locations in the center diffuser, and

one location each of other two diffusers, as shown in Figure 2.3. An overall schematic of the fog-generating system is shown below in Figure 2.5.

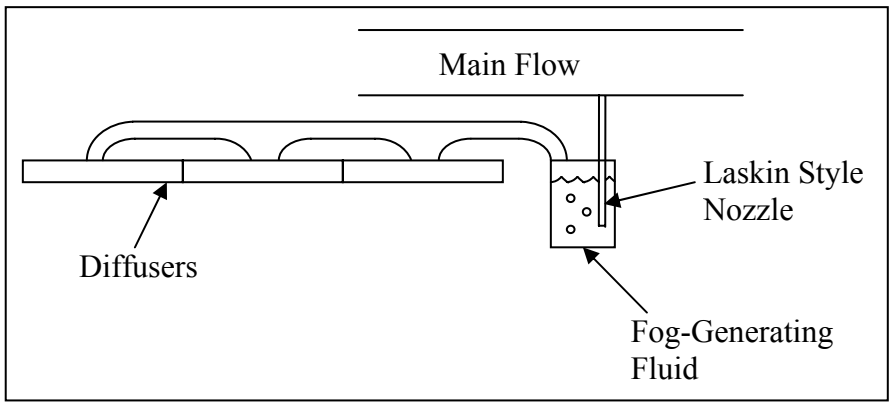

Figure 2.5: Schematic of Fog Generating System

The aerosol is injected into the diffusers by employing nozzles installed in the ceiling of the ORS. The arrangement of the nozzles inside the diffuser is illustrated in Figure 2.6.

Figure 2.6: Arrangement of Fog Nozzles Inside ORS Diffuser

In order to isolate the ORS from its surrounding environment, a significant amount of insulation was recently added. The ORS was initially constructed with ¼ inch (6.4 mm) foam board insulation, which was sufficient to isolate the room with respect to convective mass transfer from the surroundings, but it did very little to protect the ORS

from thermal conduction. A substantial amount of insulation was added in the form of glass fiber insulating panels, specifically Owens Corning QuietR Duct Board, which has an R-value of 0.76 m^2-K/W [13]. The duct board was added to the outside of the ORS frame, which left a 1.5-inch (38.1 mm) gap of air between the exterior of the foam board and the inside surface of the duct board.

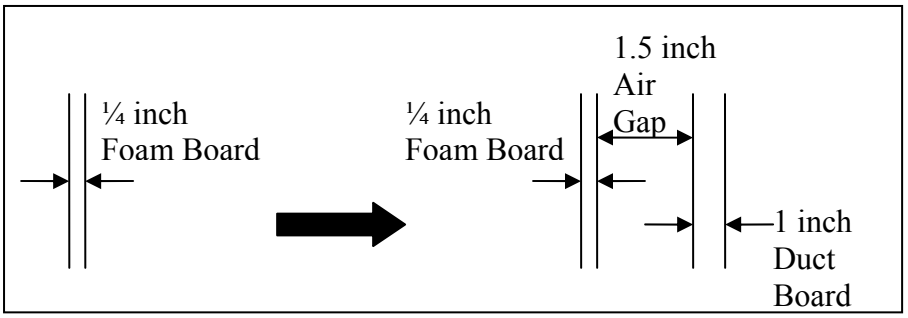

Figure 2.7: Illustration of Insulation Addition

The addition of the duct board with an air gap significantly raised the R-value of the room insulation. The R-value of insulation is calculated by employing the equation shown below, R is the R-value, k_t is the conductivity of the material, and x is the width of the material. The R-value of different insulations in series is found by summing up the individual R-values.

$$R = \frac{x}{k_t} \tag{2.1}$$

Using the R-value of a 1.5-inch gap of air from the ASHRAE handbook as 0.44 m^2-K/W [14], the R-value of duct board as 0.76 m^2-K/W, as previously mentioned, and the R-value of foam board as 0.11 m^2-K/W [15], it was found that the R-value of the insulation for the room increased from 0.11 m^2-K/W to 1.31 m^2-K/W. This increase was important to thermally isolate the room from the surrounding environment. Pictures of the ORS before and after the addition of the insulation are shown in the figures below.

Figure 2.8: Operating Room Simulator Before the Addition of Glass Fiber Insulating Panels

Figure 2.9: Operating Room Simulator After the Addition of Glass Fiber Insulating Panels

The temperature at various locations throughout the room is monitored continuously during an experimental run. Nine K-Type thermocouples are installed inside the ORS. They are located as follows: 2 in the inlet, 2 in the open air, 1 installed on the patient, 2 on the left side exhaust, and 2 on the right side exhaust. These thermocouples are read and the data from them is collected by using an Agilent 34907A Data Acquisition/Switch Unit and Agilent Benchlink Data Logger software to monitor

and log the temperature data. This data was used in the computational fluid dynamics (CFD) simulations. The thermocouples were calibrated in order to ensure high quality readings during experimental runs. The thermocouple locations are shown below in Figure 2.9.

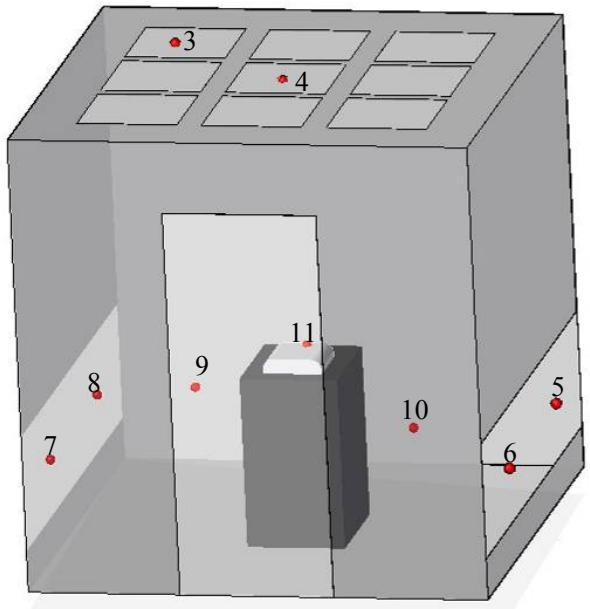

Figure 2.10: Thermocouple Locations in the ORS

Numbers shown are the assigned channel of the thermocouple, as shown in Table 2.1

In addition to the thermocouples installed in the room, the flow into the room is also continuously monitored during a run. The magnitude of the velocity is not monitored as much as the continuity of the flow to ensure that there are no spikes in the air flow. The flow is monitored by measuring the voltage potential induced in a modified analog Alnor Thermo-Anemometer. Each of the thermocouples and the thermo-anemometer are assigned a channel in the Agilent Data Acquisition/Switch Unit. The channels assigned for each component are shown in the table below.

Table 2.1: Channel Settings in Data Logger

Channel	Device	Measurement Location	Units
1	Alnor Thermo-Anemometer	Flow rate in duct upstream of plenum	VDC
2	K-Type Thermocouple	Ambient temperature outside ORS	°C
3	K-Type Thermocouple	Back-left diffuser inlet temperature	°C
4	K-Type Thermocouple	Center diffuser inlet temperature	°C
5	K-Type Thermocouple	Back-right exhaust temperature	°C
6	K-Type Thermocouple	Front-right exhaust temperature	°C
7	K-Type Thermocouple	Front-left exhaust temperature	°C
8	K-Type Thermocouple	Back-left exhaust temperature	°C
9	K-Type Thermocouple	Open air on left-side of ORS	°C
10	K-Type Thermocouple	Open air on right-side of ORS	°C
11	K-Type Thermocouple	Simulated Patient surface temperature	°C

2.2. Air Flow Rate

The most critical part of the experimental setup is the ability to carefully control the flow rate of air entering the ORS. The flow into the room is determined using an averaging pitot-tube (Dwyer Mark II) installed in the inlet duct, just upstream of the VAV box, and a Dwyer 1" manometer. It is possible to derive a relationship between the static pressure and the flow rate analytically using Bernoulli's Equation, as shown in Equation 2.2.

$$P + \frac{1}{2}\rho V^2 + \rho g h = \textbf{constant} \qquad \textbf{(2.2)}$$

Assuming that there is a negligible change in elevation, Equation 2.2 reduces to Equation 2.3, which relates the pressure measured by the pitot tube to the velocity of the flow in the duct.

$$V = \sqrt{\frac{2 \cdot \Delta P}{\rho}} \qquad \textbf{(2.3)}$$

The term ΔP can also be written as q_D, or the dynamic pressure. Equation 2.3 can be further developed to find a relationship between the volumetric flow rate and the dynamic pressure, as shown in Equation 2.4.

$$Q = A_c \cdot V = A_c \cdot \sqrt{\frac{2 \cdot q_D}{\rho}} \quad \textbf{(2.4)}$$

Using the parameters for the ORS, the following equation is obtained.

$$Q = 2205 \cdot \sqrt{q_D} \ \textbf{(CFM)} \quad \textbf{(2.5)}$$

where q_D is measured in inches of water column.

An experimental relationship between the gage pressure measured by the pitot tube and the overall flow rate was developed in order to confirm the analytical relationship. The experimental relationship was developed by doing traverses using a digital thermal anemometer [16]. In a traverse, measurements are taken with a flowmeter or a pitot tube at different distances from the center of the tube, as shown in Figure 2.10.

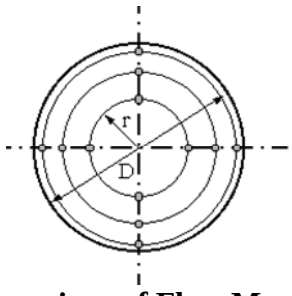

Figure 2.11: Locations of Flow Measurements [17]

The average of the velocities gathered is used to calculate the overall flow rate through the duct, as shown in Equation 2.5. The assumption used for applying traverses to determine the flow rate through a duct is that the flow is fully turbulent.

$$Q = A_{duct} \cdot \frac{1}{n} \cdot \sum_{i=1}^{n} v_i \quad \textbf{(2.6)}$$

Due to the importance of developing a reliable relationship between the static pressure and the flow rate, measurements were taken at four distances from the duct center in both the horizontal and vertical directions. The ratios used to determine the locations and the locations themselves are shown below in Table 2.2.

Table 2.2: Locations Used for Flow Rate Traverse Measurements

Distance from Center (r/D)	Radius (in)
0.177	2.124
0.306	3.672
0.395	4.74
0.468	5.616

Measurements were taken with the pitot tube at multiple q_D readings. The square root of the pressure was plotted against the calculated flow rate through the duct. Linear regression was done on the data in order to determine the best fit curve, as shown in Figure 2.11.

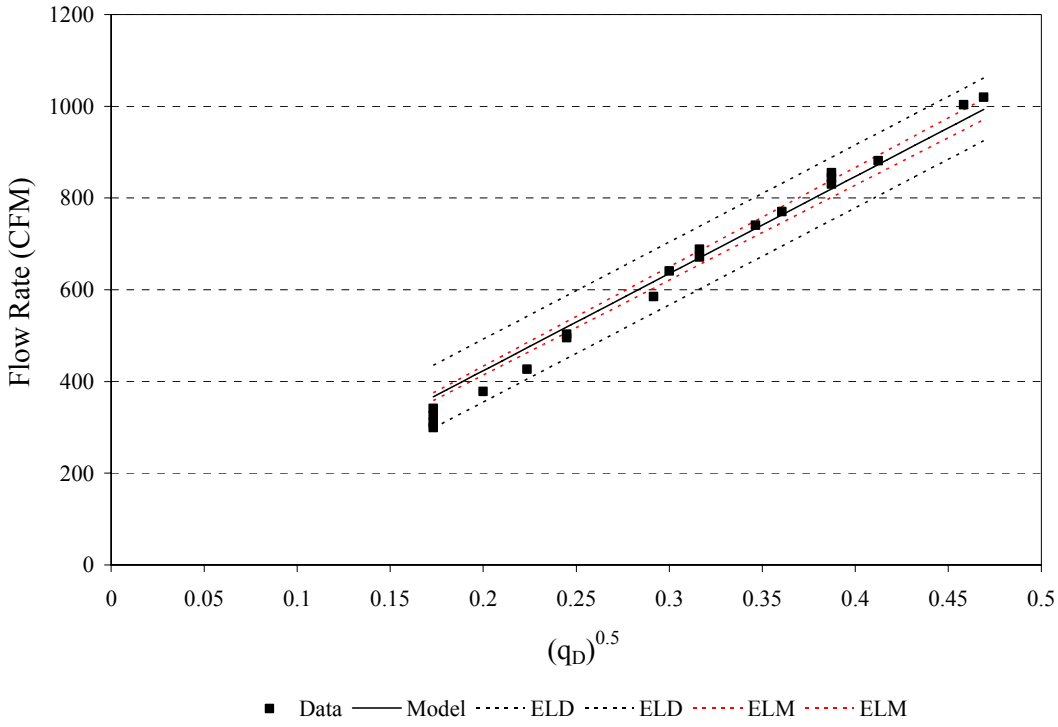

Figure 2.12: Plot of Measured Flow Rate Versus the Square Root of q_D

Equation 2.7 was derived by linear regression of the data.

$$Q = 2117 \cdot \sqrt{q_D} \pm 15 \text{ (CFM)} \qquad (2.7)$$

This equation agrees fairly well with Equation 2.5. The uncertainty obtained from linear regression is ±15 CFM, which is less than 5% of the flow at 330 CFM. This equation was used to calculate the flow for experimental runs.

In order to confirm the relationship developed by the traverse, direct measurements of the flow rate from each duct were conducted with an Alnor "Balometer" air balancing hood. This test also shows how well the diffusers are balanced, since an even flow from each diffuser is desired. Figures 2.8 and 2.9 show the results of the Alnor measurements. The numbers shown are in cubic feet per minute (CFM) of air passing through each diffuser in the ORS diffuser array.

30	35	35
30	35	40
35	35	35

Figure 2.13: Flow Balance Through Each Diffuser at Calculated Flow Rate of 330 CFM

The summation of the flow is 310 CFM
The average flow through each diffuser is 34.4 CFM
The greatest delta is 5.5 CFM or 16% from the average

45	55	45
40	50	50
50	45	45

Figure 2.14: Flow Balance Through Each Diffuser at Calculated Flow Rate of 420 CFM

The summation of the flow is 425 CFM
The average flow through each diffuser is 47.2 CFM
The greatest delta is 7.2 CFM or 15% from the average

2.3. Camera Positioning System

A unique feature of the Georgia Tech ORS is the camera positioning system. The camera positioning system makes it possible to take PIV measurements at multiple locations without entering the room. This is paramount because entering the room would cause disturbances in the airflow within the room. The camera positioning system allows for movement in both the X and Y direction. A schematic of the positioner system is shown in Figure 2.14.

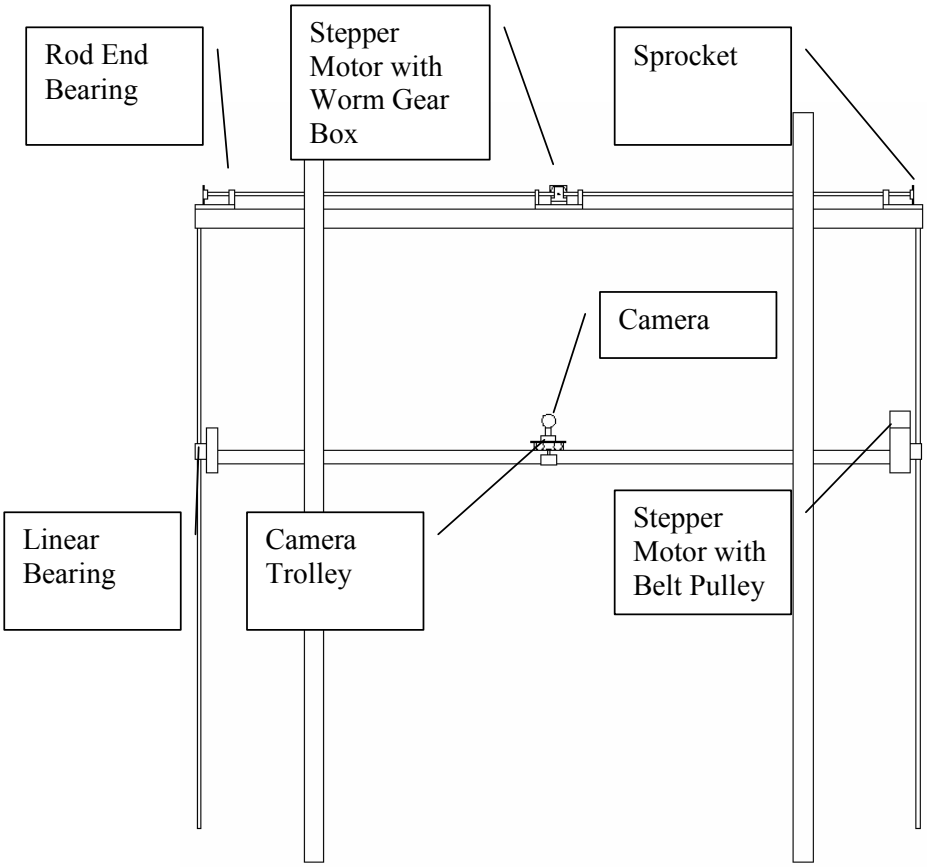

Figure 2.15: Camera Positioning System

The horizontal positioner is a belt-driven trolley on a rail. The belt is attached to a computer-controlled Superior Electric stepper motor, model number M061-LF-544, which is capable of microstepping. The stepper motor drives the toothed belt to position the trolley. The vertical positioner is a chain hoist. Another computer-controlled

Superior Electric stepper motor drives the input of a worm-gear right angle gear box, which has a reduction ratio of 60:1, at the top of the positioner. The output of this gear box drives the horizontal shaft at the top of the positioner. Sprockets are attached to both ends of the shaft. The horizontal positioner is attached to an ANSI number 25 chain which runs over the sprocket and to a counterweight. The rotation of the sprocket will raise or lower the horizontal trolley rail. Vertical guides, which are linear ball bearings engaging vertical guide bars, maintain horizontal alignment. The supporting structure is constructed out of Unistrut. The vertical supports are bolted directly into the ceiling of the ORS. The horizontal support is bolted between the two vertical supports. A picture showing the camera positioning system is shown in Figure 2.15.

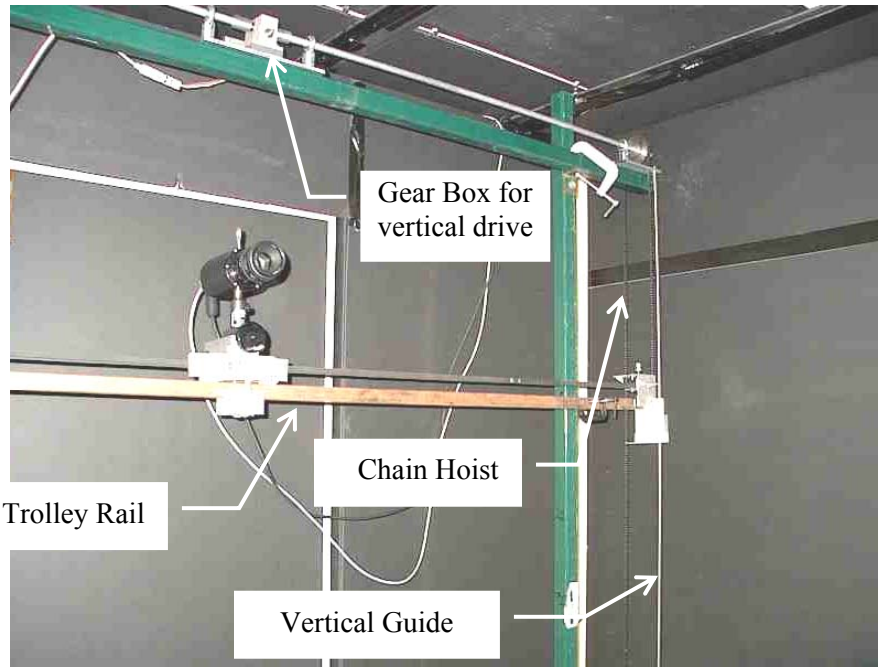

Figure 2.16: Camera Positioning System

The stepper motors are driven with Cyberpak, model CY-21, stepper motor controllers. These controllers are each supplied with 30VDC to ensure the highest possible performance of the motors. The controllers are triggered by the parallel port of the controlling computer. The Cyberpak controllers required three inputs from the

computer: Enable, Direction, and Step. Enable is hardware inverted such that a low signal on the enable pin enables the motor. The motor is made to step once every time the step pin is made high. The wiring of the pins to the parallel port can be found in the figure below.

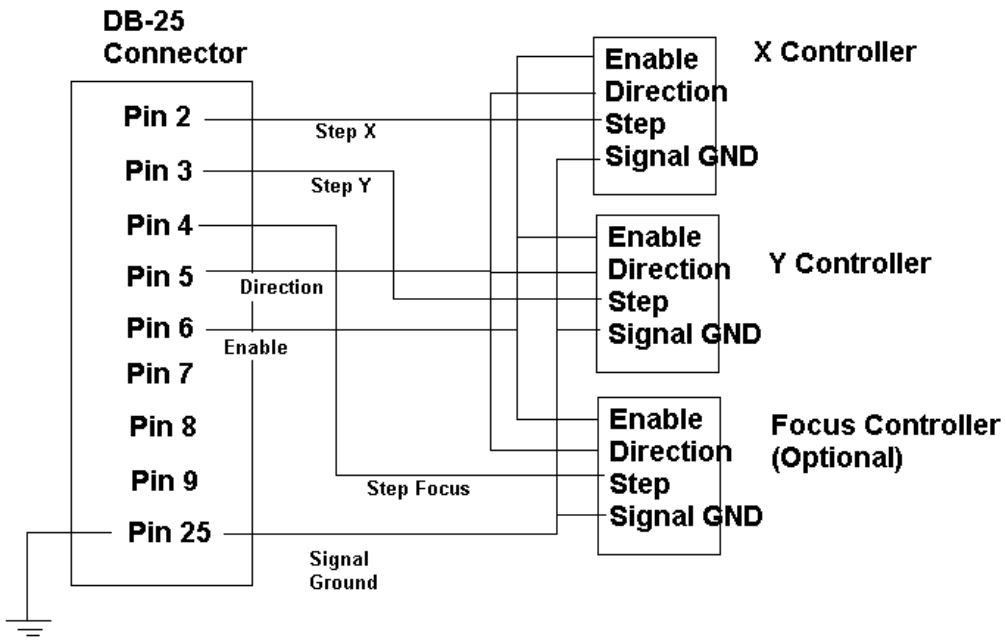

Figure 2.17: Stepper Motor Controller Wiring Diagram

The DB-25 connector wired to the controllers is connected to the parallel port on the computer (LPT1 or Address 0x378). The parallel port is manipulated using a program running within Matlab. A graphical user interface (GUI) was also made for this program. Because a programming wizard (Guide) was used to create the GUI, the details of it will be omitted. To drive the stepper motor, the proper value is written to the parallel port periodically. The code used to drive the X and Y controllers can be found in the Appendix E. This program takes in a non-zero displacement. The first step in the program is to gain access and configure the computer's parallel port. Next, the direction is found by determining the sign of the input displacement. Finally, a loop is used to repeatedly set the value of the port to the proper value (for the horizontal controller this is

8*direction+1) and zero. For the Y controller, a delay loop is needed to prevent the motor from missing steps. This is done by putting a dummy loop into the main loop. This dummy loop simply makes the computer count to 300000 before it repeats the instructions in the main loop.

Within the Matlab stepper program, 25 preset positions plus a reference home position are defined. PIV measurements are taken at the 25 preset positions above the simulated surgical patients. The positions are numbered from the bottom-left to the upper-right and are illustrated in the figure below.

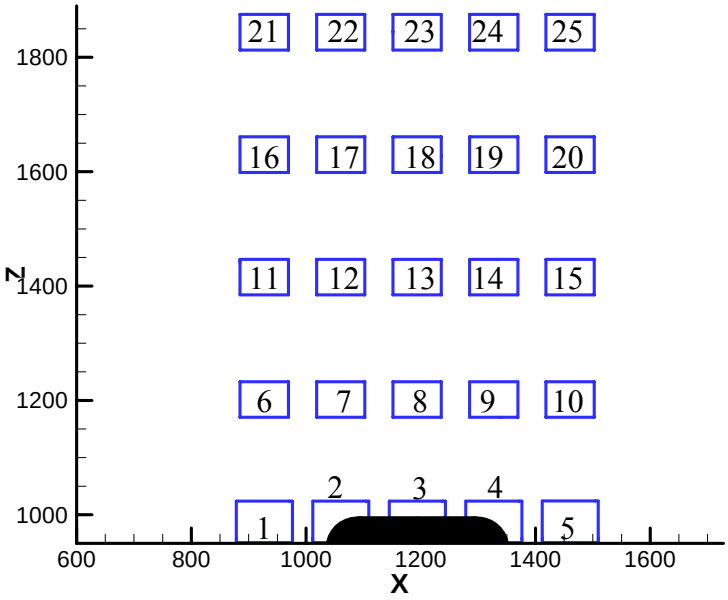

Figure 2.18: Locations of Zones for 25-Point Run

Zones are numbered from bottom-left to upper right
Axes are in mm

The coordinate system used to define the dimensions used is located at the lower left corner of the ORS. The overall area of measurement is from approximately 960 mm to 1875 mm in the z-direction by 886 mm to 1500 mm in the x-direction. Each zone is a section approximately 80 mm wide by 60 mm tall (3.1 inches wide by 2.4 inches tall) in

the plane of the PIV laser. The laser plane is located approximately 1100 mm in the y-direction, which means it is 1100 mm from the front wall of the ORS.

3. PARTICLE IMAGE VELOCIMETRY

3.1. PIV Background

Particle Image Velocimetry (PIV) is a very sophisticated but straight-forward method of determining the velocity of particles in a flow field. The particles of a seeded flow are illuminated by two quick, successive pulses from a laser light sheet. The pulsed laser is typically a dual cavity solid state laser such as a neodymium-doped yttrium aluminum garnet (Nd:YAG) ruby laser. A high-resolution (1360 x 1036 pixels) Charge-Coupled Device (CCD) camera is used to capture photographs of the light reflected from the laser off of the seeded particles. The camera and the double-pulsed Nd:YAG laser are connected to a host computer via a controller, which controls the timing of the laser illumination and the image acquisition. Velocity vectors are determined from each frame pair by employing cross-correlation statistical analysis to determine the movement of the particles between pulses [18]. Figure 3.1 shows how the movement of a particle is used to determine a velocity vector.

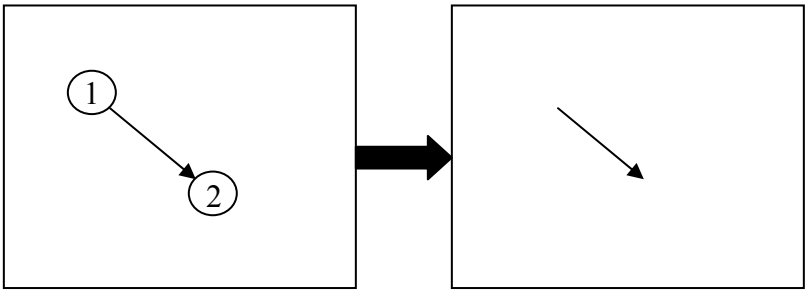

Figure 3.1: Particle Movement Between Pulses Results In Vector Shown on the Right

The velocity of the particles is calculated by dividing the distance traveled by the particles by the time separation of the pulses, as shown in the following equation.

$$V = \frac{d}{t_{pulse}} \tag{3.1}$$

The PIV method is derived from Laser Speckle Velocimetry, which is a method used to analyze solid surface movements [19]. Using PIV, it is possible to track the motion of many different particles and populate entire flow fields.

The software program proVISION-XS is used to capture multiple picture pairs and average vectors are determined for the flow of particles through the field of the capture region. An Integrated Design Tools (IDT) controller is used to relay the commands from the host computer to the PIV laser. Once the data is captured and analyzed with proVISION, Tecplot is used to graphically interpret the raw data in order to view the vector flow fields. For the data presented in this thesis, a sequence of 30 images (15 image pairs) was taken and the average velocity field was computed at each location. A 20 by 20 grid of 400 two-dimensional vectors was determined and plotted in Tecplot. An example flow field is shown in Figure 2.3 below.

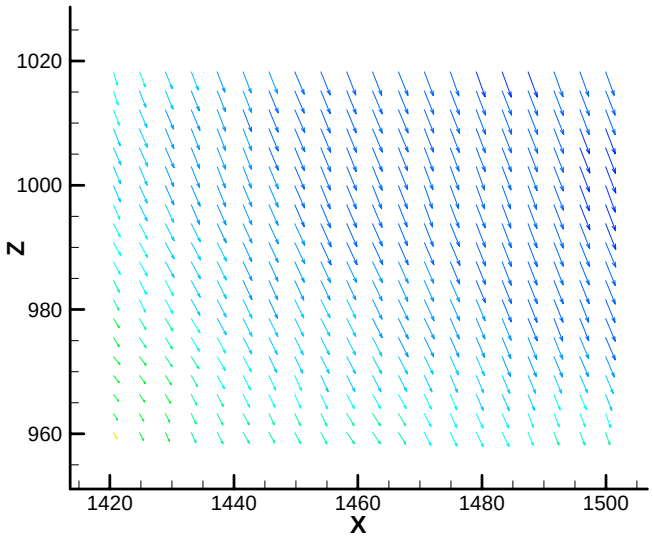

Figure 3.2: Example Vector Field from PIV Results

3.2. Camera and Laser Settings for a Run

The settings for the camera and laser are integral to getting good results from a PIV system. The pause between pulses was set such that particles would move approximately 3-5 pixels between picture pairs. Other values, such as the laser frequency and camera frequency, were adjusted to achieve high quality pictures of the particles in the flow. A table showing the camera and laser settings is shown below.

Table 3.1: Camera and Laser Settings

Exposure [μs]	234
Pulse Separation [μs]	1000
Laser Frequency [Hz]	15
Camera Div	30
Laser Frequency [Hz]	15
Camera Freqency [Hz]	.5

3.3. PIV Verification

In order to verify that the measurements taken by the PIV system were correct, a calibration of the PIV laser measurement system was performed. The idea was for the PIV system to take measurements of an object moving at a known speed. Data would be collected and processed as flow data would be for an experimental run. From there, it would be possible to compare the velocities from the experimental data to the known velocities.

3.3.1. Verification Device

An effective way to simulate objects moving would be to slowly rotate a disc that is lightly dusted with corn starch, similarly to how the air flowing through the room is seeded with fog. A 12 inch diameter disc was made out of one half inch thick particle board. This disc was rotated by an 18 RPM gear motor, which was mounted on an adjustable height camera stand. A picture of the rotating device is shown in Figure 3.3.

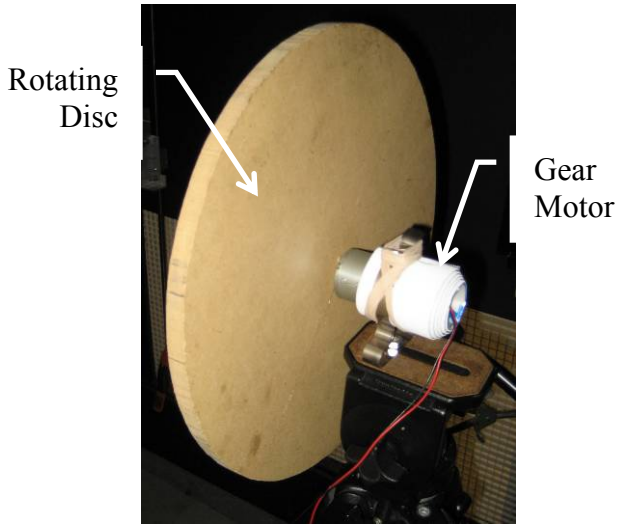

Figure 3.3: Gear Motor with Rotating Verification Disc

The rotating disc was positioned in the ORS in the same plane as the PIV laser. This would give a good comparison between the verification results and the experimental results obtained during test runs. A picture showing the configuration of the verification device in the ORS is shown in the figure below.

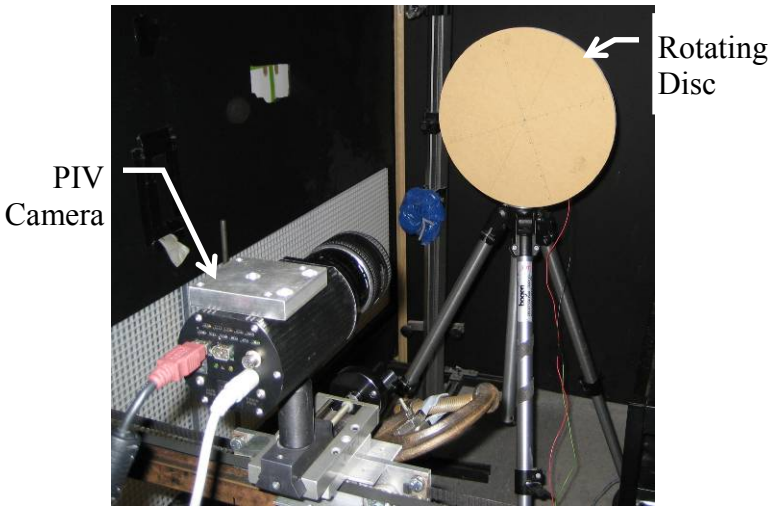

Figure 3.4: Rotating Disc Positioned in the Plane of the PIV Laser

It is a straight forward calculation to find the velocity at any point on a rotating disc by multiplying the rotational speed by the radius from the center of rotation, as shown in Equation 3.2.

$$V = r \cdot \omega \tag{3.2}$$

3.3.2. Verification Test Runs

ProVISION software was used to perform the laser-velocity measurements. ProVISION was set to take measurements at the same settings that are used for a fluid flow measurement. The pictures were then analyzed, again by proVISION, and the data was compiled in the same manner as a fluid flow measurement would be compiled.

Two verification test runs were performed on the rotating disc, with each test taking measurements at a different location on the disc. The velocities determined for each run was compared to expected velocities. The pictures of the areas of the disc considered for each verification run are shown in the following pictures.

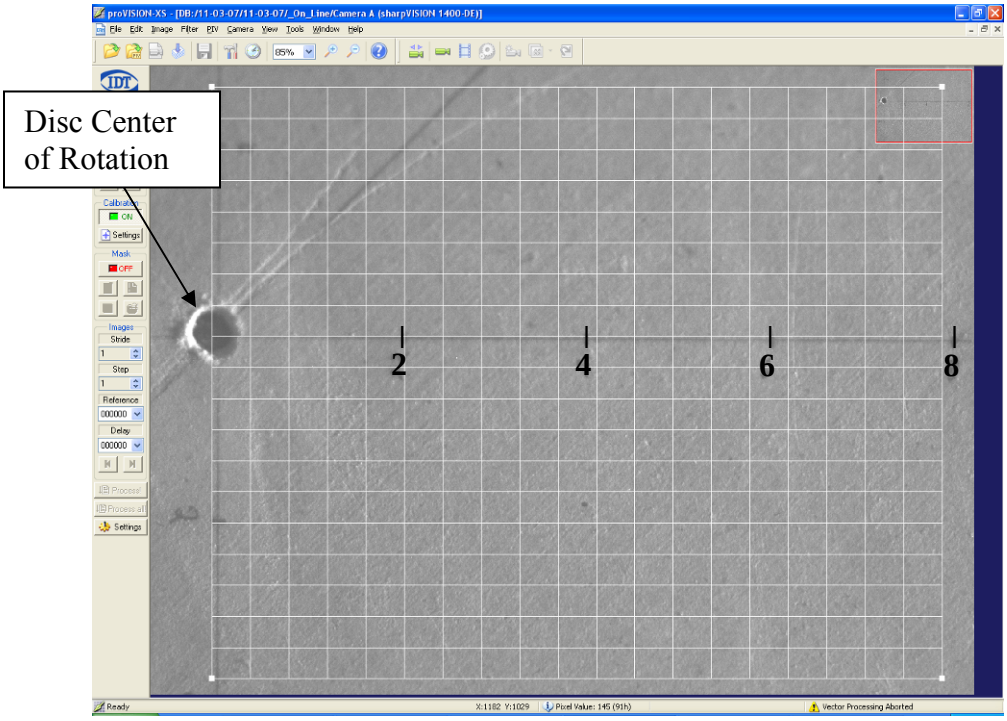

Figure 3.5: PIV Verification Run 1

Area of the disc between 0 and about 8 cm from the center of rotation
Numbers shown are the distance from the center of rotation in centimeters

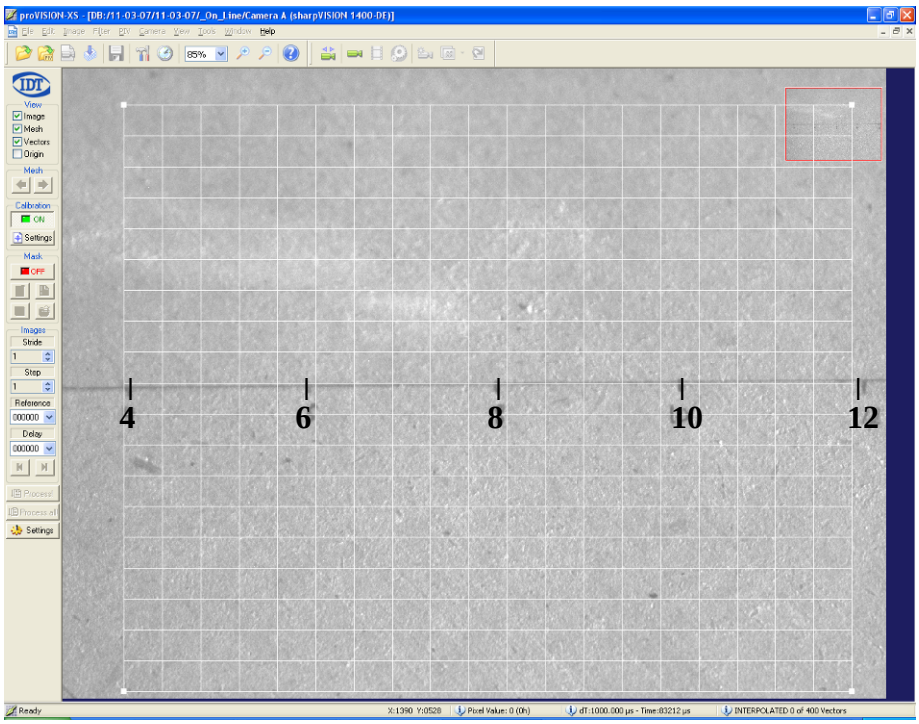

Figure 3.6: PIV Verification Run 2

Area of the disc from 4 to about 12 cm from the center of rotation
Numbers shown are the distance from the center of rotation in centimeters

3.3.3. Verification Results

The data was collected and analyzed in the same fashion as data would be collected and analyzed for a typical fluid flow run. Plots from Tecplot for each of the two runs are shown in the following figures.

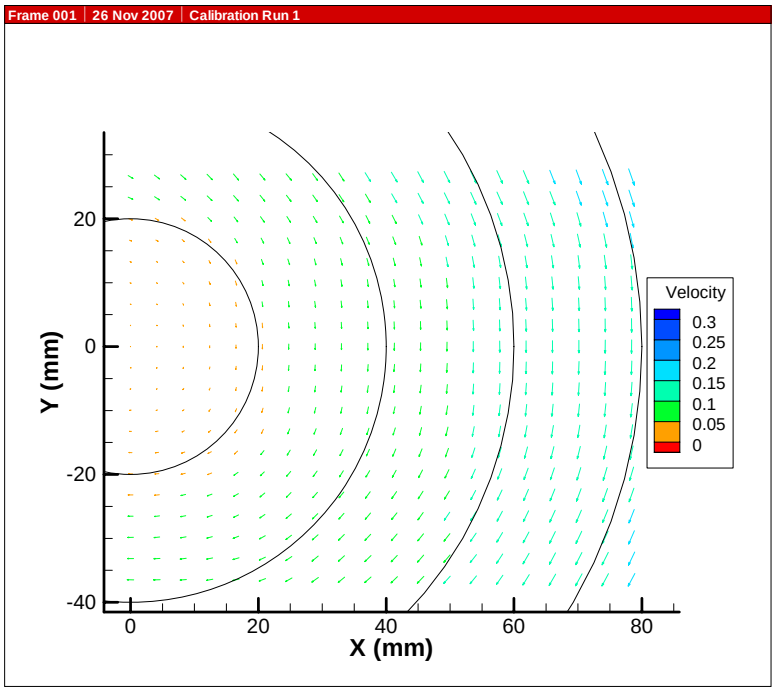

Figure 3.7: Plot of Velocity Vector Field for Verification Run 1

Vectors shown are magnitude of velocity in m/s
Center of rotation is located at (0,0)
Arcs shown are lines of constant radius

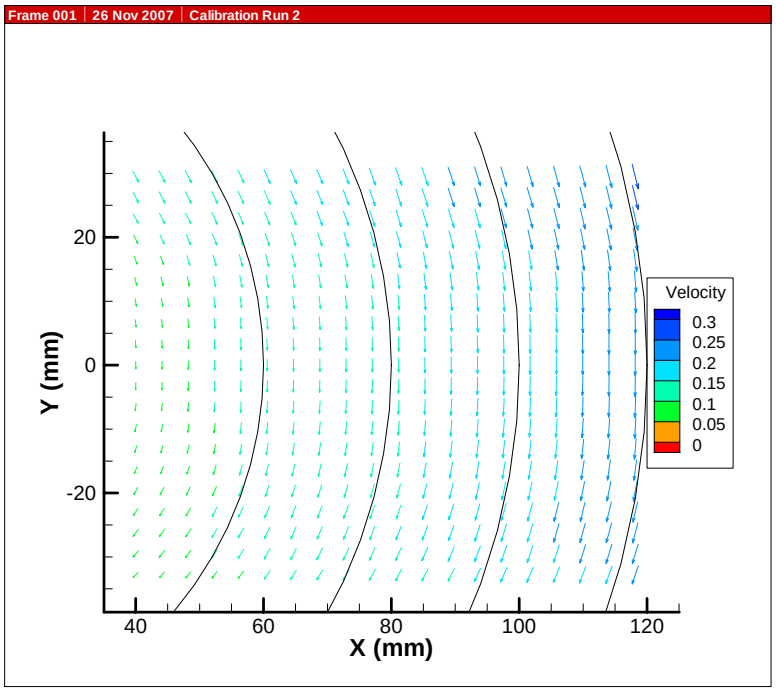

Figure 3.8: Plot of Velocity Vector Field of Verification Run 2

Vectors shown are magnitude of velocity in m/s
Center of rotation is located at (0,0)
Arcs shown are lines of constant radius

During data processing, the velocity is broken down into the x-direction velocity , *u*, and the y-direction velocity, *v*. In order to compare the PIV-measured velocities with the calculated expected velocities, the neutral line was found. The neutral line is defined as the line where the *u* velocity was minimized, meaning that velocity was contained almost entirely in the *v* component. The magnitude of the velocity, calculated using Equation 3.3, for neutral line were plotted against the radius.

$$|V| = \sqrt{u^2 + v^2} \tag{3.3}$$

The plots of the measured velocity versus the radius are shown in the figures below.

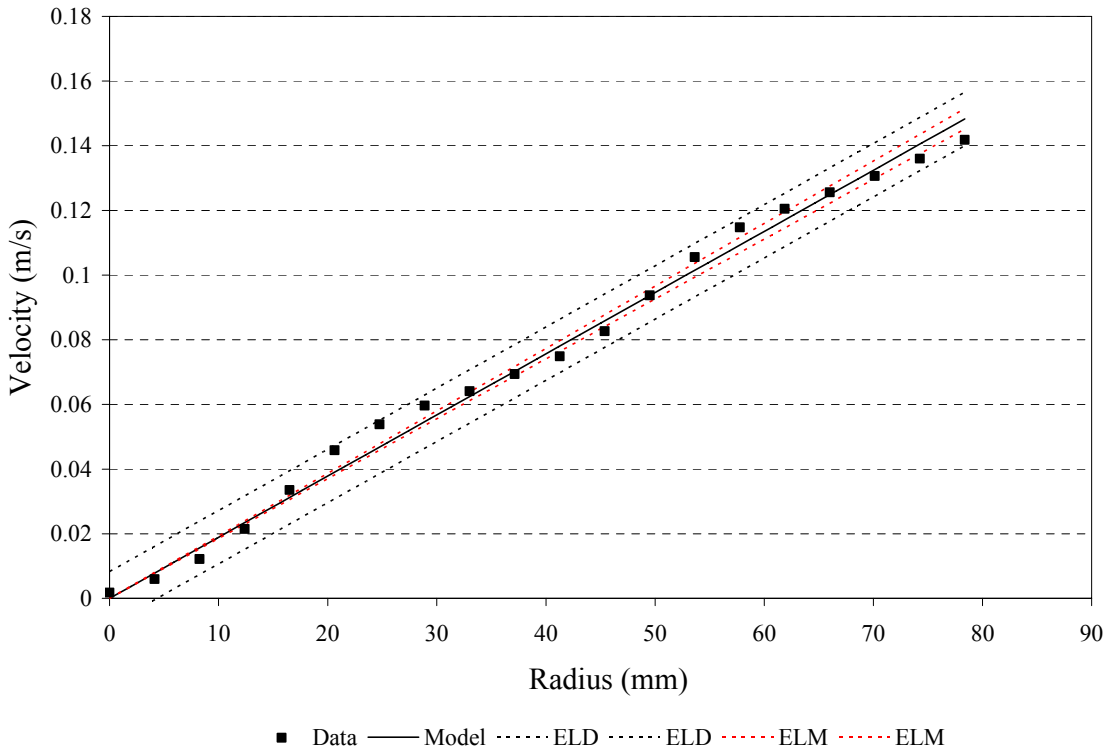

Figure 3.9: Radius versus Measured Velocity for PIV Verification Run 1

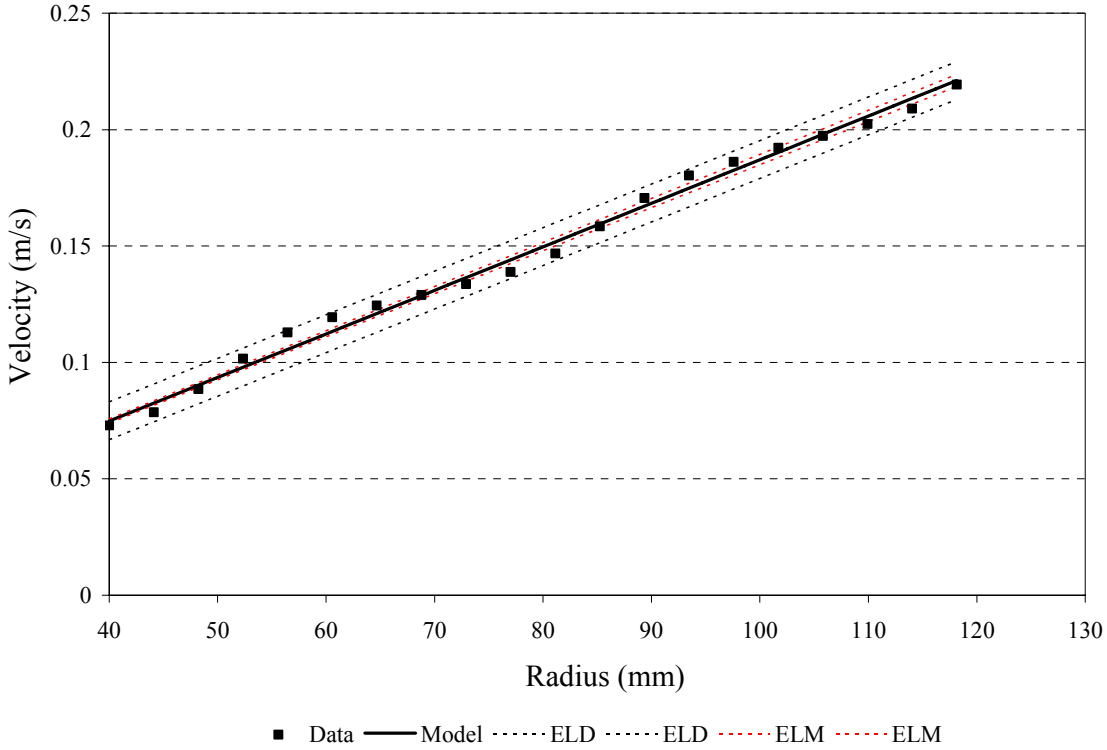

Figure 3.10: Radius versus Measured Velocity for PIV Verification Run 2

Linear interpolation was performed on the verification data. A curve was fit to the data and a constant was derived to compare with the calculated angular velocity, ω, of 1.885 radians/second. For the first verification run, a constant of 1.892 was calculated with an uncertainty of 1.58×10^{-3}. For the second verification run, a constant of 1.871 was calculated with an uncertainty of 1.74×10^{-3}. This shows that the PIV measurements agree very well with expected results.

4. EXPERIMENTAL TEST RUNS

Experimental test runs were conducted using the Georgia Tech Operating Room Simulator (ORS). Six runs were done for each case: 330 CFM - Patient at ambient, 330 CFM – Patient heated to approximately 85°F, 420 CFM – Patient at ambient, 420 CFM – Patient heated to approximately 85°F. The temperatures at the locations outlined in Section 2.1 were continuously monitored using the Agilent Benchlink Data Logger. These temperatures were used for the computational fluid dynamics (CFD) analysis. The flow into the ORS was monitored continuously to ensure that the proper airflow was supplied to the room throughout the experimental runs.

A strict procedure, shown in Appendix D, was followed for each run in order to maintain consistency for all runs. The camera and laser settings used are shown in Section 3.2. The same settings were used for all experimental runs. Representative plots for each of the four cases are shown in the figures below.

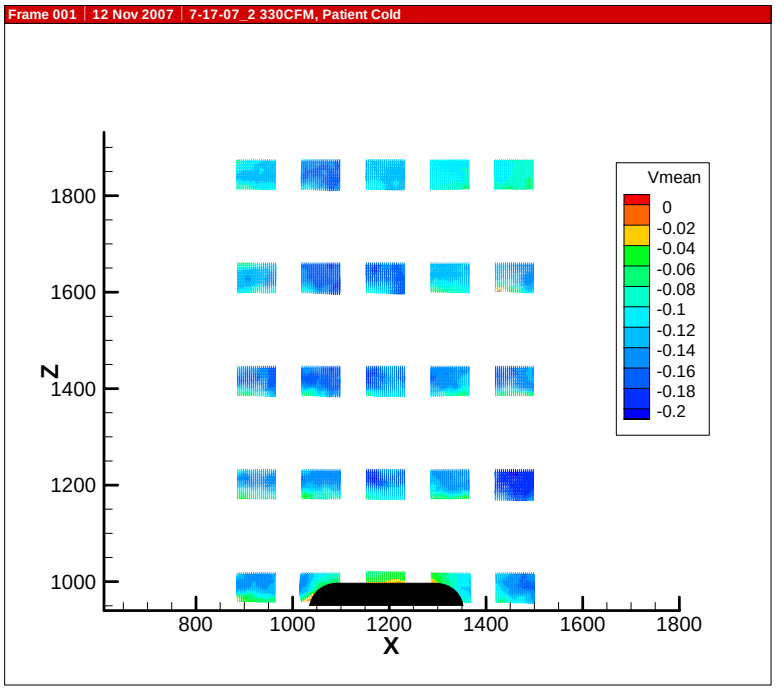

Figure 4.1: Representative Plot of 330 CFM, Patient Cold Case

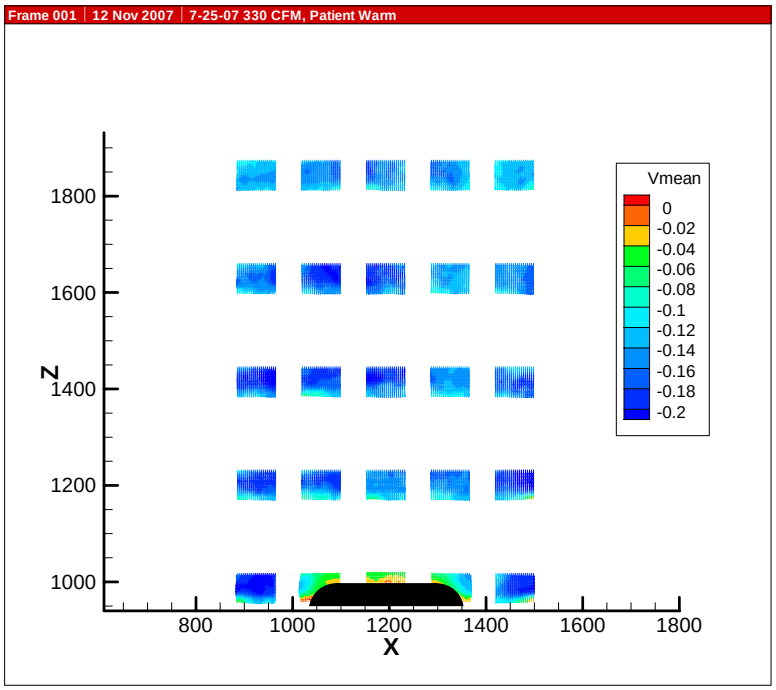

Figure 4.2: Representative Plot of 330 CFM, Patient Warm Case

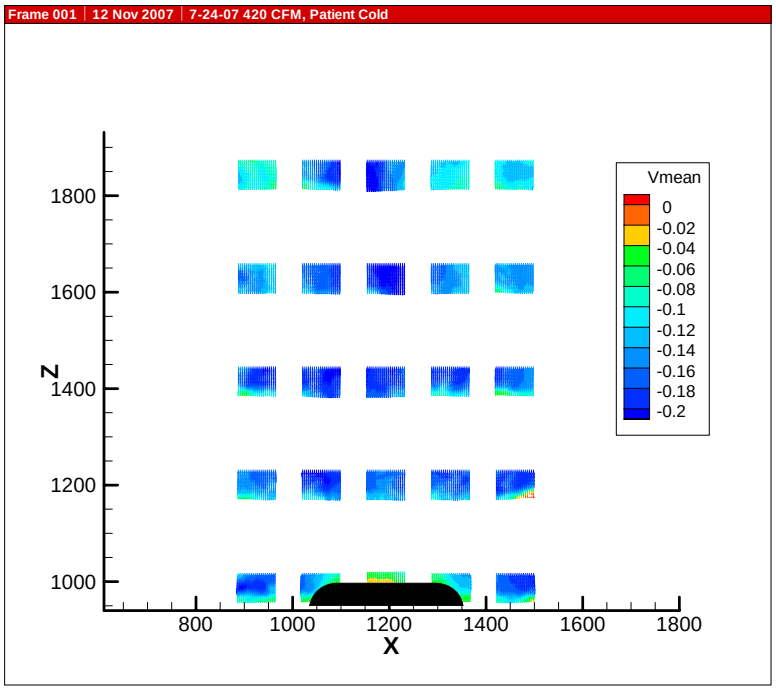

Figure 4.3: Representative Plot of 420 CFM, Patient Cold Case

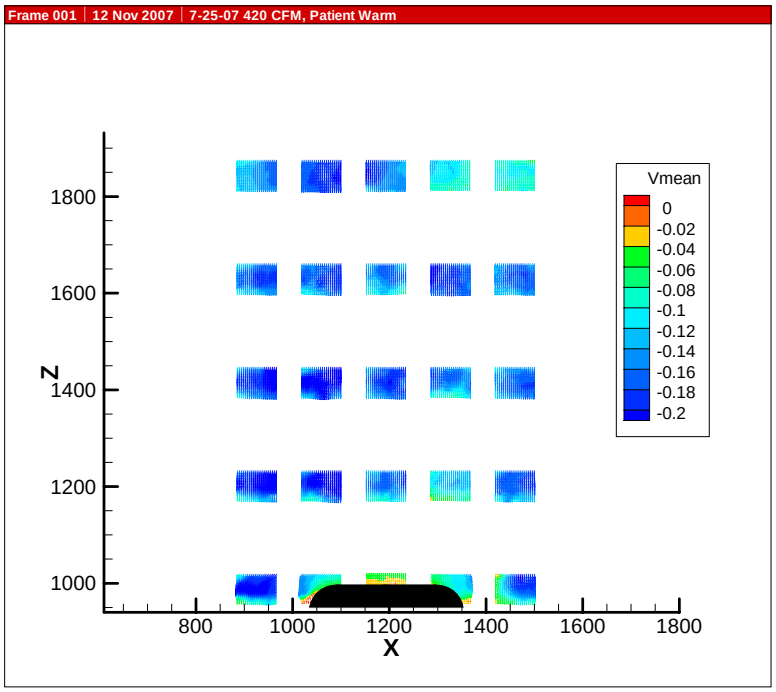

Figure 4.4: Representative Plot of 420 CFM, Patient Warm Case

As can be seen, Zone 3, directly in the center of the patient, is a stagnation region for all cases. It is difficult to see what is happening around the simulated patient. Contour plots of the six zones (zones 3, 4, 5, 7, 8, and 9) around the patient are shown below. If the plots are compared between the patient at ambient conditions to the patient

heated, a small increase in the stagnation region upstream of the patient can be observed. However, there was no evidence on any of the heated runs of a dominant buoyant thermal like those observed by Dr. Memarzadeh in his CFD analysis, which used 100°F as the temperature of the surgical site.

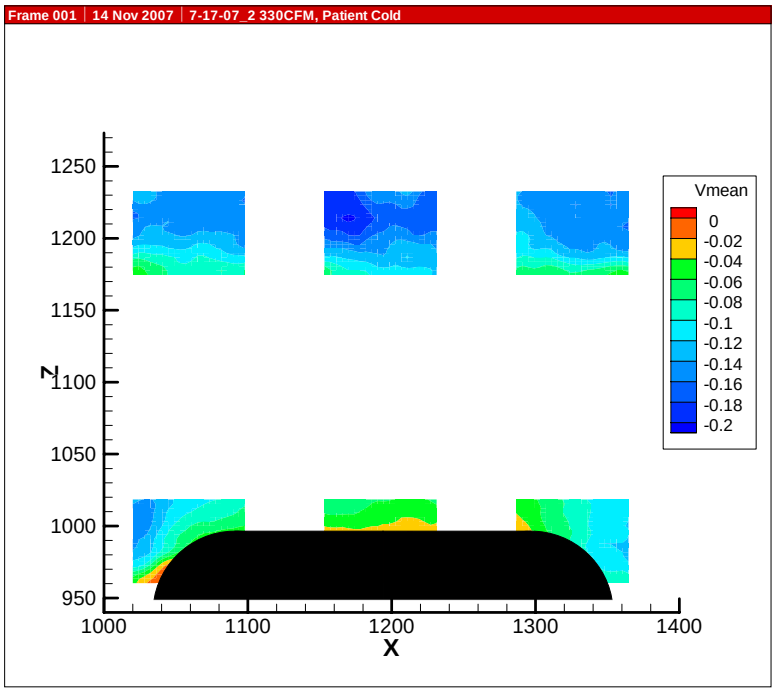

Figure 4.5: Contour Plot of Patient Region for 330 CFM, Patient Cold Case

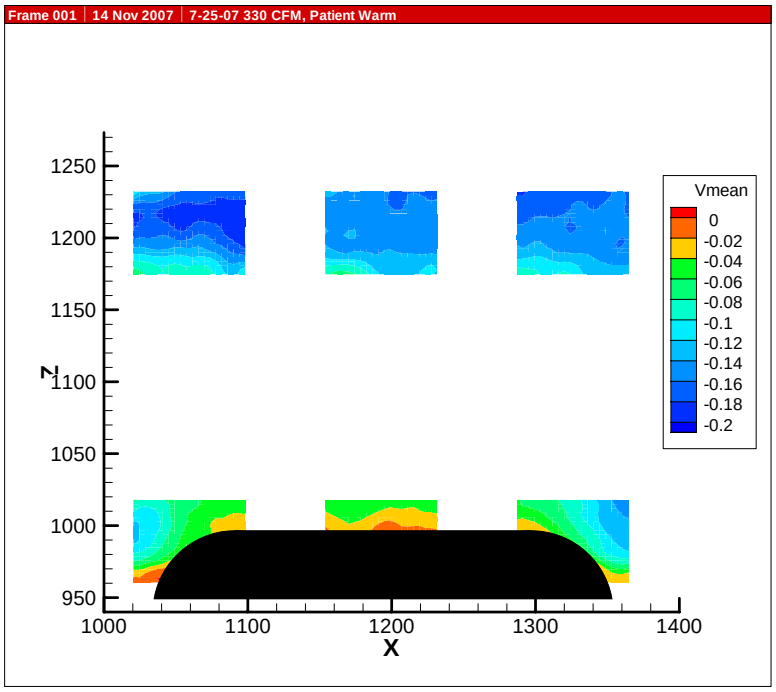

Figure 4.6: Contour Plot of Patient Region for 330 CFM, Patient Warm Case

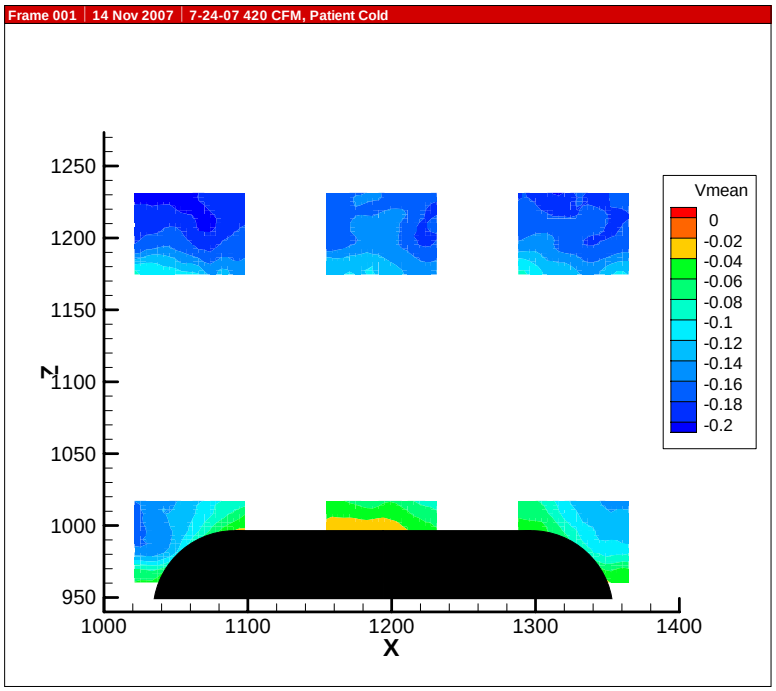

Figure 4.7: Contour Plot of Patient Region for 420 CFM, Patient Cold Case

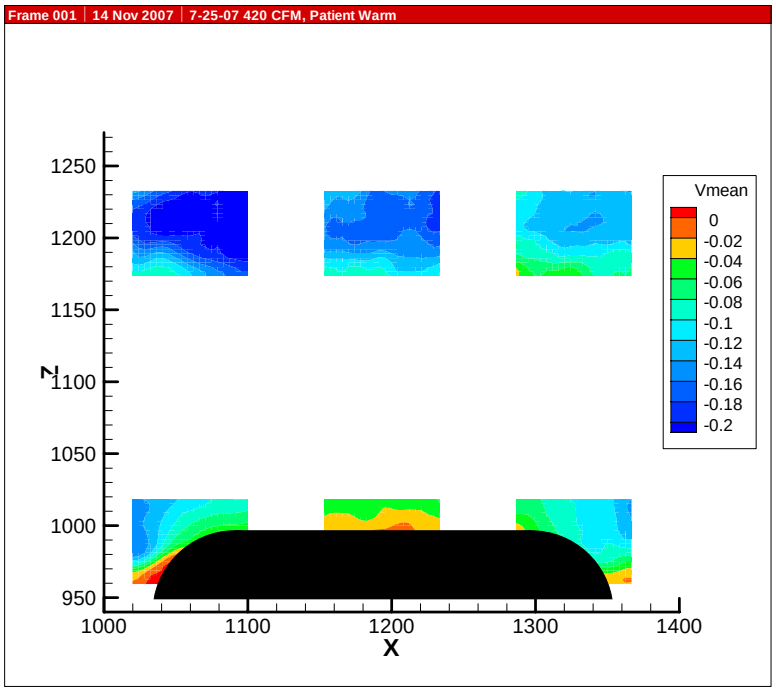

Figure 4.8: Contour Plot of Patient Region for 420 CFM, Patient Warm Case

The results from the experimental runs were very consistent. Tecplot images of all the experimental runs are included in Appendix A. In addition, average vectors for each zone were calculated for each run. These average vectors were plotted on top of each other and are supplied in Appendix B. These average plots demonstrate the consistency of the experimental runs.

4.1. Additional Test Runs

Additional test runs were conducted with the simulated patient heated to 100°F and are included in this thesis. Pictures of 330 CFM with the patient heated to 100°F and 420 CFM with the patient heated to 100°F are shown in the figures below.

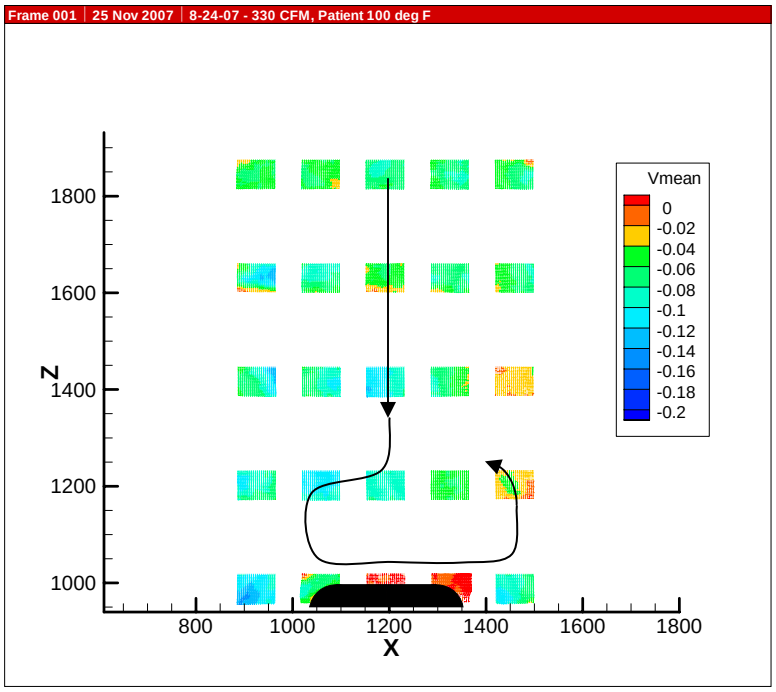

Figure 4.9: Experimental Results from 330 CFM, Patient 100°F

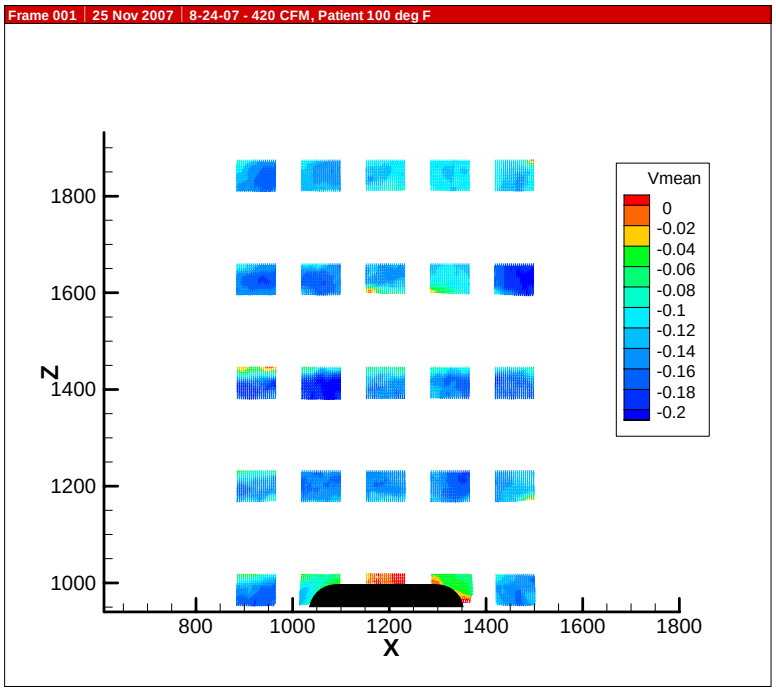

Figure 4.10: Experimental Results from 420 CFM, Patient 100°F

During the experimental run, it was noted that the buoyant flow did in fact dominate under these flow conditions. In the case of 330 CFM, with the patient heated to 100°F, there was a distinct swirl in the airflow above the patient. This results in non-symmetric flow. The general path of the flow is superimposed on Figure 4.9. Contour

plots of the patient region show a significant region of stagnation around the simulated patient, as shown in the following figures.

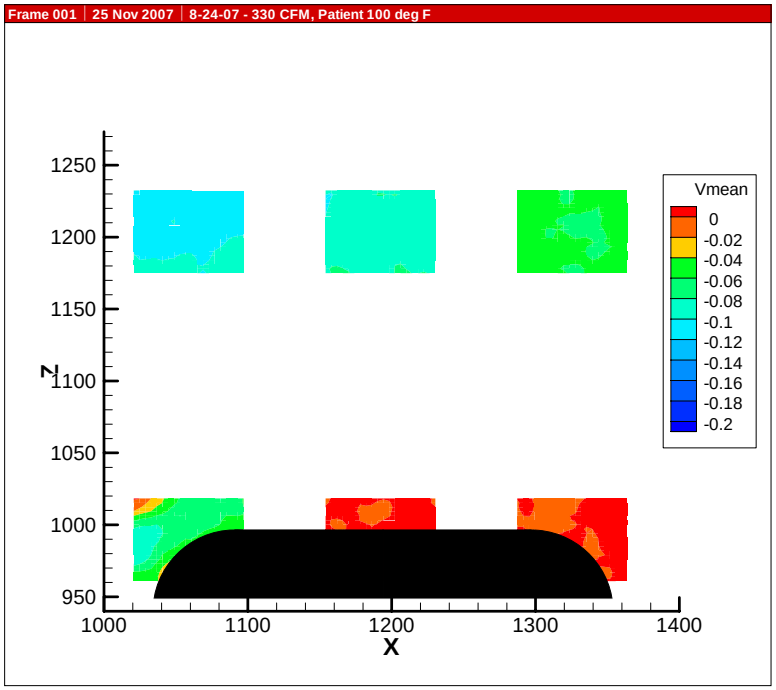

Figure 4.11: Contour Plot of Patient Region for 330 CFM, Patient 100°F

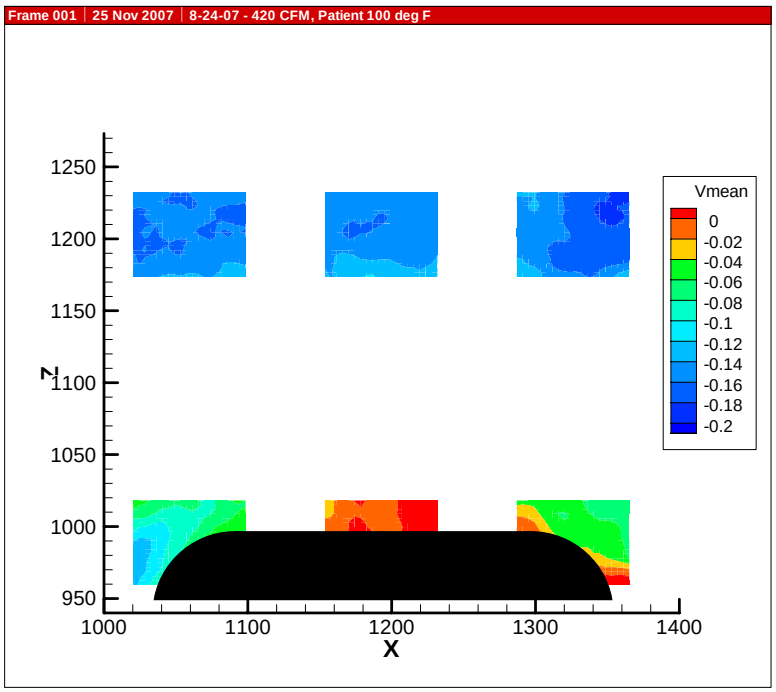

Figure 4.12: Contour Plot of Patient Region for 420 CFM, Patient 100°F

5. COMPUTATIONAL FLUID DYNAMICS ANALYSIS

As part of the investigation into the existence of a dominant buoyant flow above a surgical site under normal operating room conditions, a Computational Fluid Dynamics (CFD) analysis was conducted. FLUENT software was used to conduct this analysis. The results from the CFD analysis were qualitatively and quantitatively compared to the experimental results.

5.1. Computational Fluid Dynamics Background

The modeling of the flow inside the operating room simulator (ORS) is developed by applying the conservation equations of continuity, momentum, and energy. The choice of a suitable turbulence model is very important to obtaining reliable results. The equations used to model the turbulence in the flow are included.

5.1.1. Continuity and Momentum Equations

The conservation equations for flow in an Eulerian reference frame in the absence of external forces consist of the continuity equation [20]:

$$\frac{\partial \rho}{\partial t} + \nabla \cdot \left(\rho \vec{v}\right) = 0 \tag{5.1}$$

as well as conservation of momentum [20]:

$$\frac{\partial}{\partial t}\left(\rho \vec{v}\right) + \nabla \cdot \left(\rho \vec{v}\vec{v}\right) = -\nabla P + \rho \vec{g} - \nabla \cdot \left(\bar{\bar{\tau}}\right) \tag{5.2}$$

where ρ is the density, $\vec{v}$ is the velocity vector, P is the static pressure, ρg is the gravitational body force, and $\bar{\bar{\tau}}$ is the stress tensor.

5.1.2. Energy Continuity Equation

The energy equation can be written as:

$$\frac{\partial}{\partial t}(\rho E) = -(\nabla \cdot E) - (\nabla \cdot q) - \left(\nabla \cdot \left[\bar{\bar{\tau}} \cdot \vec{v}\right]\right) \quad \textbf{(5.3)}$$

where E is the total energy of the flow, defined in the following equation.

$$E = h - \frac{p}{\rho} + \frac{V^2}{2} \quad \textbf{(5.4)}$$

where h is the enthalpy of the flow, p is the pressure of the flow, ρ is the density of the air, and V is the magnitude velocity of the flow.

5.1.3. Turbulence Modeling

The realizable k-ε model was used to model the turbulence in the fluid flow for this study. The realizable k-ε model is a more sophisticated model than the standard k-ε model, which is used extensively in CFD. The standard k-ε model is a semi-empirical model based on writing transport equations for the turbulence kinetic energy (k) and the turbulence dissipation rate (ε). The standard k-ε model, however, over predicts the effects of eddy viscosity. The realizable k-ε model was developed by Shih [21] to correct this issue. The turbulence kinetic energy, k, and its rate of dissipation, ε, for the realizable turbulent transport condition are obtained from the following equations [21]:

$$\frac{\partial}{\partial t}(\rho k) + \frac{\partial}{\partial x_j}(\rho k u_i) = \frac{\partial}{\partial x_j}\left[\left(\mu + \frac{\mu_t}{\sigma_k}\right)\frac{\partial k}{\partial x_j}\right] + G_k + G_b - \rho\varepsilon - Y_M \quad \textbf{(5.5)}$$

$$\frac{\partial}{\partial t}(\rho \varepsilon) + \frac{\partial}{\partial x_j}(\rho \varepsilon u_j) = \frac{\partial}{\partial x_j}\left[\left(\mu + \frac{\mu_t}{\sigma_\varepsilon}\right)\frac{\partial \varepsilon}{\partial x_j}\right] + \rho C_1 S\varepsilon - \rho C_2 \frac{\varepsilon^2}{k + \sqrt{\upsilon\varepsilon}} + C_{1\varepsilon}\frac{\varepsilon}{k}C_{3\varepsilon}G_b \quad \textbf{(5.6)}$$

The terms that appear in these equations are defined next. G_k is the generation of turbulent kinetic energy due to the mean velocity gradients and is defined in the following equation.

$$G_k = -\rho\overline{u_i' u_j'}\frac{\partial u_j}{\partial x_i} \quad \textbf{(5.7)}$$

G_b is the generation of turbulent kinetic energy due to buoyancy and is defined for perfect gases as:

$$G_b = -g_i \frac{\mu_t}{\rho \mathrm{Pr}_t} \frac{\partial \rho}{\partial x_i} \tag{5.8}$$

Y_M is the contribution of the fluctuating dilation in compressible turbulence to the overall dissipation rate.

$$Y_M = 2\rho \cdot \varepsilon \cdot M_t^2 \tag{5.9}$$

where M_t is the turbulent Mach number.

$C_{1\varepsilon}$, C_2, are constants, and σ_k and σ_ε are the turbulent Prandtl numbers for k and ε, respectively. The following values are used during FLUENT analysis $C_{1\varepsilon} = 1.44, C_2 = 1.9, \sigma_k = 1.0, \sigma_\varepsilon = 1.2$ [21].

$C_{3\varepsilon}$ is defined as:

$$C_{3\varepsilon} = \tanh\left|\frac{u_=}{u_\perp}\right| \tag{5.10}$$

where $u_=$ is the component of the flow velocity parallel to the gravitational vector and $u_\perp$ is the component of the flow velocity perpendicular to the gravitational vector.

C_1 is defined by the following equation [21]:

$$C_1 = \max\left[0.43, \frac{\sqrt{2S_{ij}S_{ij}}\,\frac{k}{\varepsilon}}{\sqrt{2S_{ij}S_{ij}}\,\frac{k}{\varepsilon} + 5}\right] \tag{5.11}$$

5.2. Computational Fluid Dynamics Analysis Methodology

The boundary conditions used were taken from measurements collected during the experimental runs. The thermocouples used to collect these data points were located

in the room as shown in Figure 2.5 (Section 2). Several calculations were done with the experimental data in order to aid with the CFD analysis.

The Boussinesq density was found for each of the cases. The Boussinesq approximation of the density helps get a faster convergence for buoyancy-driven flows than when density is defined as a function of temperature. The Boussinesq model in FLUENT treats the density as a constant value in all solved equations except for the buoyancy term in the momentum equation. The Boussinesq approximation is defined as [20]:

$$\rho_B = \rho_o(1 - \beta \cdot \Delta T) \quad \textbf{(5.12)}$$

where ρ_o is the ambient density of air (1.2 kg/m^3), β is the thermal expansion coefficient, which was previously defined, and ΔT is the temperature difference between the inlet air and the surface of the simulated patient.

The thermal coefficient of expansion, β, is defined by the equation below, which simplifies to the inverse of the absolute temperature for an ideal gas.

$$\beta = -\frac{1}{\rho}\frac{\partial \rho}{\partial T} = \frac{1}{T} \quad \textbf{(5.13)}$$

The boundary conditions used for the four different cases are shown in the following table.

Table 5.1: Operating Conditions

	330 CFM, Patient Cold	330 CFM, Patient Warm	420 CFM, Patient Cold	420 CFM, Patient Warm
u_{in} (m/s)	0.064	0.064	0.081	0.081
T_{in} (K)	288.5	288.8	288.5	288.6
T_{room} (K)	288.9	289.4	288.9	289.1
T_{out} (K)	289.1	289.5	289.0	289.3
$T_{patient}$ (K)	288.9	303.6	289.0	304.5
β (1/K)	0.00346	0.00346	0.00346	0.00346
ρ_B (kg/m^3)	1.22	1.16	1.22	1.16
Ar	0.15	36.09	0.23	24.07

The Archimedes numbers calculated are shown here for reference only.

The heat flux through the walls was calculated from the experimental data in order to include it in the CFD analysis. This was done by employing the following equation.

$$\dot{q} = \frac{\dot{Q}}{A} = \dot{m} C_p (T_{out} - T_{in}) \quad \textbf{(5.14)}$$

where $\dot{q}$ is the heat flux per unit area, $\dot{Q}$ is the total heat flux, A is the wall area, $\dot{m}$ is the mass flow rate of the air in the room, C_p is the specific heat at constant pressure, and T_{out} and T_{in} are taken from the measured boundary conditions. See Appendix F for heat flux calculations done with Engineering Equation Solver software.

The heat flux through the ORS walls was found to be 7.05 W/m^2 and was applied as a boundary condition to the model. An illustration of the boundary conditions taken from the experimental data and applied to the CFD analysis is shown in the figure below.

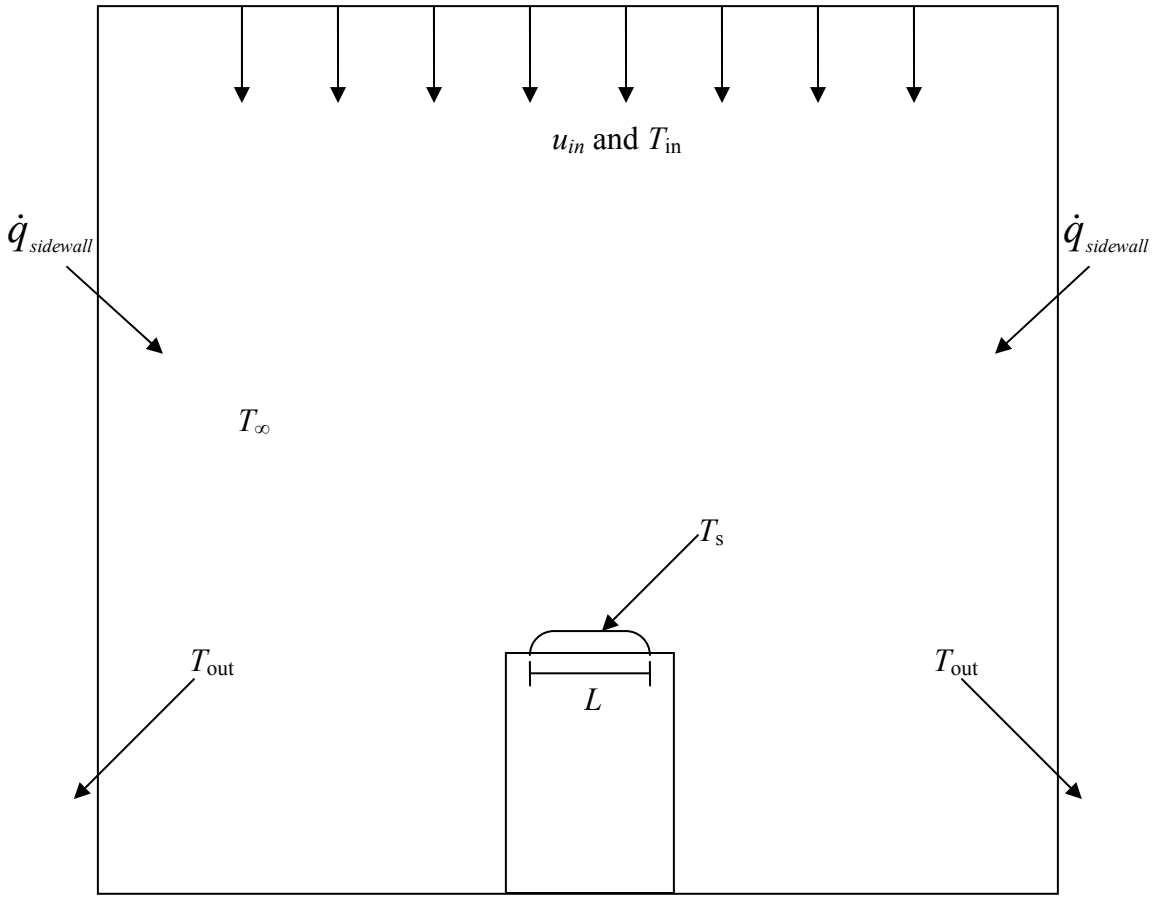

Figure 5.1: Definition of Boundary Conditions Used for Analysis

A 3-dimensional model of the Georgia Tech ORS was developed in Gambit and analyzed in FLUENT. The model was dimensioned to the same dimensions as those of the physical ORS. A Tet-hybrid mesh was used for the mesh construction in Gambit. The mesh consisted of 554,093 cells with the mesh being very dense around the simulated patient. The cell volumes were between 8×10^{-8} and 8×10^{-5} m^3. A picture of the mesh is shown in Figure 5.2 below. The interior mesh is not shown for clarity.

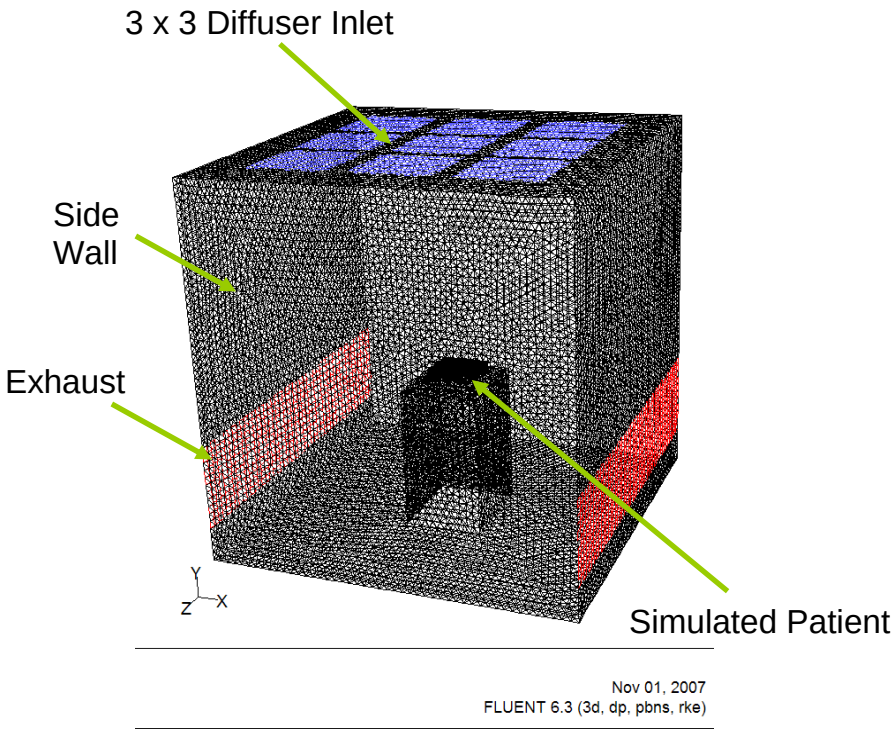

Figure 5.2: Gambit Mesh of ORS

Several different meshes were tested before the mesh used for this analysis was developed, including several structured grid. The structured grids, however, were unsuccessful in meshing the geometry of the ORS. The unstructured Tet-hybrid mesh was able to efficiently model the flow. In practice, an unstructured Tet-hybrid mesh would be the easiest mesh to use, and in simulating realistic and complicated geometry, the unstructured grid is likely to be the only feasible option.

To couple the pressure and velocity and ensure continuity is satisfied, the SIMPLE algorithm was employed to obtain a numerical solution of the momentum equations. The SIMPLE algorithm in FLUENT uses a procedure similar to the one outlined by Rhie and Chow [24]. Using this method, the face value of velocity is not averaged linearly. Momentum-weighted averaging, which uses weighting factors, is performed.

The PRESTO! (PREssure STaggering Option) solver was used for the pressure continuity solver. This solver uses a staggered control volume about the face to compute the staggered pressure [25]. This solver is recommended by Fluent for buoyant flows [22]. The second order momentum, turbulent kinetic energy, turbulent dissipation, and energy discretizations were utilized to discretize the governing equations. The numerical solution was found to a convergence accuracy of 1 x 10^{-4} (kg/s and m/s) for the continuity and velocity terms for each of the four cases. In addition, a convergence accuracy of 1 x 10^{-7} W was achieved for the energy equation.

5.3. Computational Fluid Dynamics Analysis Results

The data from FLUENT was exported and Tecplot was employed to visualize the flow inside the ORS model. The flow of the CFD results in the same plane as the experimental results is shown the following figures.

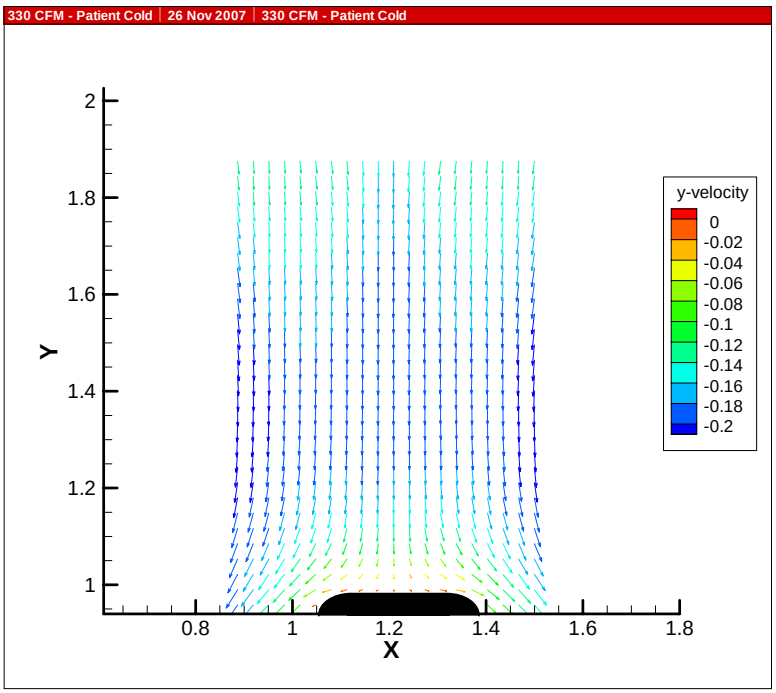

Figure 5.3: CFD Results for 330 CFM, Patient Cold in Region of Experimental Results

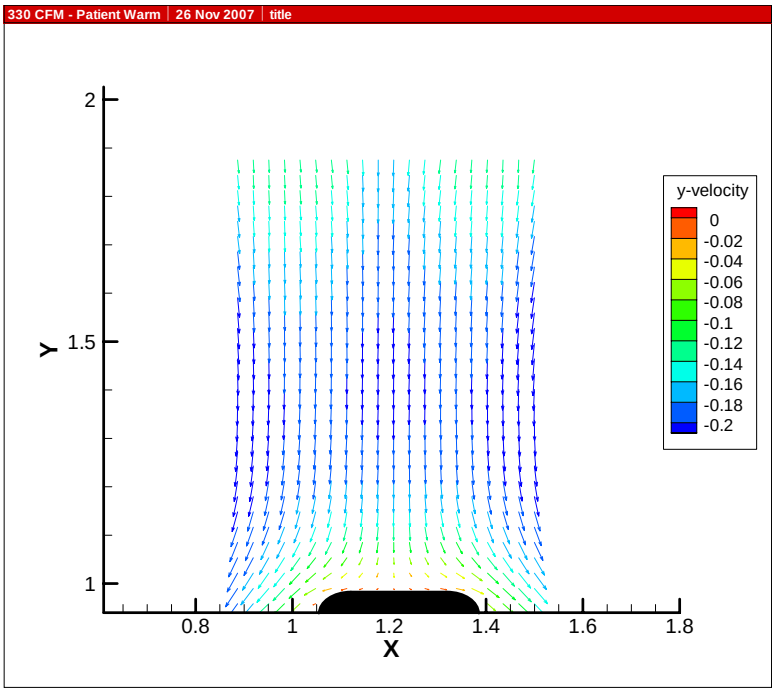

Figure 5.4: CFD Results for 330 CFM, Patient Warm in Region of Experimental Results

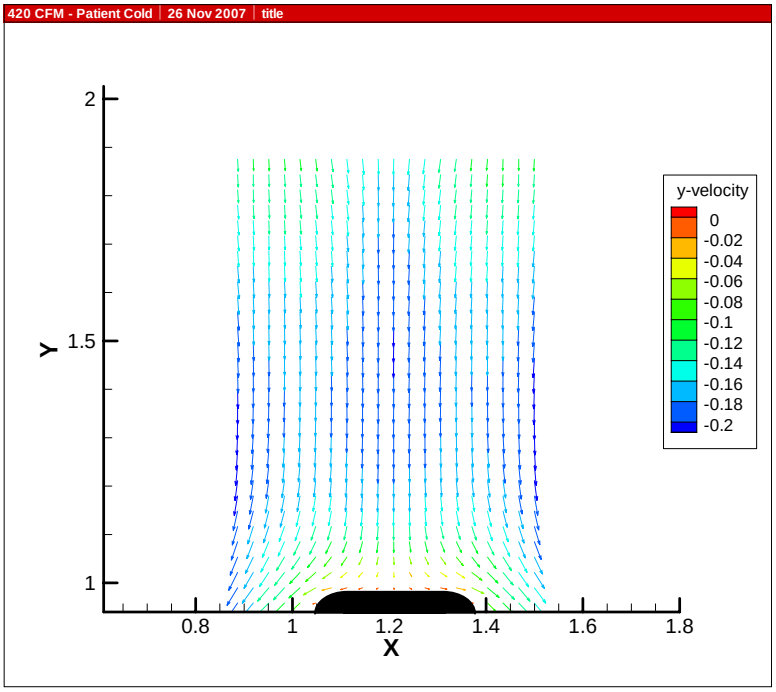

Figure 5.5: CFD Results for 420 CFM, Patient Cold in Region of Experimental Results

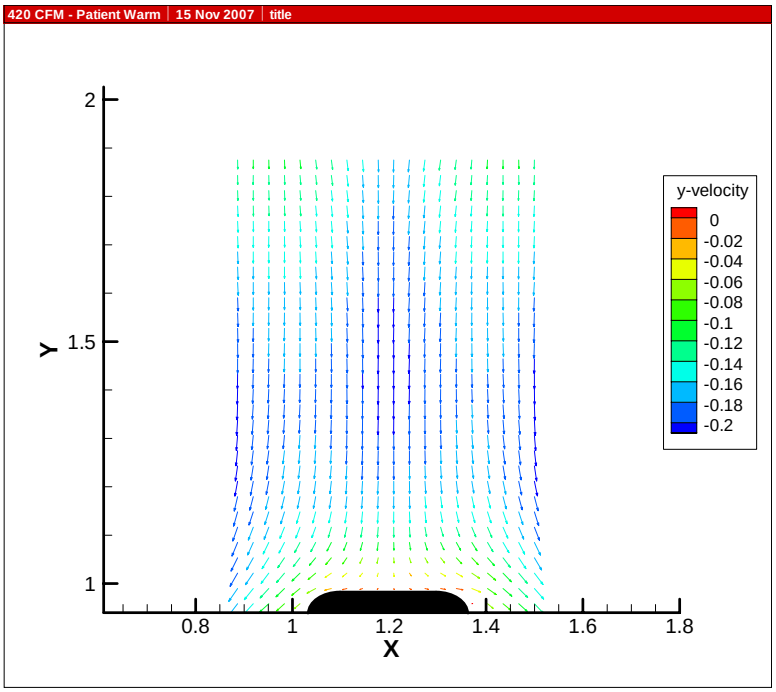

Figure 5.6: CFD Results for 420 CFM, Patient Warm in Region of Experimental Results

As can be seen in these results, the flow is predominantly downward vertical flow with a small stagnation region upstream of the patient. There is not a significant difference in the stagnation region between the patient heated and the patient at ambient conditions. This indicates that a dominant buoyant thermal does not exist above a surgical site under these conditions. Tecplot windows of the entire plane of the experimental results for the four cases are included in Appendix C.

5.4. Comparison with Experimental Results

A comparison of the experimental results and the CFD results was performed to determine how well the two agree. This was accomplished by partitioning the CFD results into the same zones as those used for the PIV measurements using Tecplot. The numbers determined by Tecplot linear interpolation can be written to a text file. Using those numbers, it is possible to find an average velocity (in the *u* and *v* components) for

each zone using Excel. These numbers can then be directly compared with the average velocities obtained through the experimental runs.

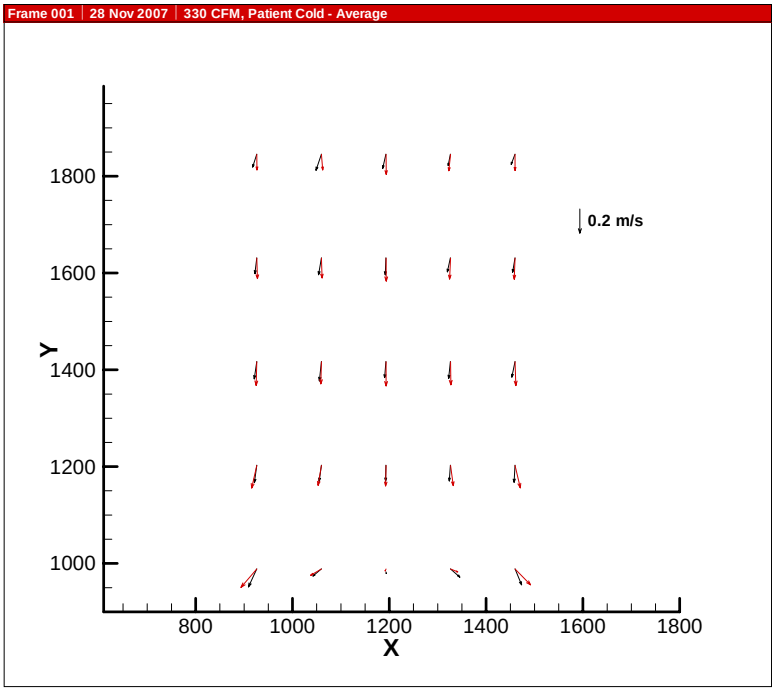

Figure 5.7: Comparison of CFD Zone Averages with Experimental Zone Averages for 330 CFM, Patient Cold Case

Experimental Zone Averages are shown in Black
CFD Zone Averages are shown in Red

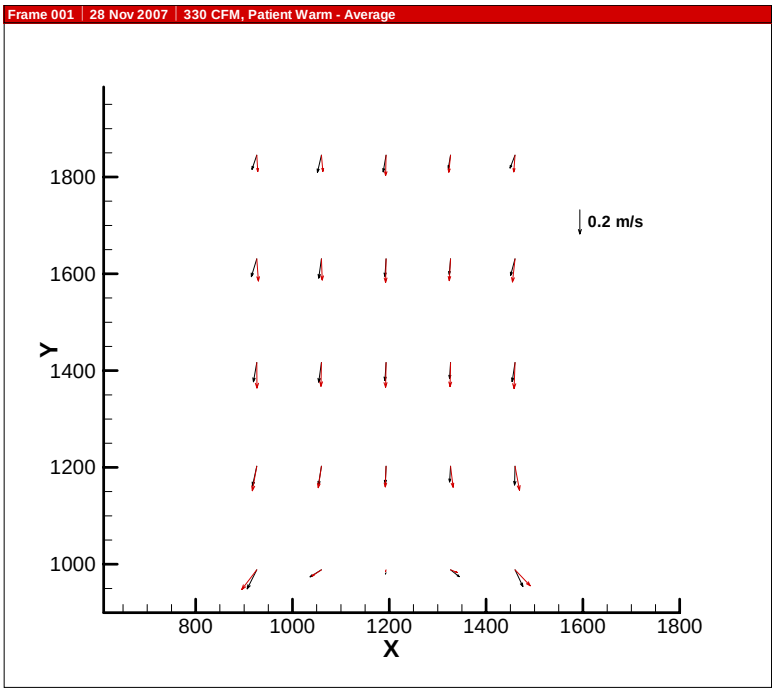

Figure 5.8: Comparison of CFD Zone Averages with Experimental Zone Averages for 330 CFM, Patient Warm Case

Experimental Zone Averages are shown in Black
CFD Zone Averages are shown in Red

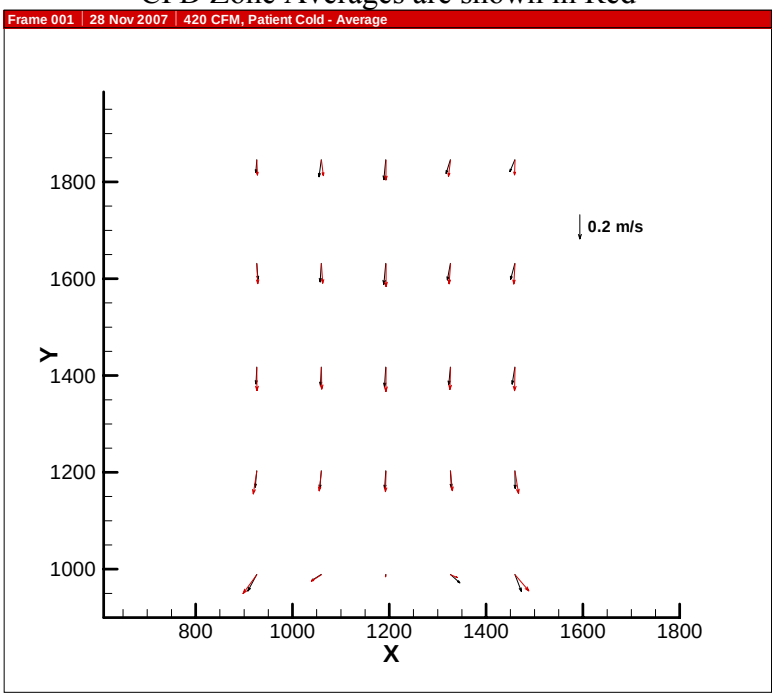

Figure 5.9: Comparison of CFD Zone Averages with Experimental Zone Averages for 420 CFM, Patient Cold Case

Experimental Zone Averages are shown in Black
CFD Zone Averages are shown in Red

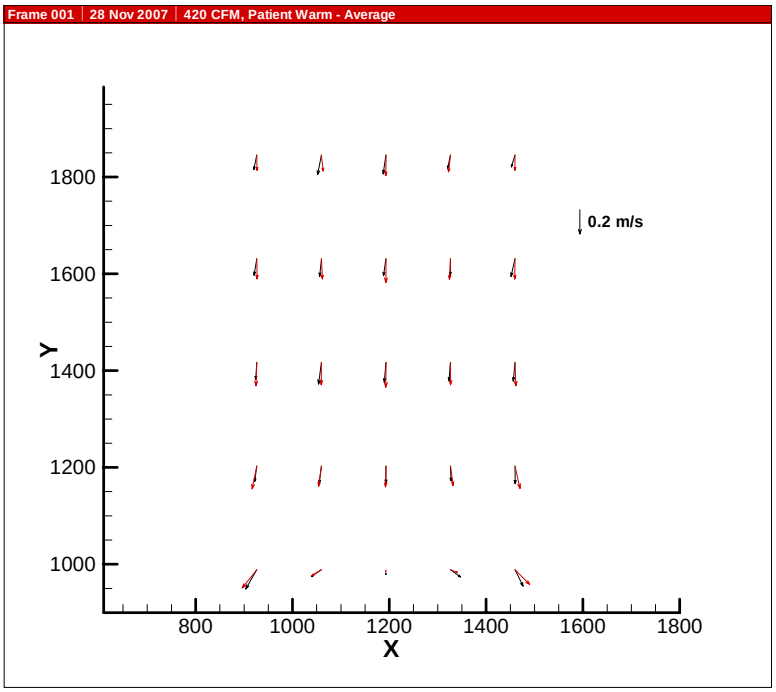

Figure 5.10: Comparison of CFD Zone Averages with Experimental Zone Averages for 420 CFM, Patient Warm Case

Experimental Zone Averages are shown in Black
CFD Zone Averages are shown in Red

As can be seen from viewing Figures 5.7 through 5.10, the CFD results agree very well with the experimental results in both magnitude and direction of the average vectors in each experimental zone.

In addition to the qualitative comparison of the results shown above, a quantitative comparison was done. This was done by taking the difference between the FLUENT results and the experimental results. This number was squared and the sum of the difference squared was found for all 25 zones and then divided by the average velocity found by adding the two results and dividing by 2. The overall error for the whole area was found by using Equation 5.11.

$$RMS = \frac{\sqrt{\Sigma(V_{yCFD} - V_{y\exp})^2}}{\sum V_{avg}} \qquad \textbf{(5.15)}$$

The errors found by using this analytical comparison are shown in the table below.

Table 5.2: Root-Mean Squared Error Between Experimental Results and CFD Results

Case	RMS Error
330 CFM, Patient Ambient	6.1 %
330 CFM, Patient Heated	5.1 %
420 CFM, Patient Ambient	4.2 %
420 CFM, Patient Heated	4.4 %

It is interesting to note that the results obtained from a conventional and commercially available CFD modeling and simulation package were in good agreement with the results obtained from experiments.

6. CONCLUSION

Surgical site infections are a significant area of concern for surgical patients. Under recommended hospital operating room ventilation conditions, a buoyant flow may develop from the heat of the surgical site and may help prevent infections. The aim of this thesis was to determine the role of the buoyant flow in preventing antibodies and bacteria from entering the surgical site during an operation. An experimental and a numerical study were conducted as part of this investigation. The cases considered were for 330 cubic feet per minute (CFM) and 420 CFM volumetric airflow rates entering the experimental setup. A simulated patient was either heated or left at ambient conditions to determine what effect the patient's heat has on airflow impinging on the surgical site.

The Georgia Tech Operating Room Simulator (ORS) was used extensively in the collection of experimental data. The ORS is arranged to emulate the parallel downward airflow system commonly found in hospital operating rooms. Data were collected from 25 zones upstream of a simulated patient in the ORS employing Particle Image Velocimetry (PIV) technology. The results of the experimental runs indicate that when the surgical site is maintained at a realistic temperature (85°F), the buoyancy probably did not play a dominant role in preventing the airflow (which could possibly be carrying infectious particles) from impinging directly on the surgical site during steady state conditions. However, when the temperature of the surgical site was raised to 100°F, a dominant buoyant flow was observed.

Temperature and flow measurements were taken from the experimental runs and applied as boundary conditions for the numerical model. A 3-D model of the ORS was

developed and analyzed using FLUENT software. It is notable that a relatively conventional CFD modeling and simulation package was able to produce results that agreed very well with the experimental data.

From the results obtained as part of this study, it was observed that a buoyant flow generated from a patient's own body heat did not seem to protect the surgical site from impinging airflow. Therefore, it is recommended that a method of active patient air control be developed. The Georgia Tech ORS should be further utilized to determine the effect active patient air control has on airflow patterns in a hospital operating room.

It is acknowledged that no attempt was made to track simulated infectious particles in this research. Such an effort would be far beyond the current scope of effort and resources. It is recommended that experimental particle tracking imaging be conducted to evaluate the effectiveness of various air distribution designs in protecting the patient. Such experimental results should be compared with particle tracking simulations, which will require transient CFD simulations that are far outside the scope of this work.

APPENDIX A – EXPERIMENTAL TEST RUN RESULTS

330 CFM – Patient Cold

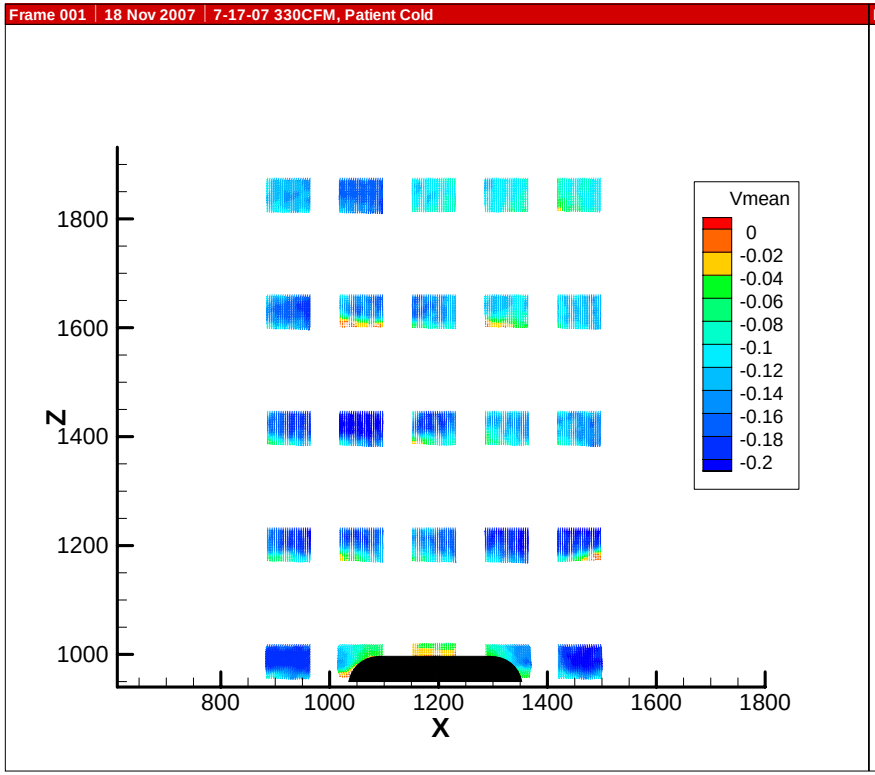

Figure A.1: Detail Velocity Vectors for 330 CFM, Patient Cold Experimental Run Performed on 7-17-2007

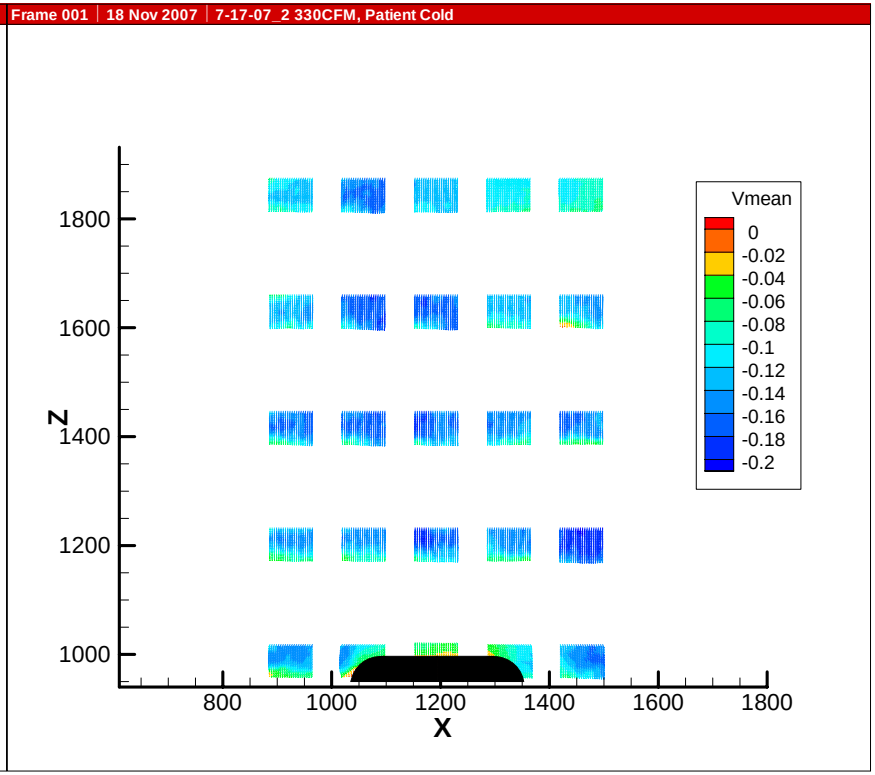

Figure A.2: Detail Velocity Vectors for 330 CFM, Patient Cold Experimental Run Performed on 7-17-2007

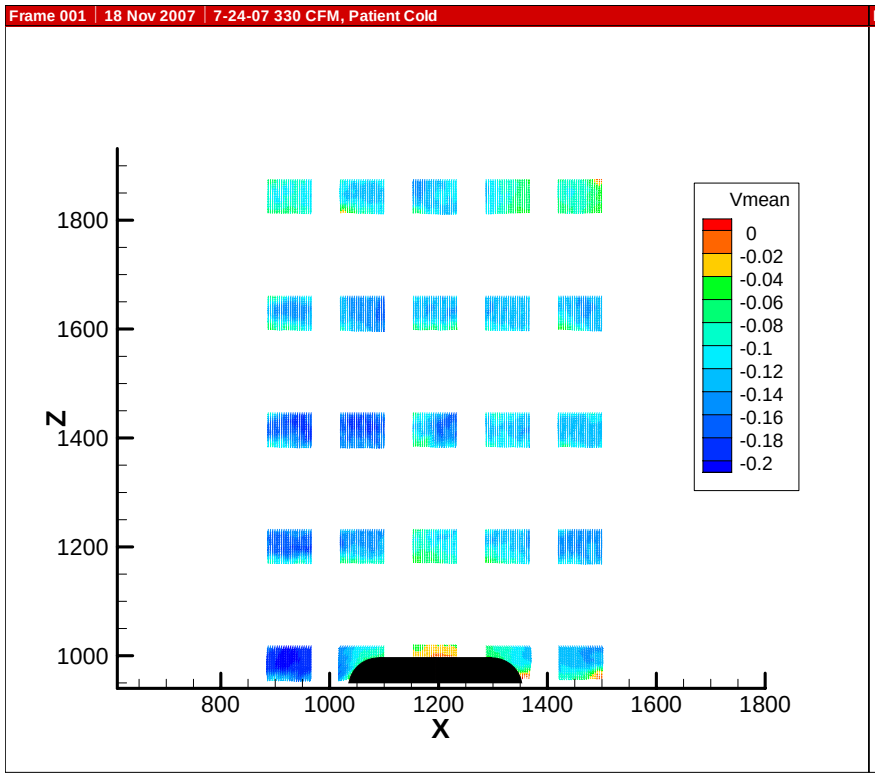

Figure A.3: Detail Velocity Vectors for 330 CFM, Patient Cold Experimental Run Performed on 7-24-2007

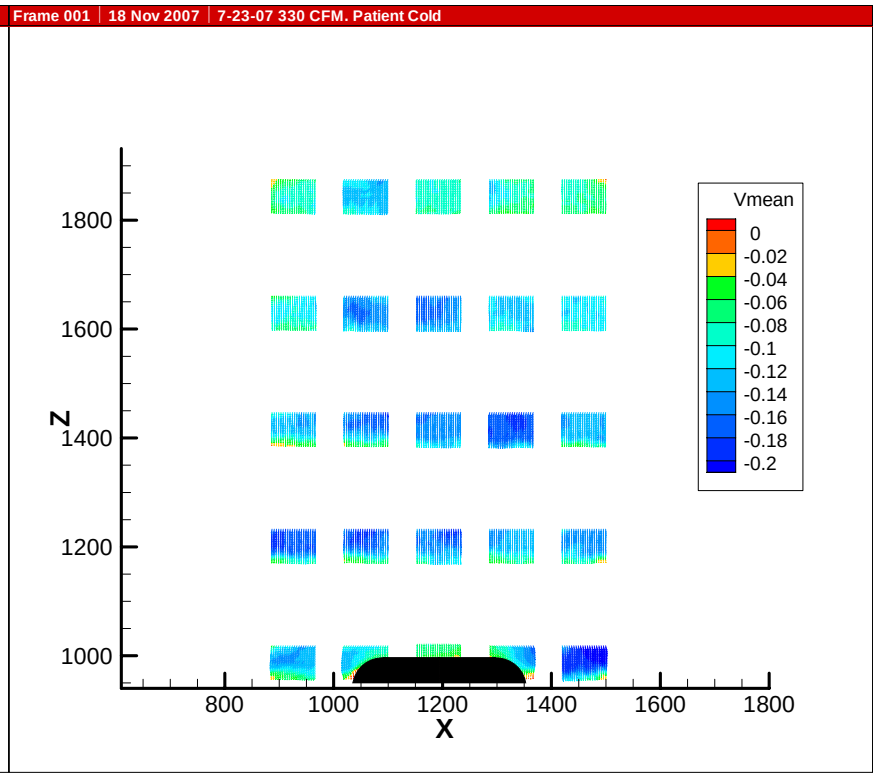

Figure A.4: Detail Velocity Vectors for 330 CFM, Patient Cold Experimental Run Performed on 7-28-2007

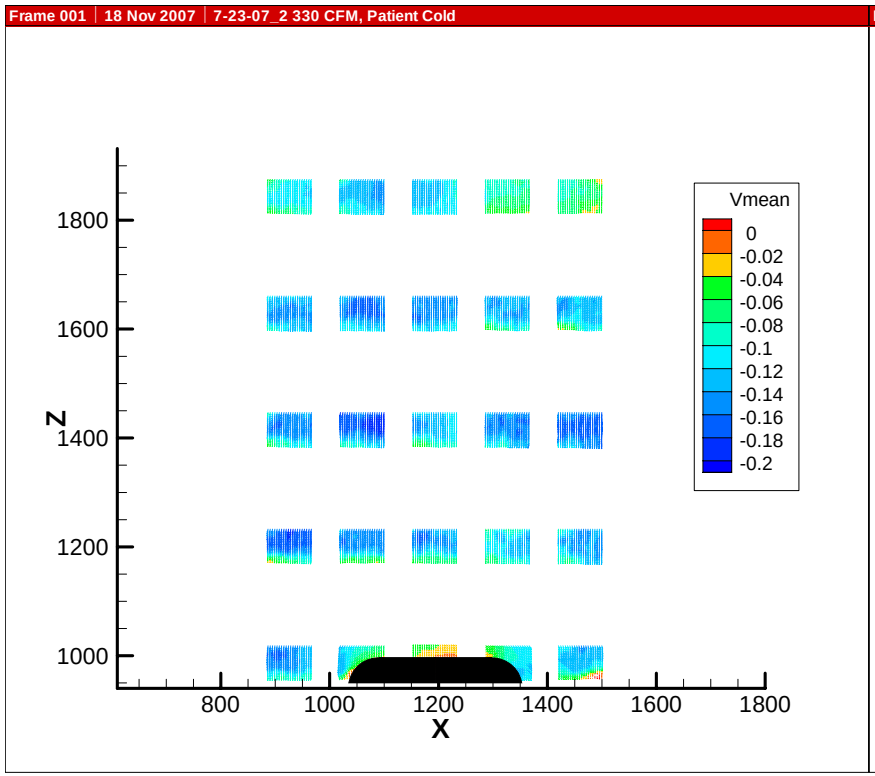

Figure A.5: Detail Velocity Vectors for 330 CFM, Patient Cold Experimental Run Performed on 7-28-2007

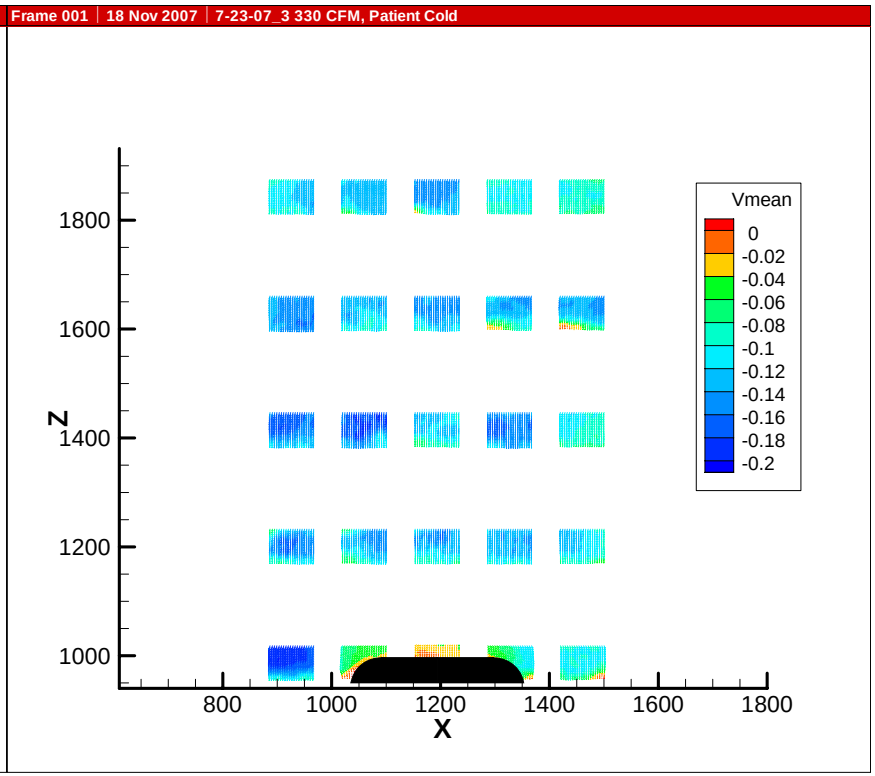

Figure A.6: Detail Velocity Vectors for 330 CFM, Patient Cold Experimental Run Performed on 7-28-2007

330 CFM – Patient Warm

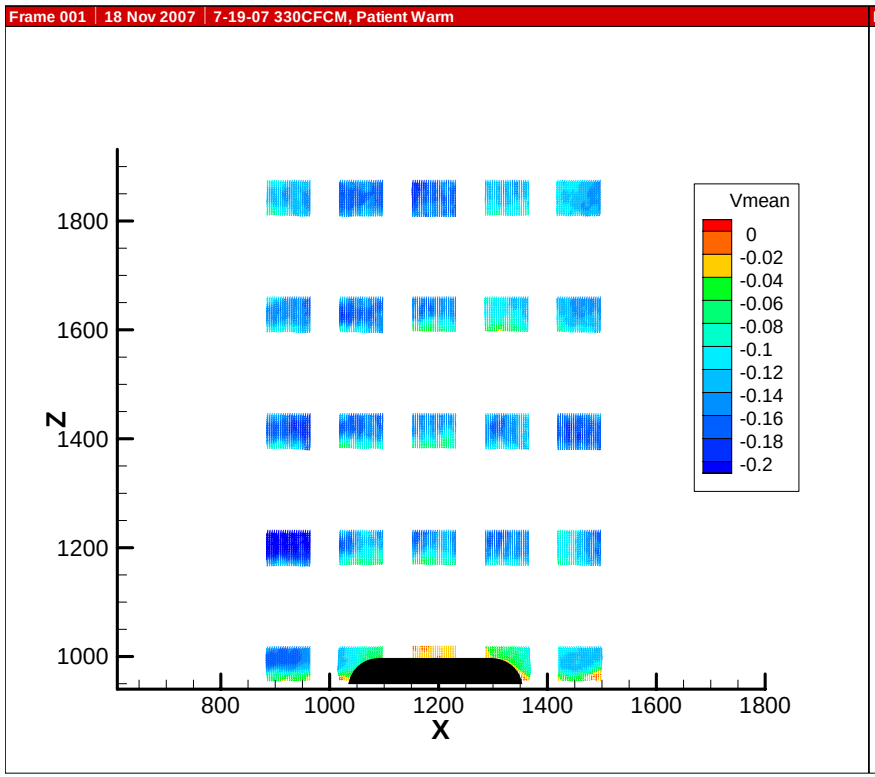

Figure A.7: Detail Velocity Vectors for 330 CFM, Patient Warm Experimental Run Performed on 7-19-2007

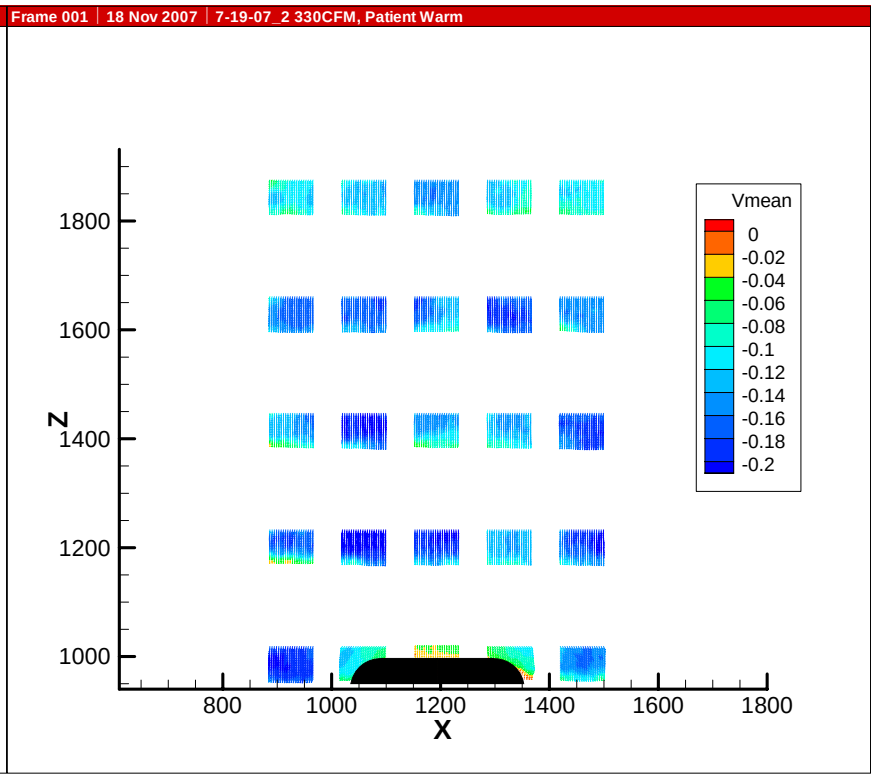

Figure A.8: Detail Velocity Vectors for 330 CFM, Patient Warm Experimental Run Performed on 7-19-2007

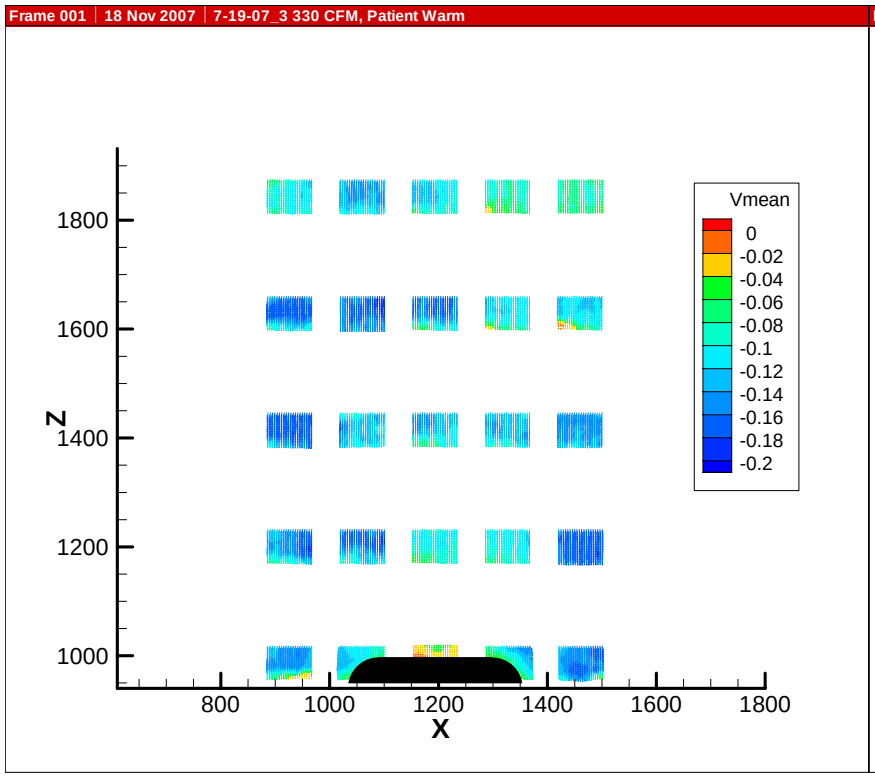

Figure A.9: Detail Velocity Vectors for 330 CFM, Patient Warm Experimental Run Performed on 7-19-2007

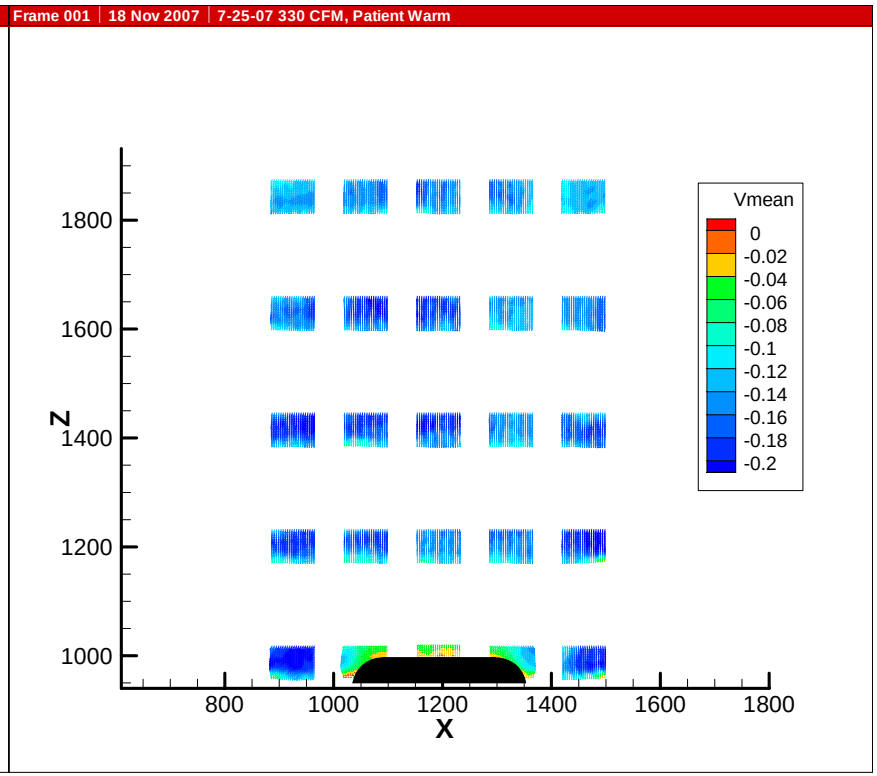

Figure A.10: Detail Velocity Vectors for 330 CFM, Patient Warm Experimental Run Performed on 7-25-2007

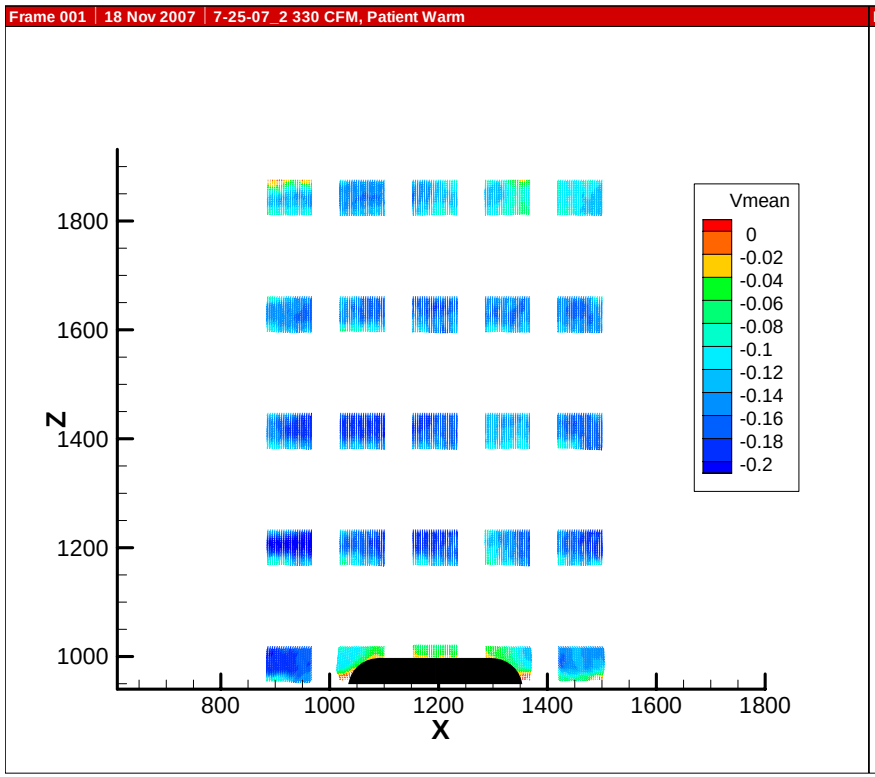

Figure A.11: Detail Velocity Vectors for 330 CFM, Patient Warm Experimental Run Performed on 7-25-2007

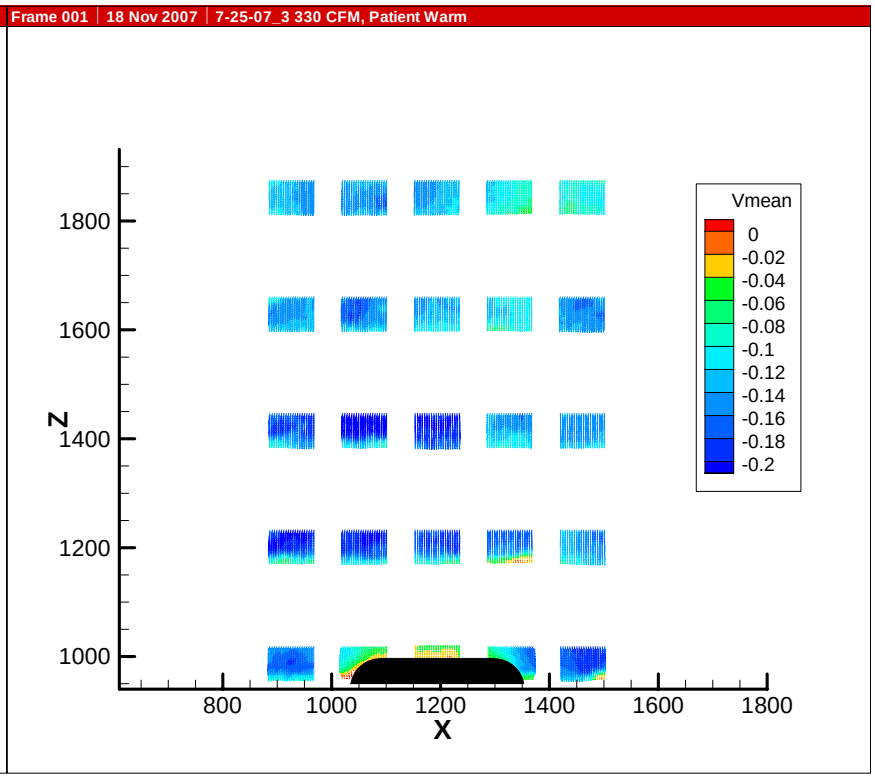

Figure A.12: Detail Velocity Vectors for 330 CFM, Patient Warm Experimental Run Performed on 7-25-2007

420 CFM – Patient Cold

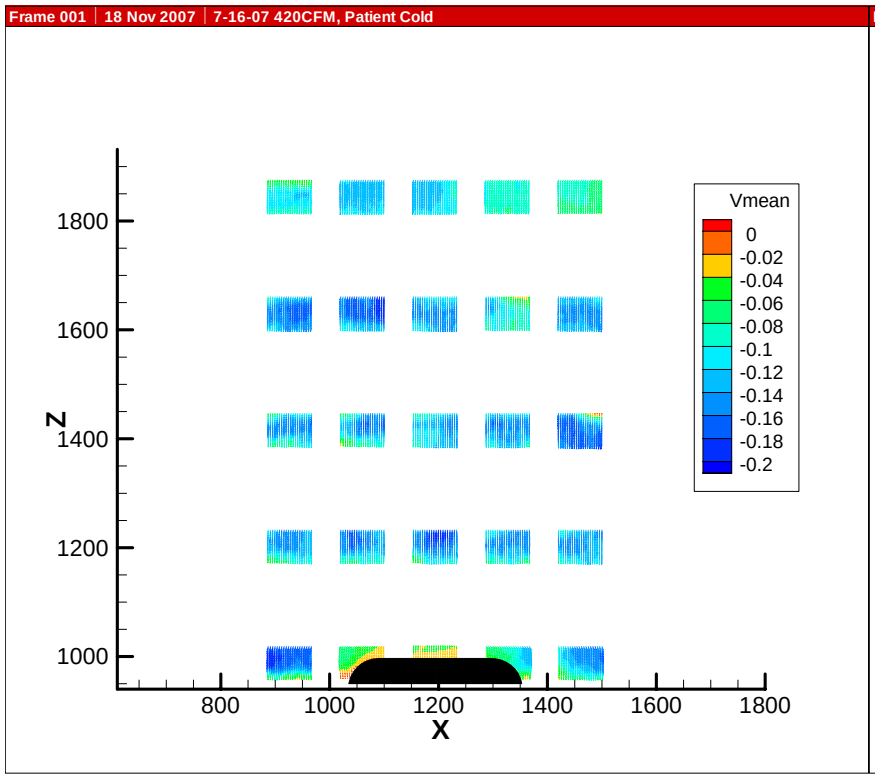

Figure A.13: Detail Velocity Vectors for 420 CFM, Patient Cold Experimental Run Performed on 7-16-2007

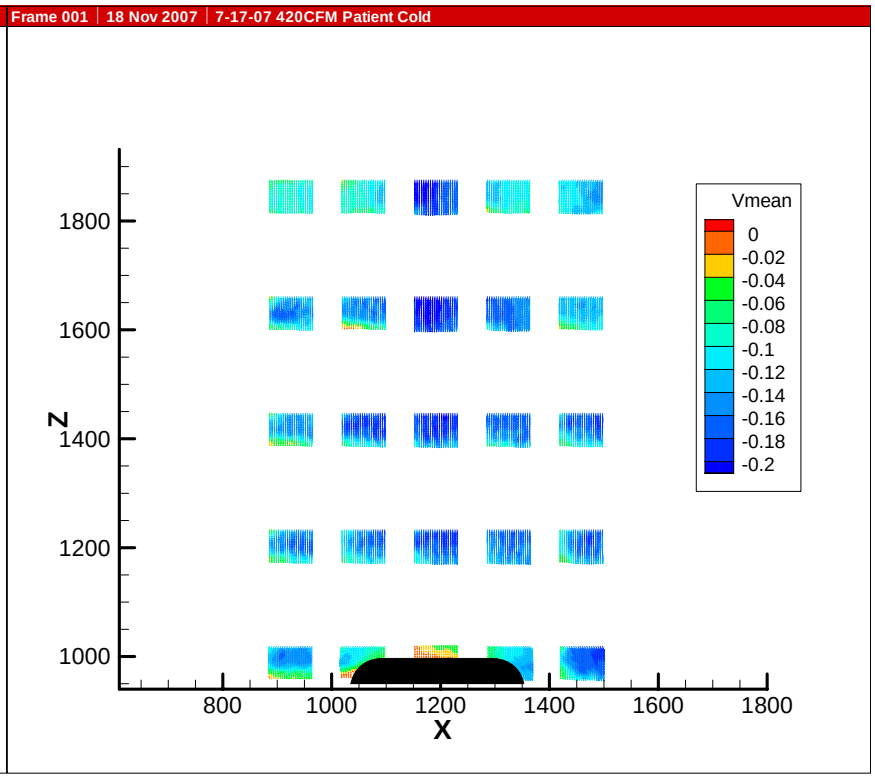

Figure A.14: Detail Velocity Vectors for 420 CFM, Patient Cold Experimental Run Performed on 7-17-2007

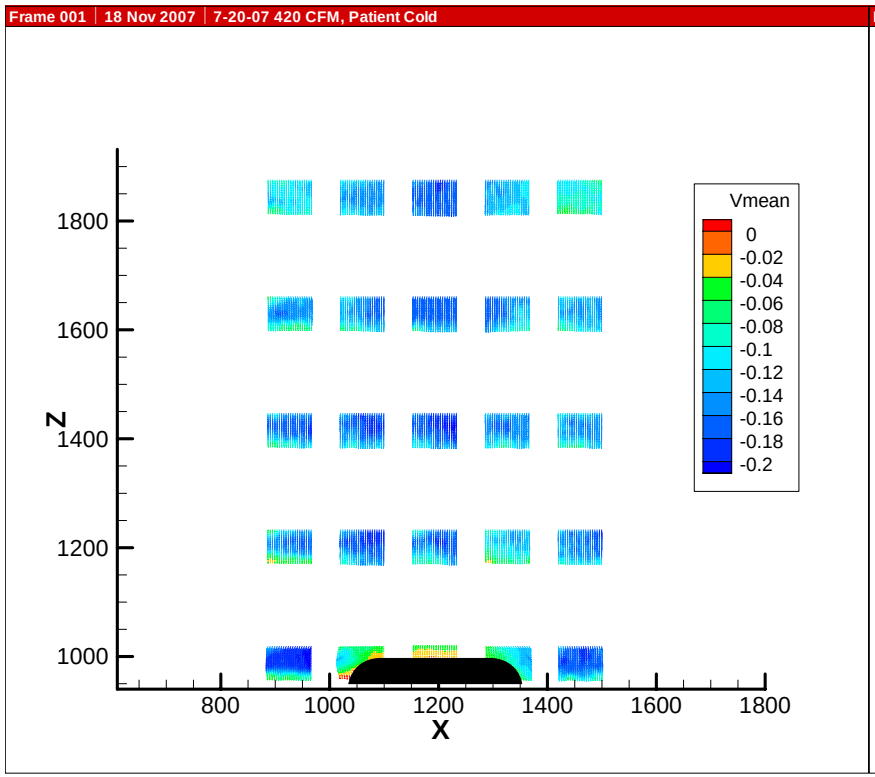

Figure A.15: Detail Velocity Vectors for 420 CFM, Patient Cold Experimental Run Performed on 7-20-2007

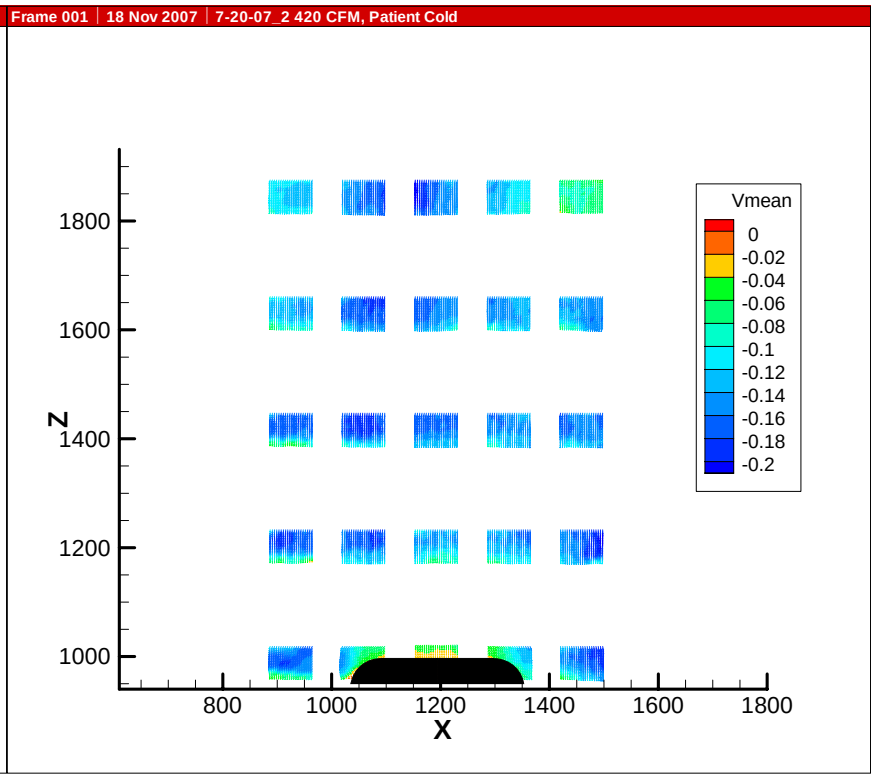

Figure A.16: Detail Velocity Vectors for 420 CFM, Patient Cold Experimental Run Performed on 7-20-2007

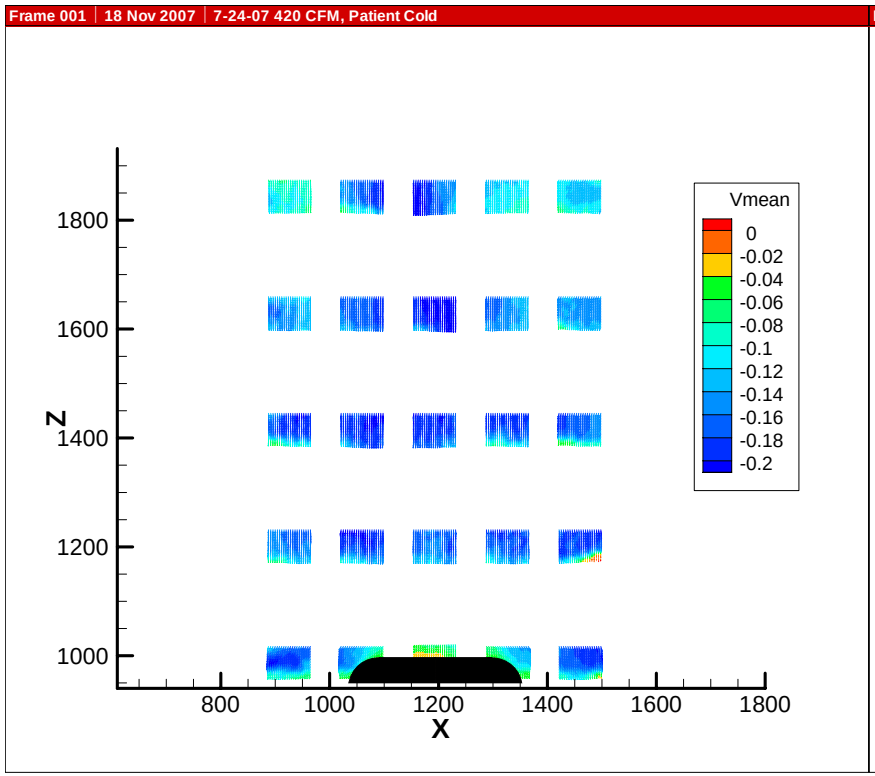

Figure A.17: Detail Velocity Vectors for 420 CFM, Patient Cold Experimental Run Performed on 7-24-2007

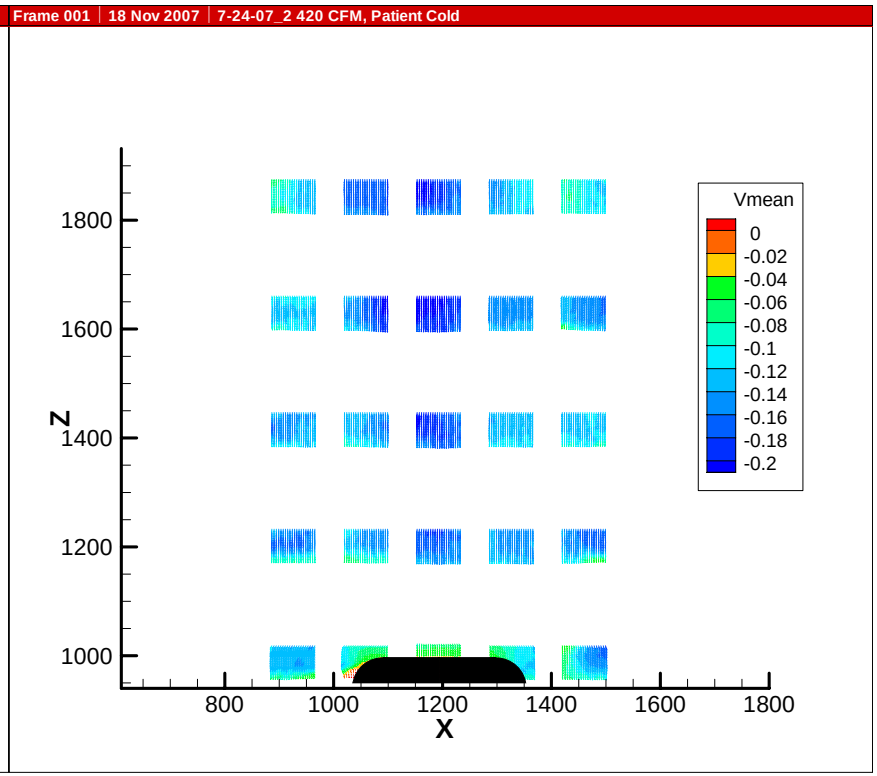

Figure A.18: Detail Velocity Vectors for 420 CFM, Patient Cold Experimental Run Performed on 7-24-2007

420 CFM – Patient Warm

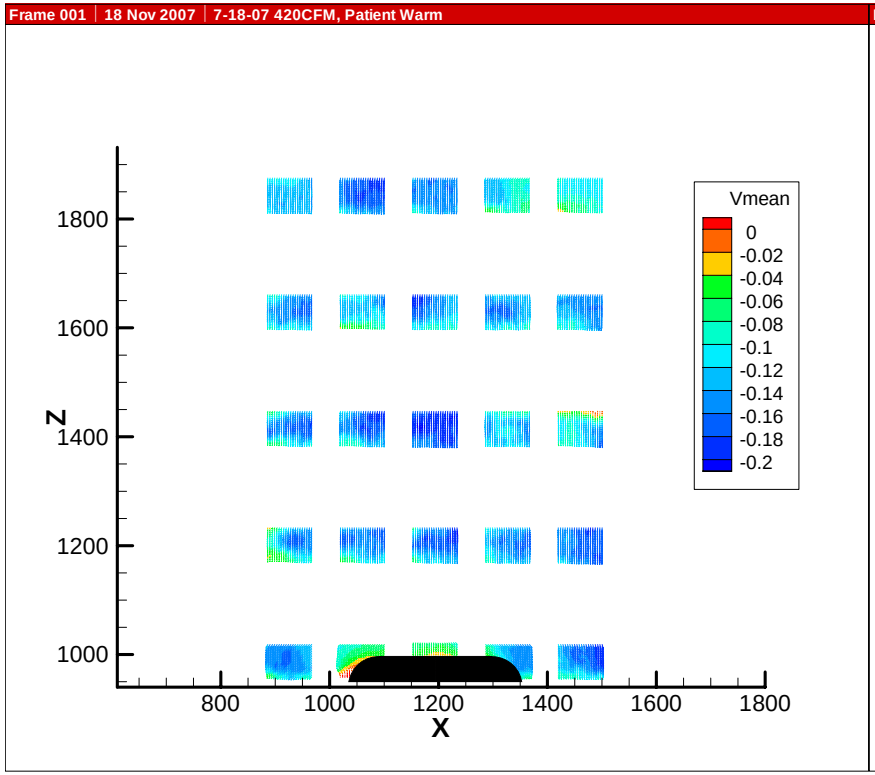

Figure A.19: Detail Velocity Vectors for 420 CFM, Patient Warm Experimental Run Performed on 7-18-2007

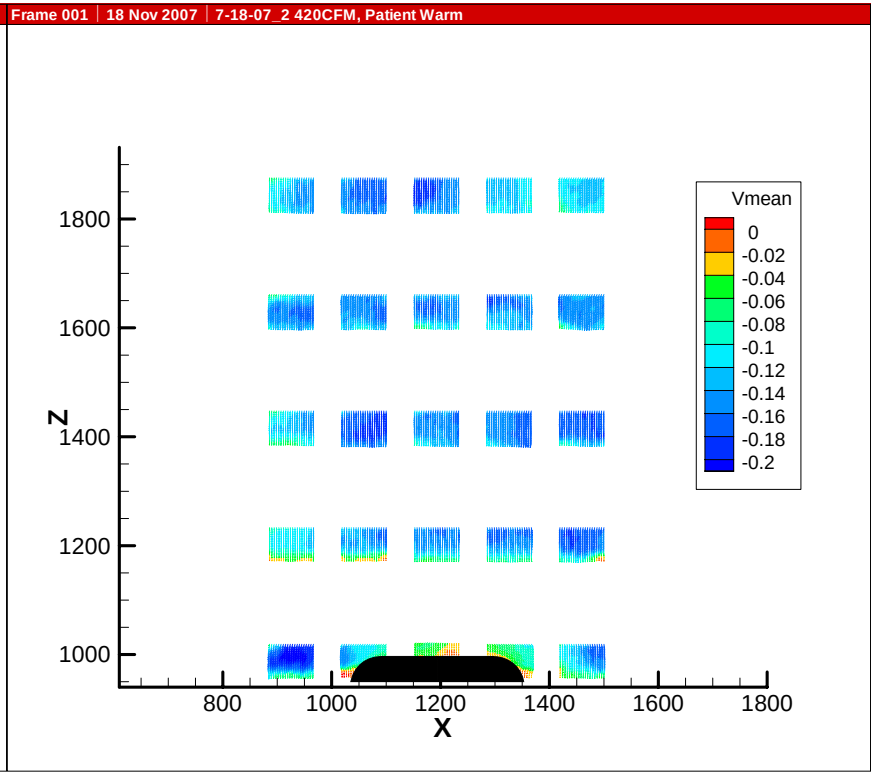

Figure A.20: Detail Velocity Vectors for 420 CFM, Patient Warm Experimental Run Performed on 7-18-2007

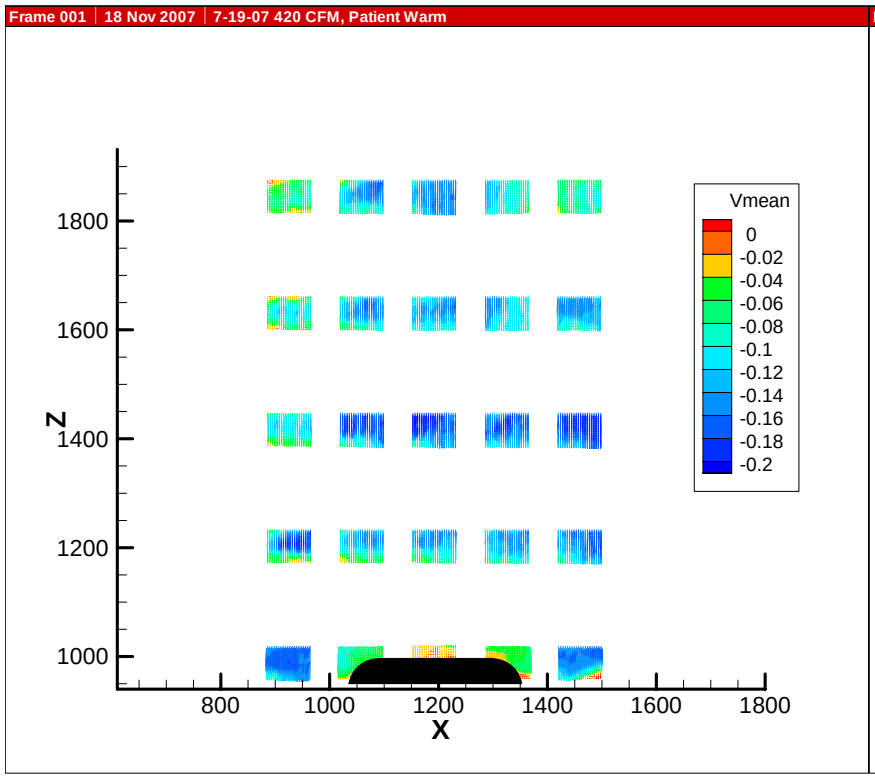

Figure A.21: Detail Velocity Vectors for 420 CFM, Patient Warm Experimental Run Performed on 7-19-2007

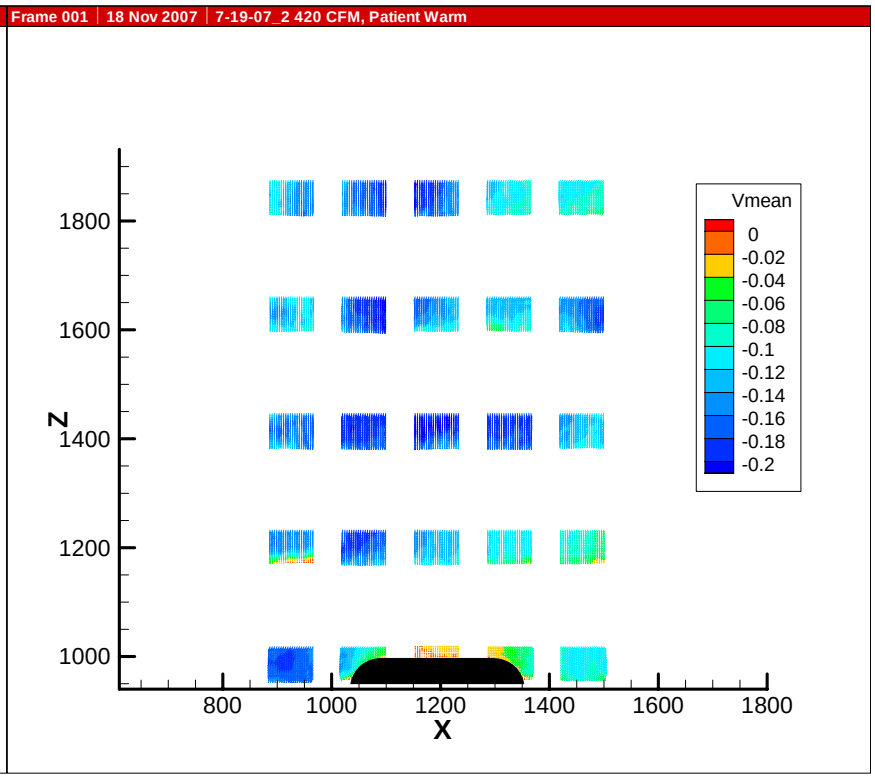

Figure A.22: Detail Velocity Vectors for 420 CFM, Patient Warm Experimental Run Performed on 7-19-2007

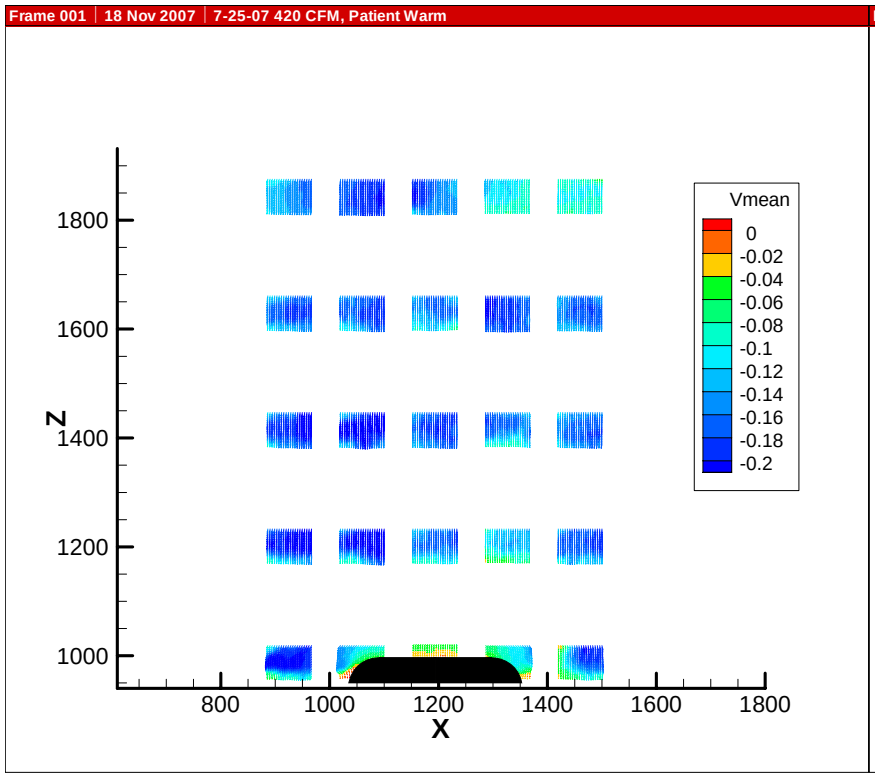

Figure A.23: Detail Velocity Vectors for 420 CFM, Patient Warm Experimental Run Performed on 7-25-2007

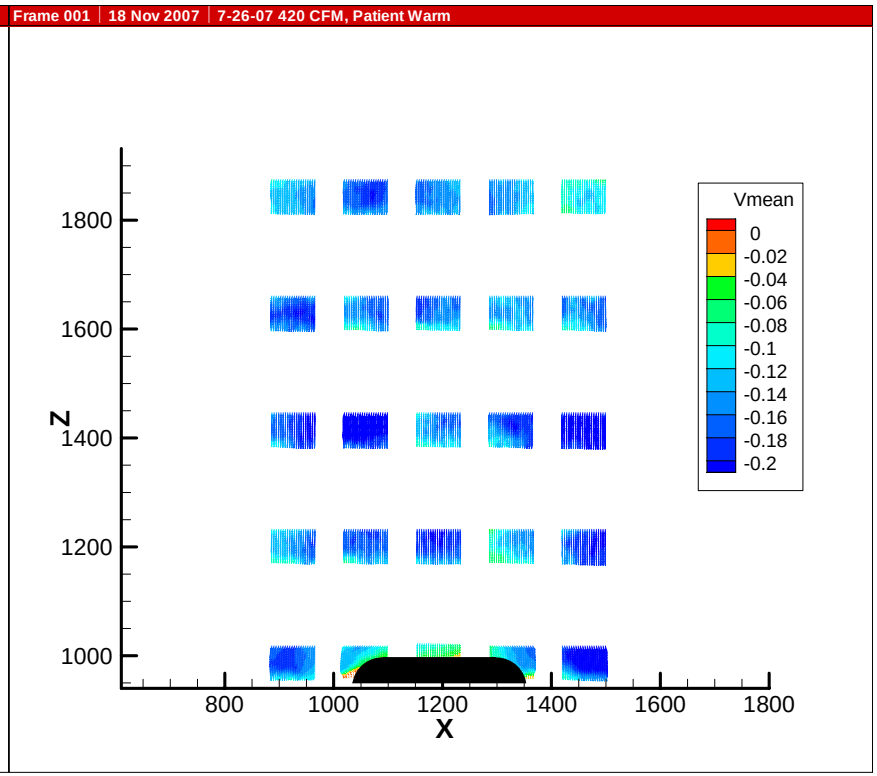

Figure A.24: Detail Velocity Vectors for 420 CFM, Patient Warm Experimental Run Performed on 7-26-2007

APPENDIX B – AVERAGE PLOTS FOR THE FOUR CASES

330 CFM – Patient Cold Average Plot

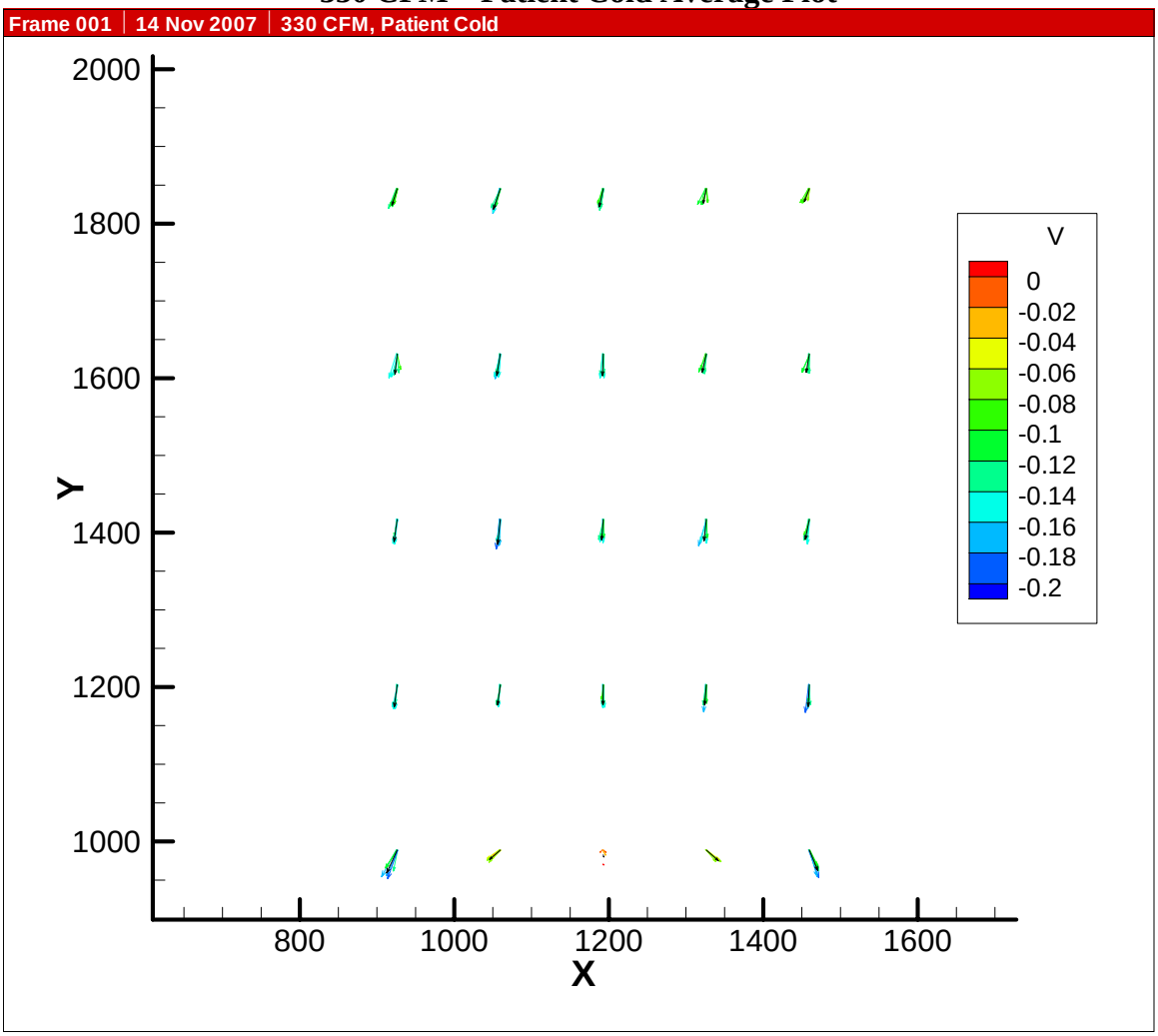

Figure B.1: Averaged Velocity Vectors for 330 CFM, Patient Cold Case
The data points from each individual run are color-coded as shown
The average vector from all the runs is black

330 CFM – Patient Warm Average Plot

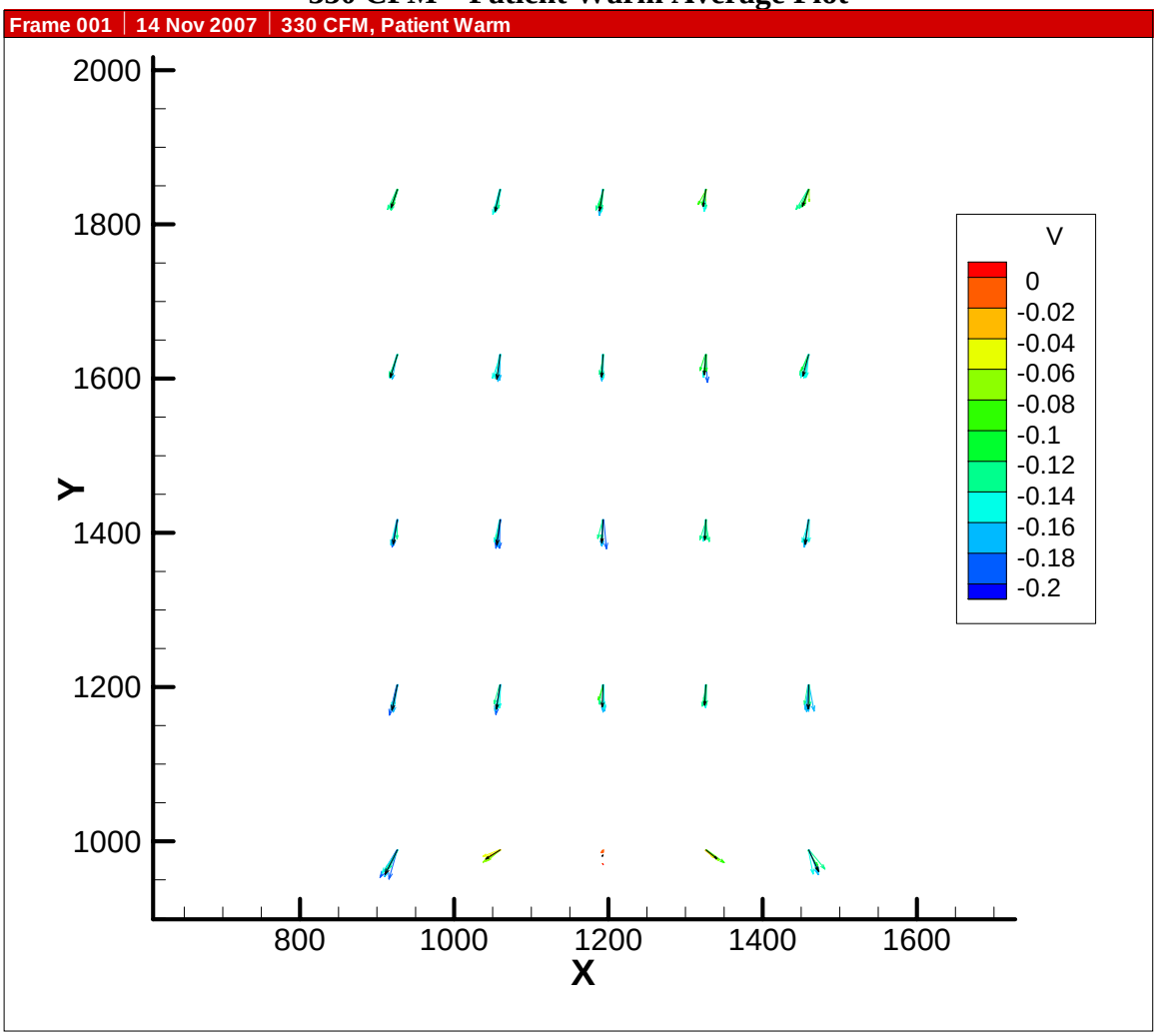

Figure B.2: Averaged Velocity Vectors for 330 CFM, Patient Warm Case
The data points from each individual run are color-coded as shown
The average vector from all the runs is black

420 CFM – Patient Cold Average Plot

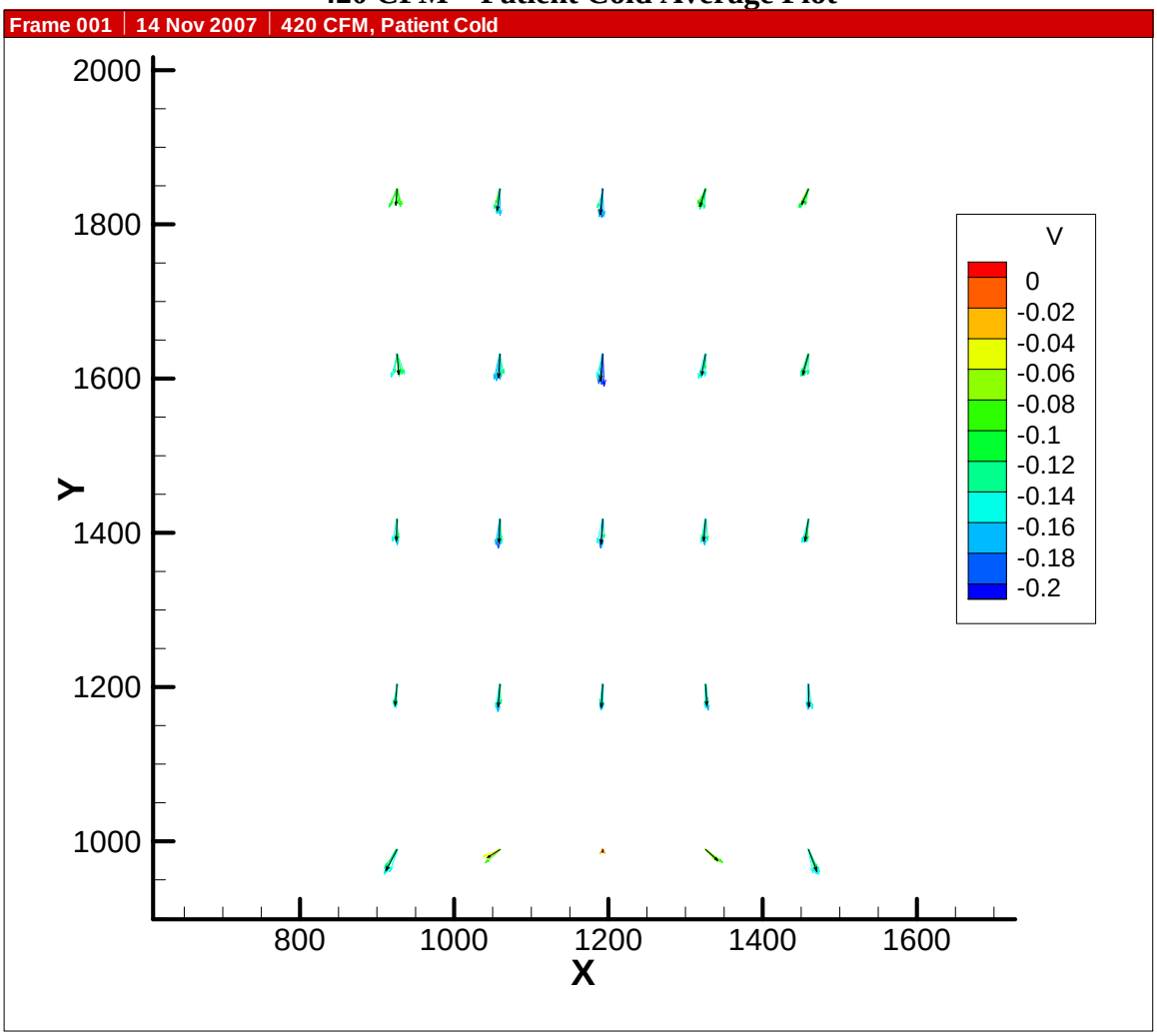

Figure B.3: Averaged Velocity Vectors for 420 CFM, Patient Cold Case
The data points from each individual run are color-coded as shown
The average vector from all the runs is black

420 CFM – Patient Warm Average Plot

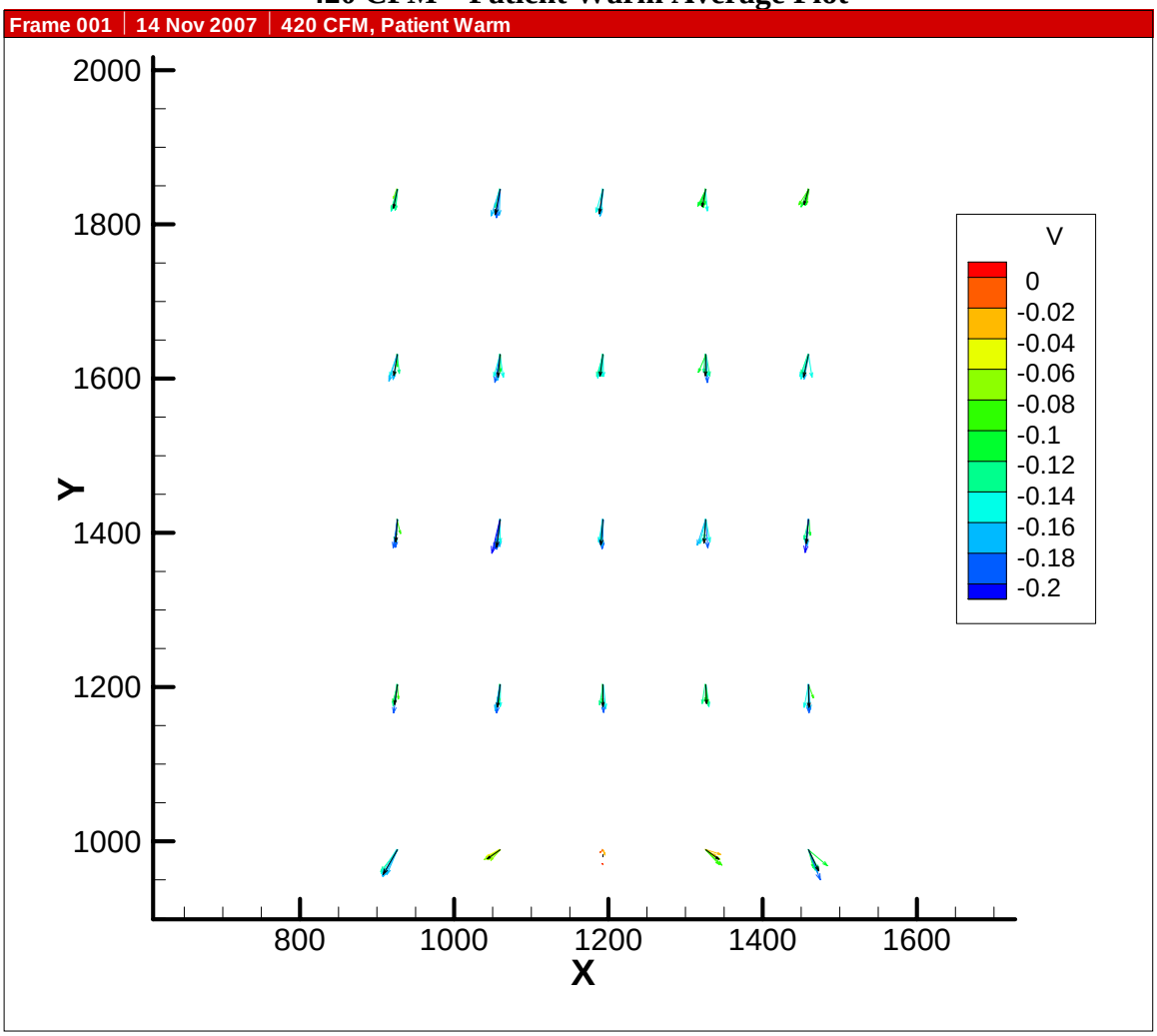

Figure B.4: Averaged Velocity Vectors for 420 CFM, Patient Warm Case
The data points from each individual run are color-coded as shown
The average vector from all the runs is black

APPENDIX C – CFD RESULTS

330 CFM – Patient Cold

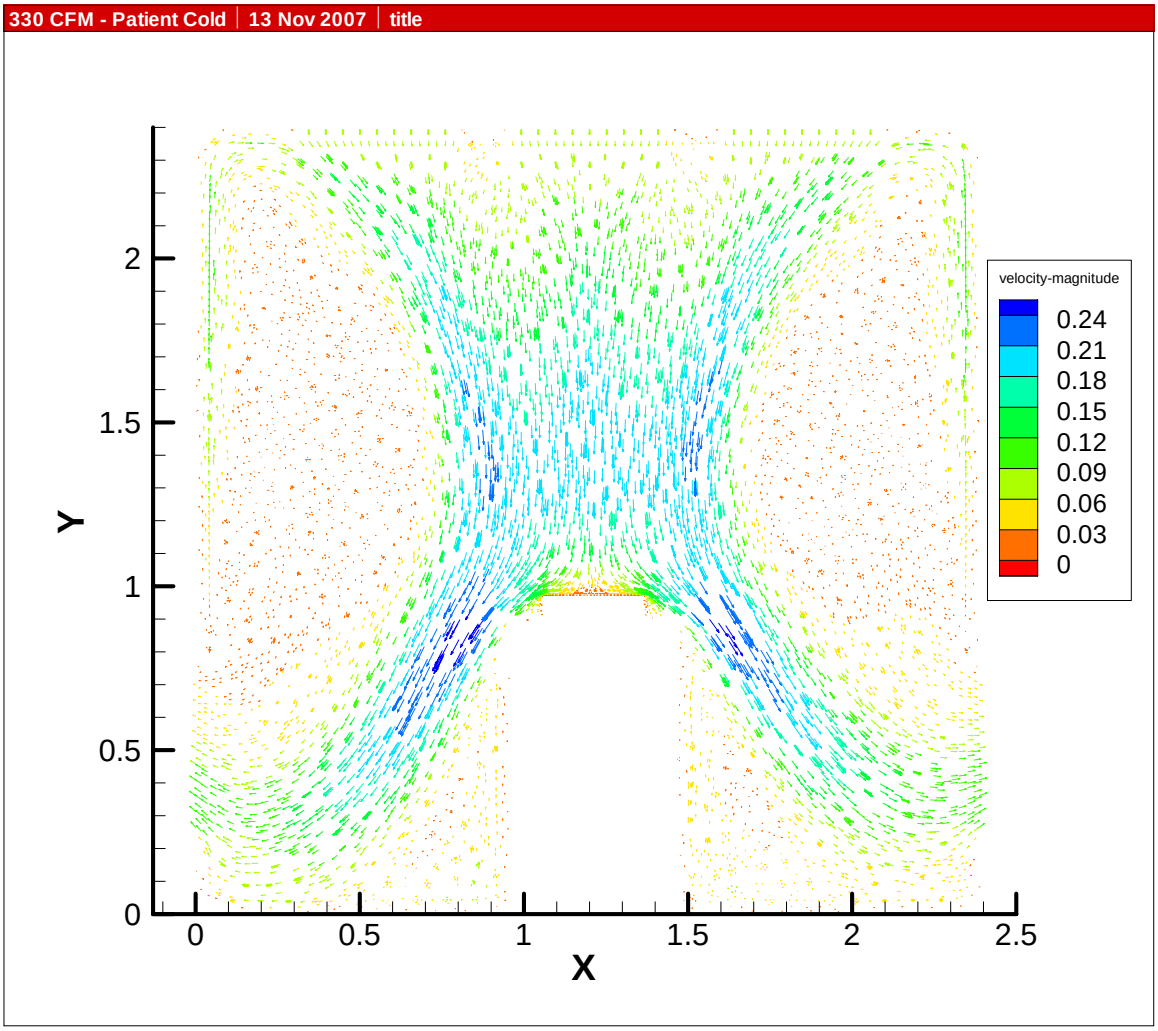

Figure C.1: 330 CFM, Patient Cold CFD Results

330 CFM – Patient Warm

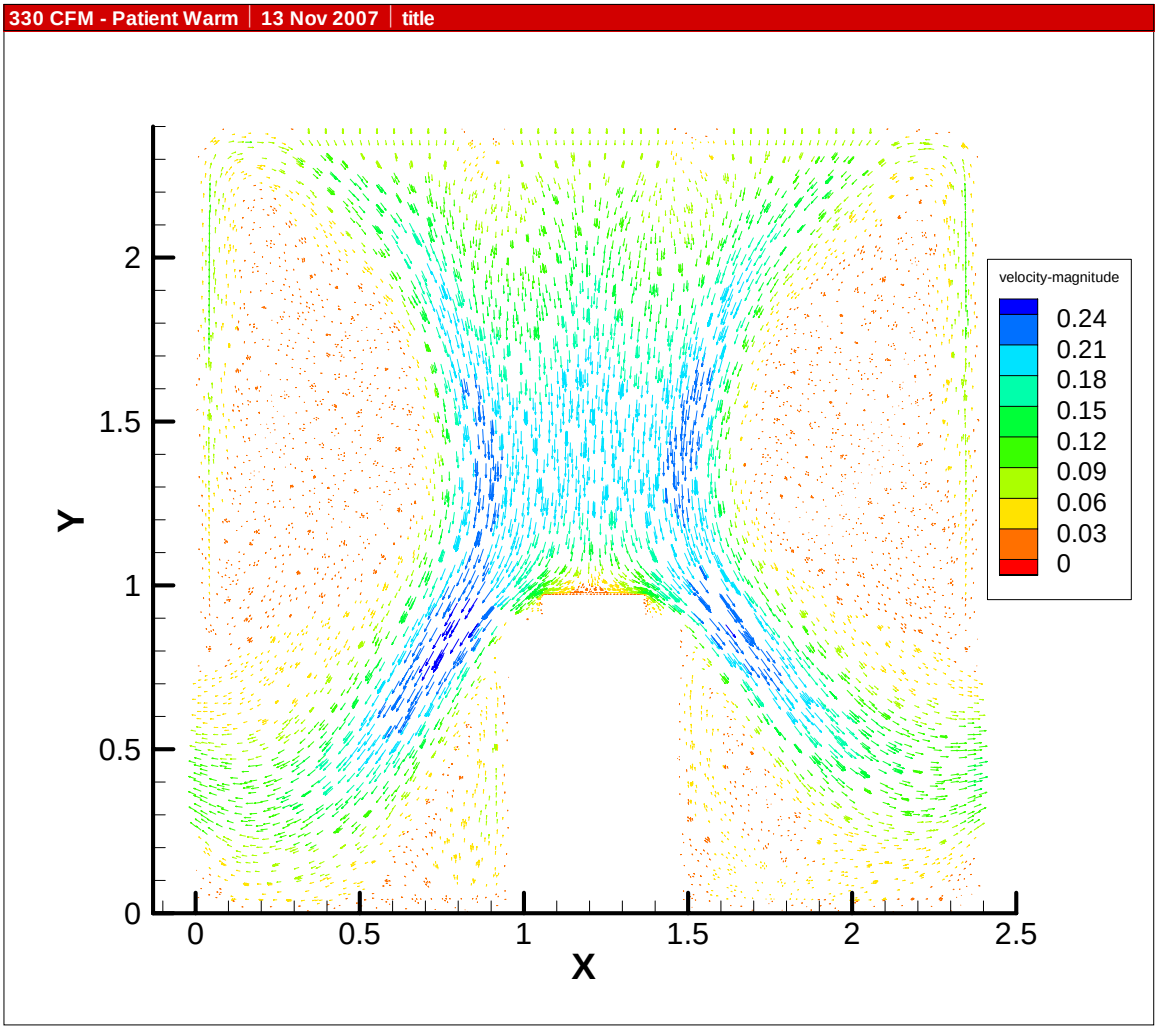

Figure C.2: 330 CFM, Patient Warm CFD Results

420 CFM – Patient Cold

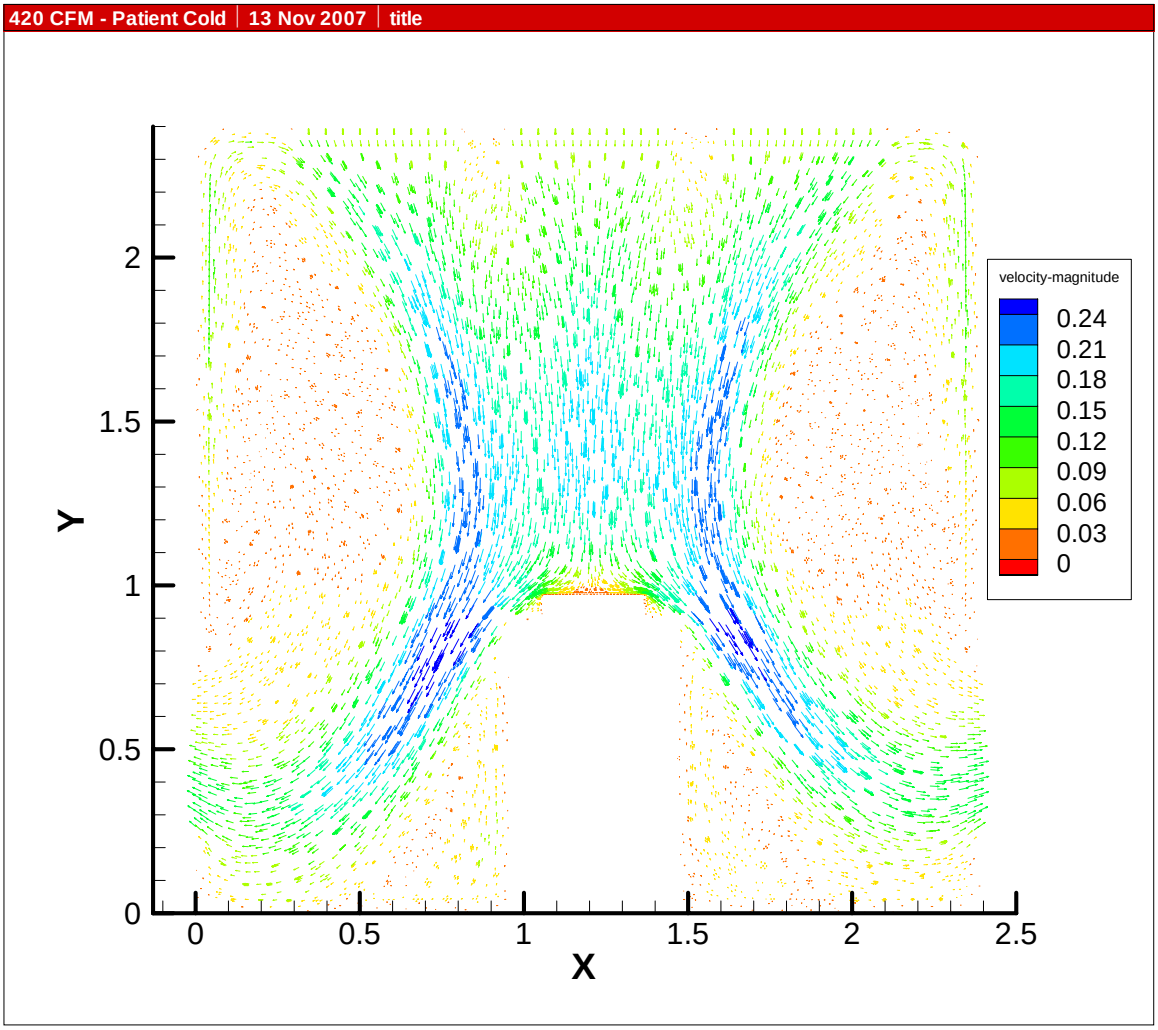

Figure C.3: 420 CFM, Patient Cold CFD Results

420 CFM – Patient Warm

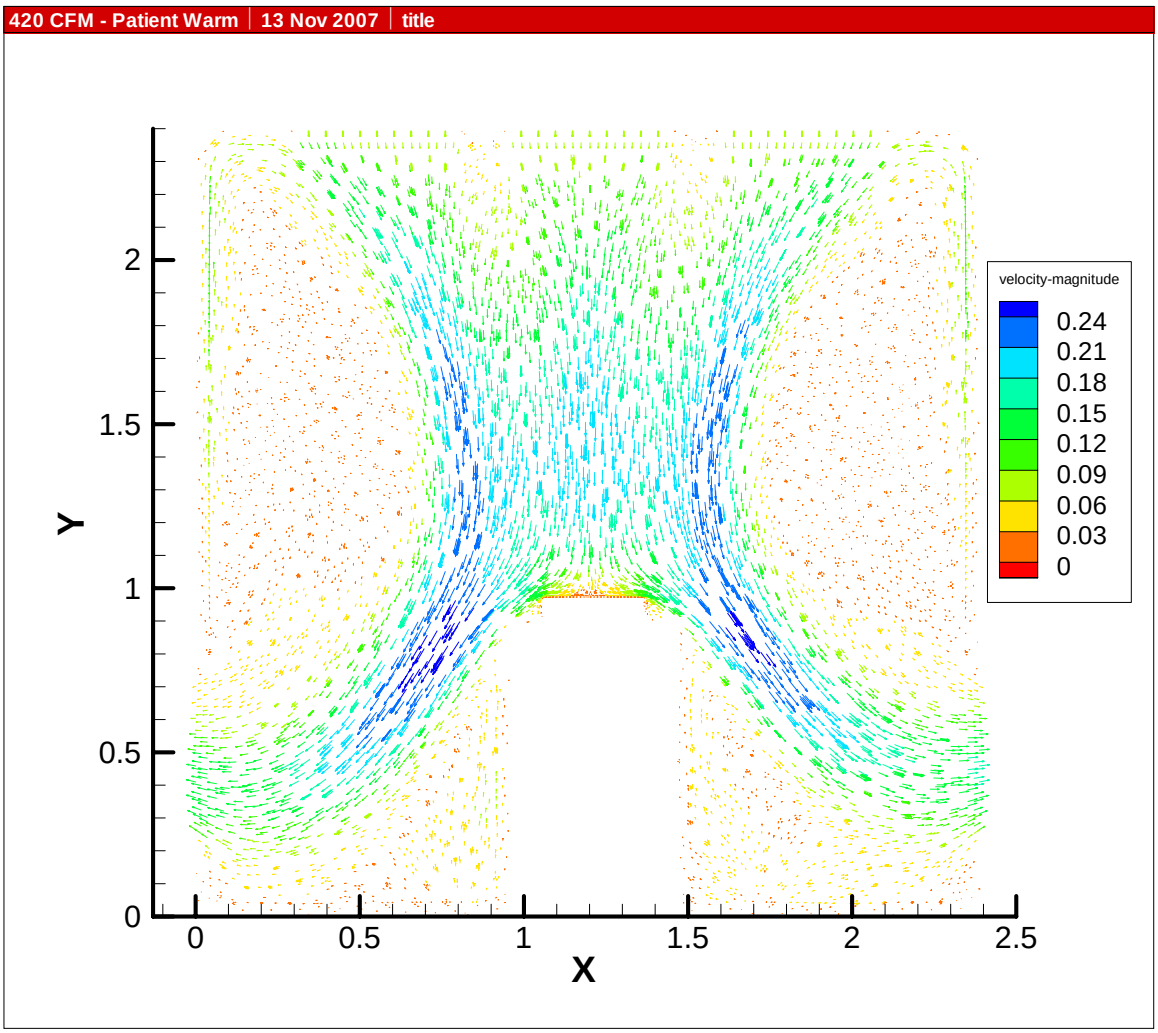

Figure C.4: 420 CFM, Patient Warm CFD Results

APPENDIX D – COMPLETE PIV PROCEDURE

1. Open supply air to operating room
    a. Tweak pressure to VAV box in order to adjust the flow entering the operating room by adjusting the knob in the following figure.

    b. The volumetric flow rate (in CFM) entering the room can be calculated with the following equation. The dynamic pressure, q_D, used in the equation is read from a Dwyer 1" Manometer, shown below.

$$Q = 2117 \cdot \sqrt{q_D}$$

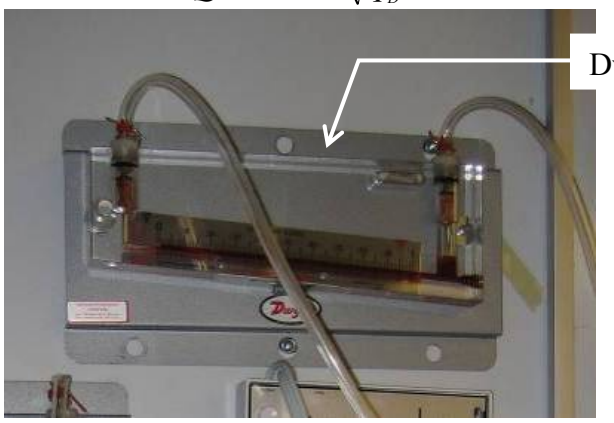

2. Turn on Agilent Data Acquisition/Switch Unit
3. Turn on power supply for Alnor Thermo-Anemometer
    a. Channels are assigned as shown in Section 2.1.
4. Push play button in Agilent Data Logger window to start monitoring
5. If a run with the patient heated is being done, turn on the Brookfield Heater Pump
    a. Monitor Channel 11 in Agilent Data Logger
    b. Typically takes about 1 hour to heat up to 85°F
6. Power on Camera Positioner Power Supply and Laser Positioner Power Supply

Camera Positioner Power Supply

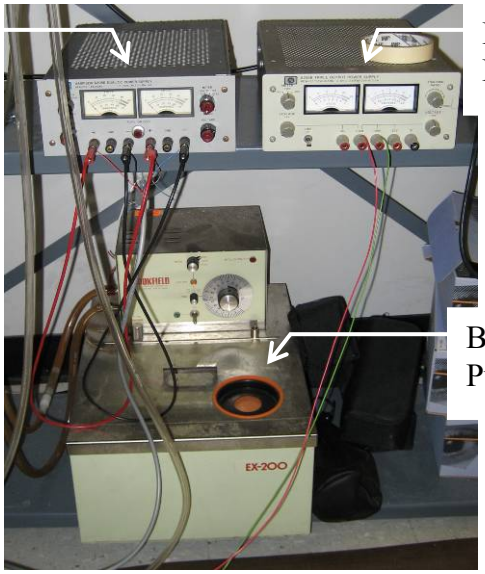

Laser Positioner Power Supply

Brookfield Heater Pump

7. Open proVISION-XS
8. Set-up proVISION for a run
    a. Click “Open PIV Camera Session”

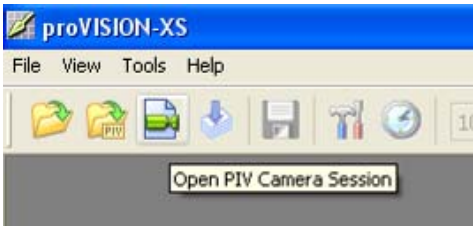

        1. Click Next >
    b. Create New Camera session as PIV Research

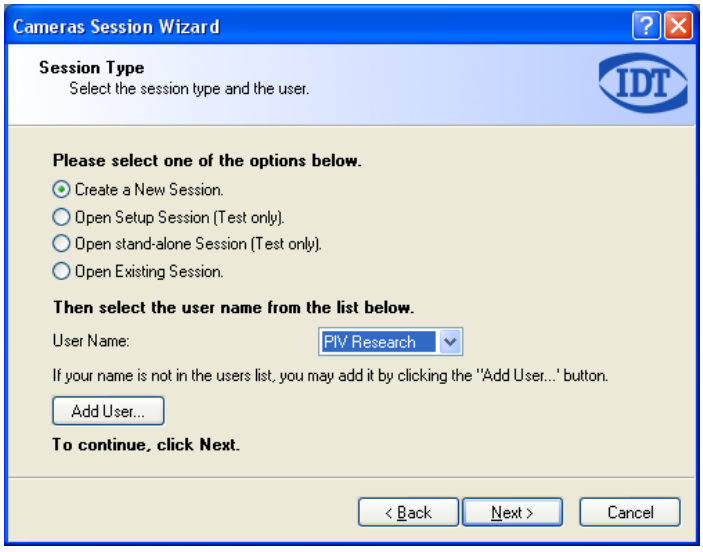

        1. Click Next >
    c. Enter the date for session name

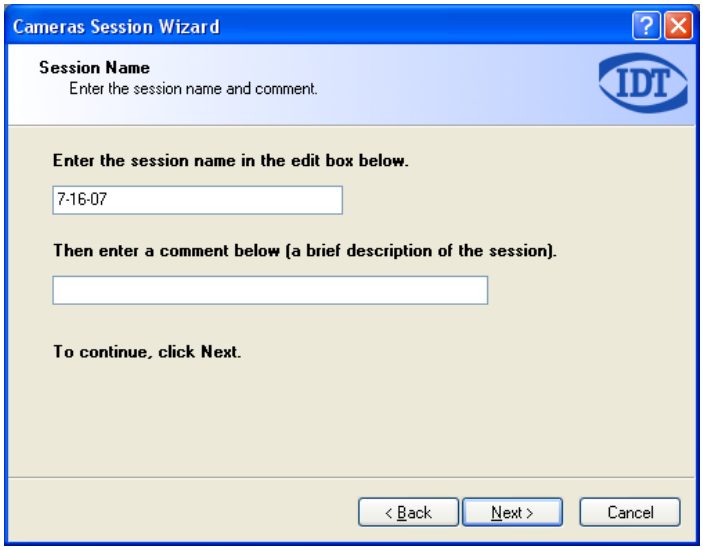

1. Click Next > Next > Next > Finish

d. In main screen, ensure camera pad and camera settings are displayed

e. Calibrate the camera
    1. Click on Calibration Settings

    2. If no changes have occurred since the last calibration, the last calibration image can be loaded by selecting the "Import calibration image" button from the calibration box and finding the calibration image from a previous run.

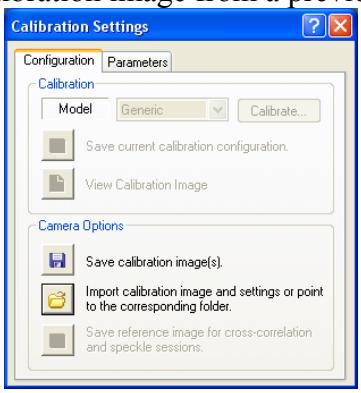

    3. If changes have been made, the camera needs to be calibrated.
    4. Place wood block with grid paper on top of simulated patient. Ensure that the grid is level and the plane of the grid is in the plane of the laser.
    5. Open Matlab
        1. Type "stepper" and hit enter

2. Check to make sure the camera is in the physical “Home” position before moving it

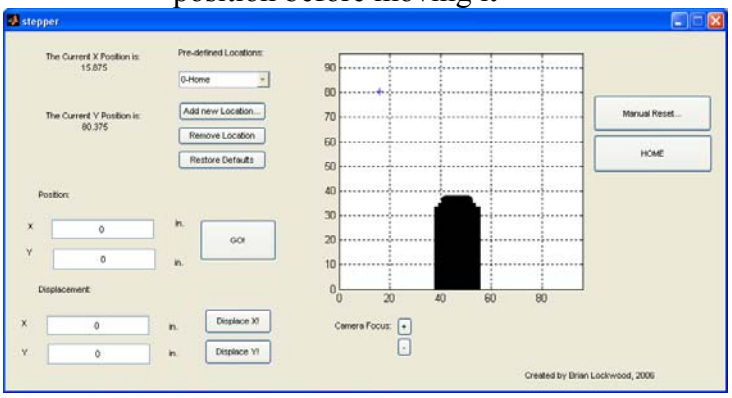

3. Move to predefined position 8-Mp-Center

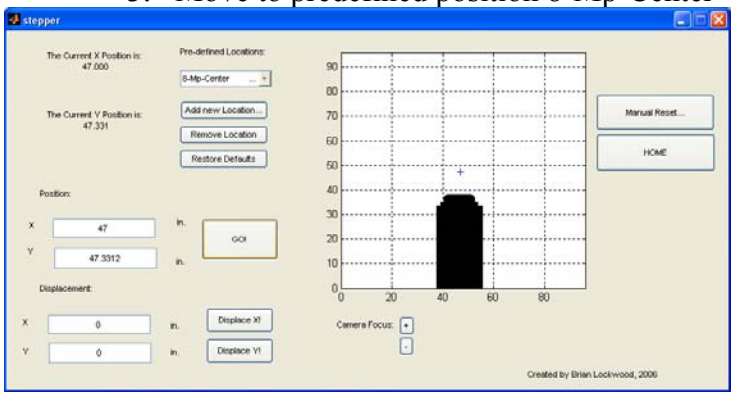

6. Click “Play” in the proVISION camera controls box

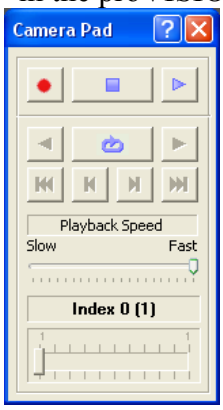

7. Change Brightness setting on camera until grid of grid paper is visible (settings shown below work well)

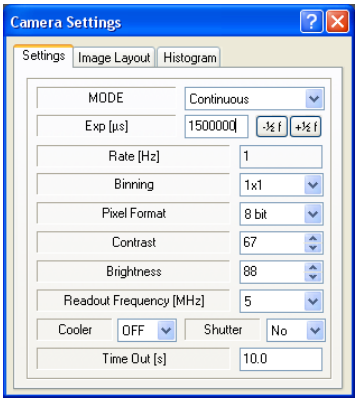

8. Adjust Camera Focus with outermost camera wheel
9. Click on "Save Calibration Image" in Calibration Settings Window
    1. Click Next
    2. Enter date for calibration family name, click Next > Next > Finish

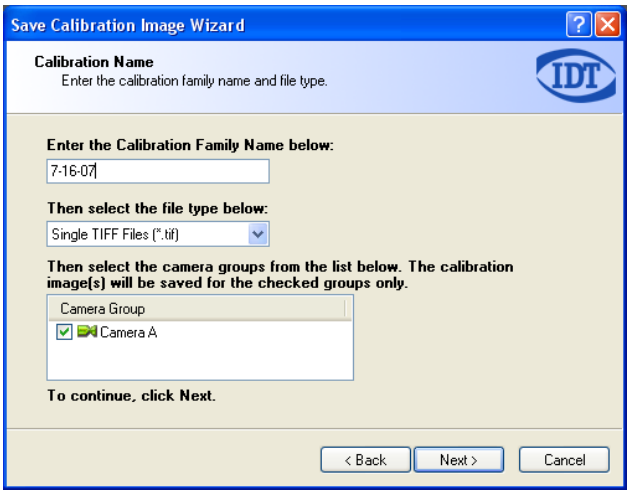

10. Click "Calibrate"

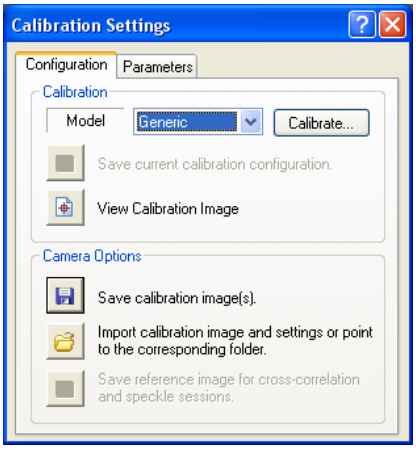

11. Make Grid size 50.8 50.8, Grid Nodes 9 x 9

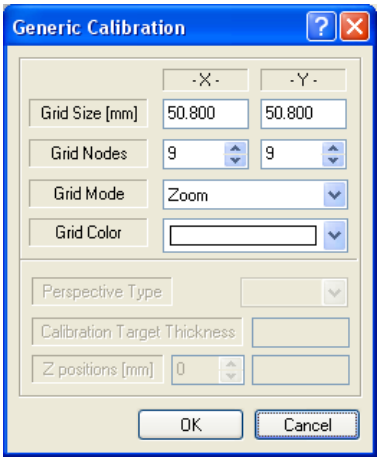

12. Line up grid on screen with the grid of the grid paper

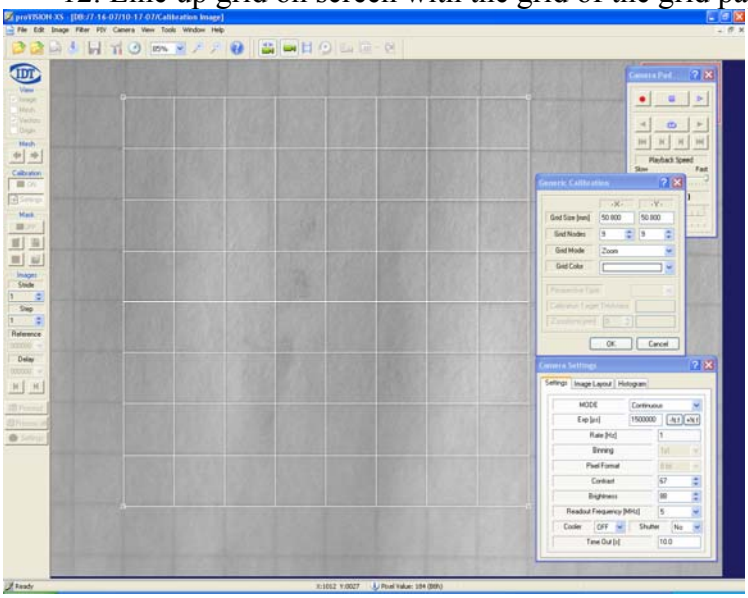

13. Click OK in Generic Calibration Window
14. Click OK again to finish Calibration
15. Close Calibration Settings Window
16. Click on PIV Settings

17. Click on Mesh Tab
18. Input the Mesh settings shown below

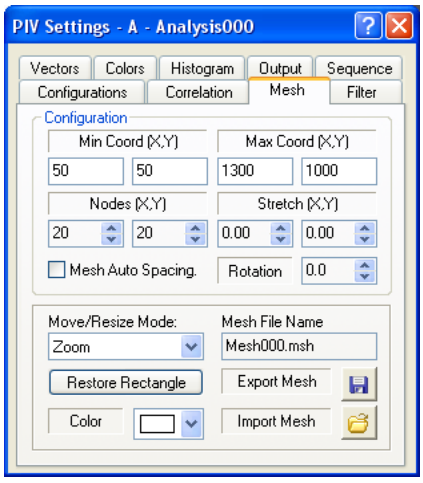

f. Remove check by mesh

9. Power on laser (turn key)
   a. Press START button
   b. Start on internal (INT) control for both lasers
   c. Press LASER1 and LASER2 buttons simultaneously to start up laser
10. Turn on fog to 15 psi
11. Line up laser with field of camera using vertical laser adjustment switch (located near computer monitor)
12. In the proVISION window, click Clock to adjust timing configuration

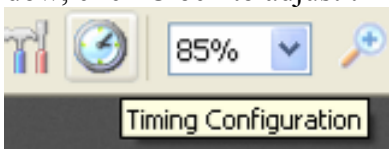

   a. On/Off
   b. Click Emission
   c. 1000 pulse separation (controls time between laser pulses)
   d. .5 Hz camera freq. (freq of snapshots)

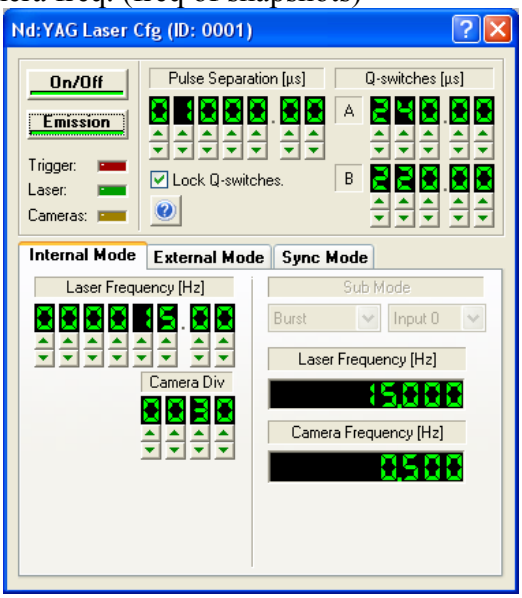

13. Turn laser to computer control (EXT) for both lasers

a. Ensure level is set to high
b. Press LASER1 and LASER2 buttons to start lasers again

Steps for a typical run

1. Using Matlab stepper program, move camera to pre-defined location 1
2. Set laser manually to cut across the face of the camera
3. Press play
4. Manually focus camera until a fog particles are visible in the picture
5. Set Camera settings Double Exposure

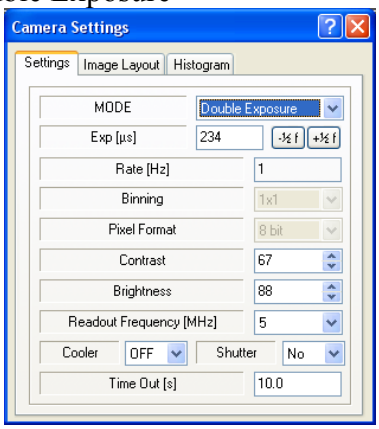

6. Click on "Record" and then "Play"

7. If this is the first capture of a run, the acquisition name will be "Acquis001". It is best to name the acquisition the same as the position number (eg Acquis005 for position 5)
   a. Click Save
   b. Wait for sequence to complete
8. It's a good idea to do a quick analysis of each sequence before moving the camera to ensure that a good reading was taken
9. Click PIV Settings

a. Under the Correlation Tab
    i. Set the Mode to Adaptive
    ii. Turn off Auto Range and set to
        1. -16 to 16 in u-direction
        2. -16 to 16 in v-direction

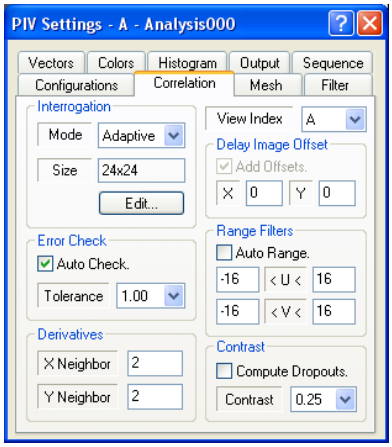

b. Under Vectors Tab, set Interp cut off to >40

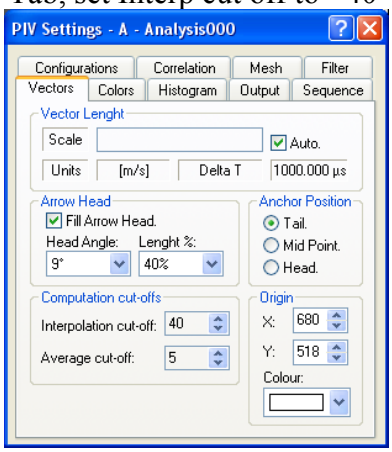

c. Under the Output Tab
    i. Set output to ASCII
    ii. Click on Launch Tecplot field

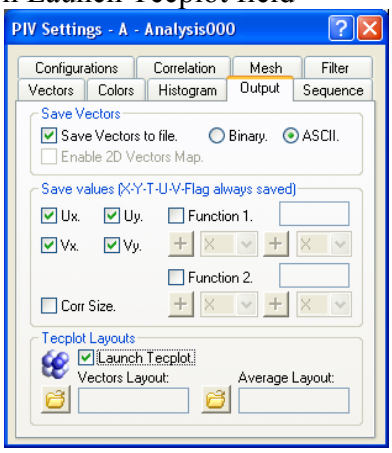

d. Under the Sequence Tab
    i. Set number of images to 30

ii. Image stride 2
iii. Click Process

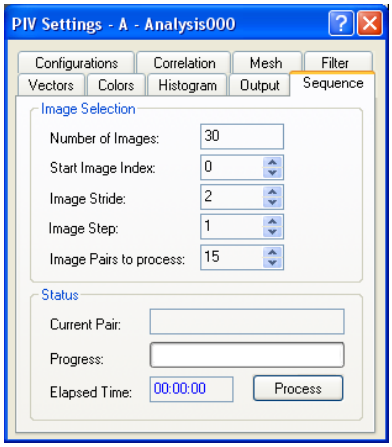

10. To step thru non averaged plots go to Tools>Animate Zones
11. Continue moving the camera and taking measurements until all 25 positions have been completed.

To analyze the sequence batch:

1. If you analyzed each sequence as you took it, skip to Step 7
2. Otherwise, click "Open PIV Images" in proVISION window

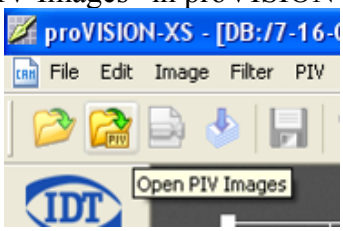

3. Select date (or folder name) and acquisition run you want to analyze
   a. Click date>Acquis001>ImgA.tif

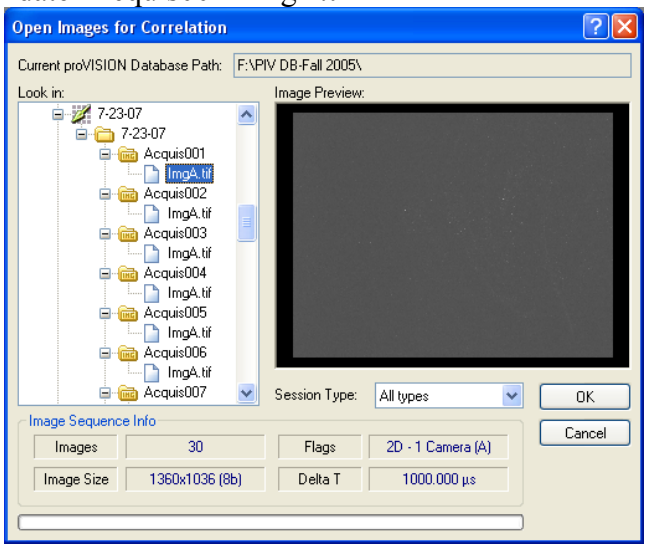

4. Click on Settings
   a. Use the same Settings as shown above
5. Hit Process

6. Go to the Start menu and MyComputer/F:PIVDB-Fall 2005
    a. Open your folder
    b. Open the date folder
        i. Acquis001>Analysis000
            1. Copy config.prv and mesh000.msh
        ii. Go to Acquis002>Analysis000
            1. Paste
        iii. Go to Acquis003>Anaylsis000
            1. Paste
        iv. And so on… This ensures a consistent mesh between all captures
7. Go back to the proVISION window and select "Open PIV batch"

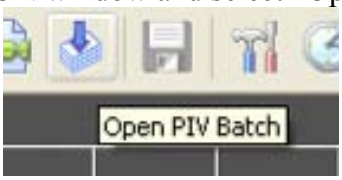

    a. Click "Yes"

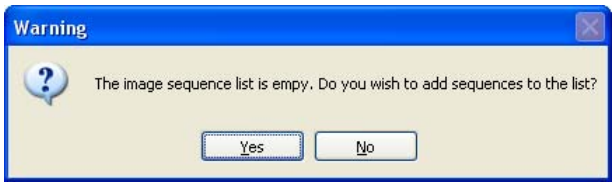

    b. Click Next
    c. Click on the radio button next to "Add multiple image sequences…."
    d. Click Next

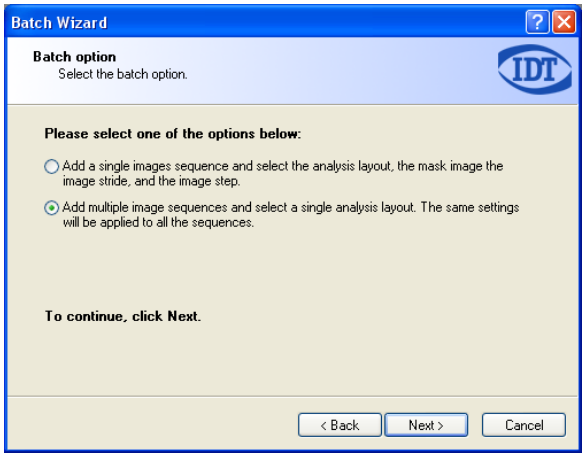

    e. Find your date

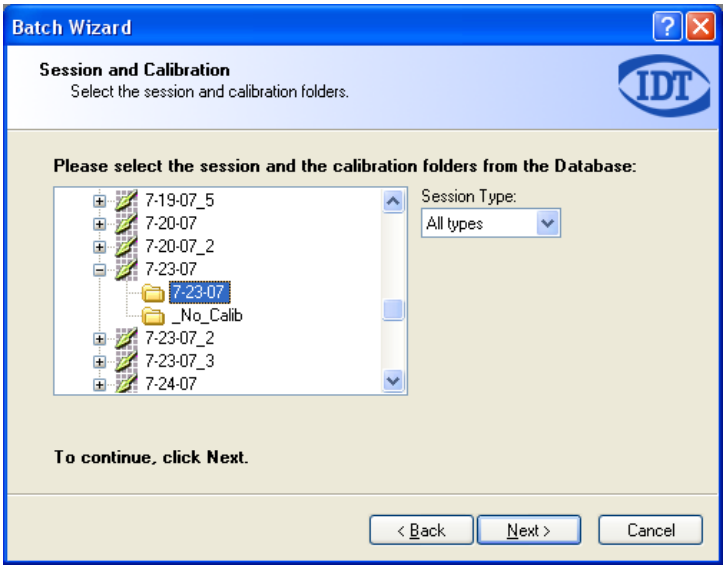

f. Click "Select All", then Next
g. Click on Analysis001 from Acquis001 (this will establish the analysis settings to be used)
h. Click on Analysis Info and ensure that the settings are correct
i. Click Next>Finish
j. Click "Process!"

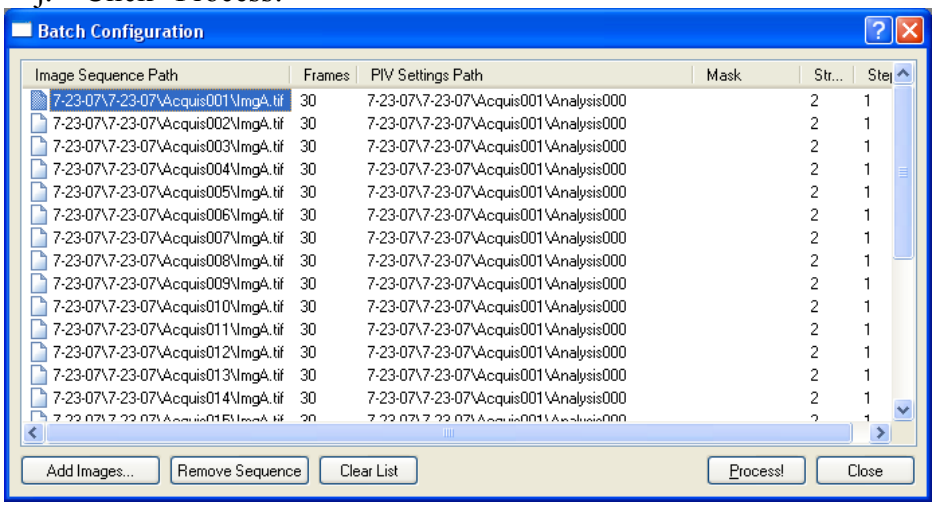

8. Find the data from the data just analyzed
    a. Go to F:/PIVDB…/your date/your date/Acquis001/Analysis000
        i. Copy ImgA-Average (the AutoCAD plot)

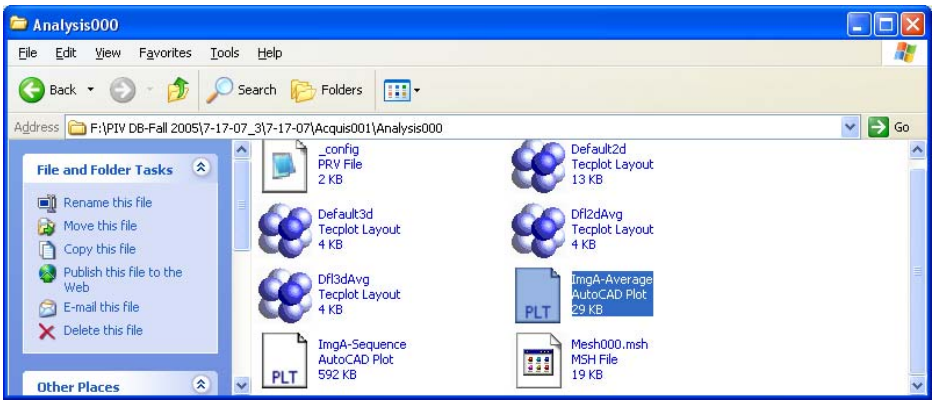

b. Go to C:\Documents and Setting/Owner/Desktop/25 spot Traverse
    i. Paste file into folder corresponding to the position
        1. Positions 1-5 are in “Patient” folder
        2. Positions 6-10 are in “Mid-Patient” folder
        3. Positions 11-15 are in “Middle” folder
        4. Positions 16-20 are in “Mid-Top” Folder
        5. Positions 21-25 are in the “Top” Folder

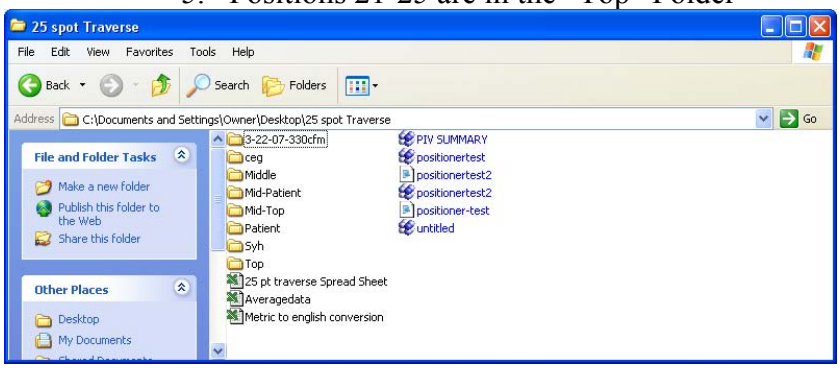

9. After all 25 are done, open Excel file titled “25 pt traverse Spread Sheet
    a. Enable macros
    b. Click Import when prompted (this updates the data in the spreadsheet for all 25 zones)
    c. Go to Tools>Macro>Visual Basic editor
        i. Click on “Forms” folder
            1. Double-click UserForm1
            2. Click “Play”

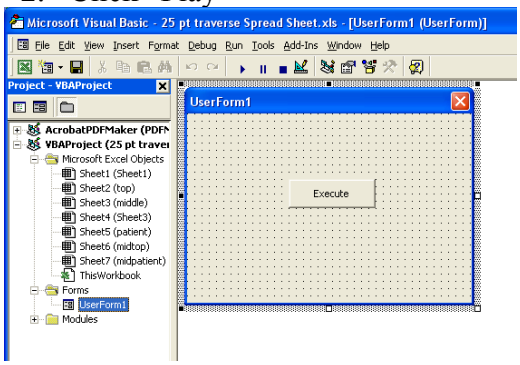

    d. Go to Sheet 3
    e. Click in the upper right hand corner of the spreadsheet to select all

f. Copy
g. Open Notepad
h. Paste data into notepad
i. Save as date.dat (make sure Save as Type is All Files)

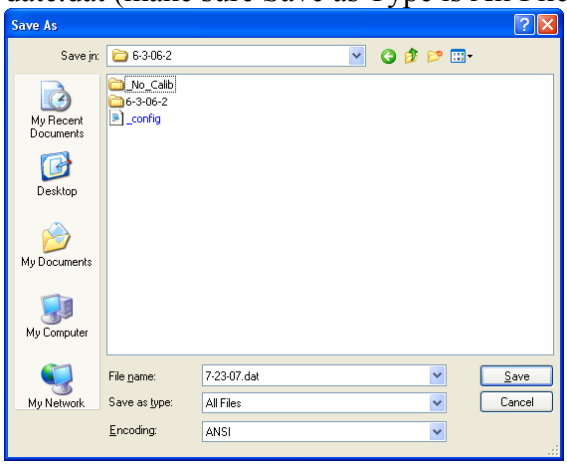

j. Exit out of Excel, do not save

10. Open Tecplot template file "patient_layout"
    a. Click File>Load Data File(s)
    b. Click on radio button next to "Replace data set and retain plot style

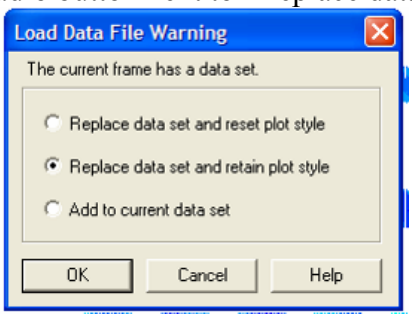

    c. Find the .dat that was just generated.
    d. The data collected will be displayed in Tecplot

APPENDIX E – STEPPER MOTOR CONTROLLER

```
function stepx(dis)                          Defines function stepx and variable dis
dio=digitalio('parallel',1);
hline=addline(dio, 0:7, 'out');
if dis==0                                    If distance to travel is zero, end program
   return
else                                         If distance to travel is less than zero, rotate
  if dis<0                                   step motor counterclockwise
     dir=0;
  else
     dir=1;                                  If distance to travel is greater than zero,
  end                                        rotate step motor clockwise
  distance=abs(dis);
  putvalue(dio,0)
    for i=0:1:ceil((distance/9.3750e-004))   Defines the distance traveled with each step
       putvalue(dio,8*dir);                  to determine the number of steps required

     putvalue(dio,8*dir+1);
    end
   putvalue(dio,16)
end

function stepy(dis)                          Defines the same routine for the y-direction
dio=digitalio('parallel',1);
hline=addline(dio, 0:7, 'out');

if dis==0
   return
else
  if dis<0
     dir=1;
  else
     dir=0;
  end
  distance=abs(dis);
  putvalue(dio,0);
    for i=0:1:ceil((distance/8.2500e-004))
       putvalue(dio,8*dir);
      for j=0:1:300000
      end
      putvalue(dio,8*dir+2);
    end
  putvalue(dio,16)
end
```

APPENDIX F – HEAT FLUX CALCULATIONS

T_av=16 [C]
P=101.325 [kPa]
Cp_air=Cp(air,T=T_av)
rho_air=density(air,T=T_av,P=P)
Q_low=.1557 [m^3/sec] "330 CFM"
Q_high=.1982 [m^3/sec] "420 CFM"
m_dot_low=Q_low*rho_air
m_dot_high=Q_high*rho_air
ductarea=(20.5/39.37)^2*9 [m^2]

wallarea=15.75 [m^2]
heat_flux_low=Q_dot_cold_low/wallarea
heat_flux_high=Q_dot_cold_high/wallarea

"Temperature Data"
T_in_cold_low=15.3449 [C]
T_out_cold_low=15.9128 [C]
DELTAT_cold_low=T_out_cold_low-T_in_cold_low

T_in_hot_low=15.6293 [C]
T_out_hot_low=16.3327 [C]
DELTAT_hot_low=T_out_hot_low-T_in_hot_low
Q_dot_cold_low=Cp_air*m_dot_low*DELTAT_cold_low
Q_dot_hot_low=Cp_air*m_dot_low*DELTAT_hot_low

G_dot_patient_low=Q_dot_hot_low-Q_dot_cold_low

T_in_cold_high=15.3619 [C]
T_out_cold_high=15.8295 [C]
DELTAT_cold_high=T_out_cold_high-T_in_cold_high
T_in_hot_high=15.4646 [C]
T_out_hot_high=16.1174 [C]
DELTAT_hot_high=T_out_hot_high-T_in_hot_high
Q_dot_cold_high=Cp_air*m_dot_high*DELTAT_cold_high
Q_dot_hot_high=Cp_air*m_dot_high*DELTAT_hot_high

G_dot_patient_high=Q_dot_hot_high-Q_dot_cold_high
q_dot_av=(heat_flux_low+heat_flux_high)/2

$\dot{q}_{av} = 7.05\ \mathrm{W/m^2}$

REFERENCES

[1] Malone, D., T. Genuit, J. Tracy, C. Gannon, and L. Napolitano. "Surgical Site Infections: Reanalysis of Risk Factors" *Journal of Surgical Research*, Volume 103, No. 1. pp 89-95. March 2002.

[2] Nichols, R. "Preventing Surgical Site Infections: A Surgeon's Perspective." *Emerging Infectious Diseases*, Volume 7, No. 2, March-April 2001, pp 220-224.

[3] Kirkland, Kathryn, Jane Briggs, Sharon Trivette, William Wilkinson, Daniel Sexton. "The Impact of Surgical-Site Infections in the 1990s: Attributable Mortality, Excess Length of Hospitalization, and Extra Costs." *Infection Control and Hospital Epidemiology*, Volume 20, No. 11. November 1999.

[4] Ryan, K., C. Ray (editors). *Sherris Medical Microbiology*, 4th edition, McGraw Hill, 2004.

[5] Todar, Kenneth. *Staphylococcus*. Updated: 2005. Accessed: 16 August, 2007. <http://www.textbookofbacteriology.net/staph.html>.

[6] Memarzadeh, Farhad and Zheng Jiang. "Effect of Operation Room Geometry and Ventilation System Parameter Variations on the Protection of the Surgical Site." *IAQ 2004: Critical Operations: Supporting the Healing Environment through IAQ Performance Standards.*

[7] Balaras, C., Dascalaki, E., Gaglia, A. *HVAC and indoor thermal conditions in hospital operating rooms*. Energy and Buildings 39 (2007).

[8] Turner, Robert S. "Laminar Air Flow." *The Journal of Bone and Joint Surgery*, Volume 56-a, No. 2, March 1974.

[9] Memarzadeh, Farhad and Andrew Manning. "Comparison of Operating Room Ventilation Systems in the Protection of the Surgical Site." *ASHRAE Transactions 2002,* Volume 108, Part 2. 2002.

[10] Eisman, Louis. *Biology and Human Progress*. Englewood Cliffs, NJ. Prentice Hall, 1972.

[11] Jeter, Sheldon M. and Milton S. Goldman, 2002, "Draft Background and Task Statement for ASHRAE Research on Operating Room Air Distribution," Atlanta, GA, 28 June 2002.

[12] Kähler, C., B. Sammler, J. Kompenhans. "Generation and control of tracer particles for optical flow investigations in air." *Experiments in Fluids 33* (2002) 736–742

[13] Owens Corning. *QuietR Duct Board*. Accessed: 19 October 2007. <http://www.owenscorning.com/comminsul/products.asp?product=271>

[14] ASHRAE, 1985. *ASHRAE Handbook, 1985 Fundamentals Volume*. The American Society of Heating, Refrigerating and Air Conditioning Engineers. Atlanta, GA, pp. 13.14 - 13.15.

[15] Çengel, Yunus A. *Heat Transfer: A Practical Approach*. McGraw-Hill. 1998.

[16] Bryer, D.W. and Pankhurst, R.C., "Pressure-Probe Methods for Determining Wind Speed and Flow Direction", *Her Majesty's Stationary Office*, London, 1971.

[17] Flow Kinetics LLC. "Using A Pitot Static Tube for Velocity and Flow Rate Measurement." Flowmeter Directory. Updated: December 11, 2002. Accessed: 15 October 2007. <http://www.flowmeterdirectory.com/flowmeter_artc/flowmeter_artc_02111201.html>

[18] Adrian, R.J., 1984. "Scattering particle characteristics and their effect on pulsed laser measurements of fluid flow: speckle velocimetry vs. particle image velocimetry." *Applied Optics 23*, pp. 1690-91.

[19] Pickering, J.D. & Halliwell, N.A., 1984. "Speckle photography in fluid flows: signal recovery with two-step processing." *Applied Optics 23*, pp.1128-1129.

[20] Bird, R., W. Stewart, E. Lightfoot. *Transport Phenomena*. Second Edition. John Wiley & Sons, Inc., 2002.

[21] Shih, T., W. Liou, A. Shabbir, Z. Yang, J. Zhu. "A New k-ε Eddy-Viscosity Model for High Reynolds Number Turbulent Flows - Model Development and Validation". *Computers Fluids*, 24(3):227-238, 1995.

[22] FLUENT Inc. FLUENT 6.3 User's Guide. 2006.

[23] Incropera, F., D. DeWitt, T. Bergman, A. Lavine. *Fundamentals of Heat and Mass Transfer*. Sixth Edition. John A. Wiley & Sons, Inc. 2007.

[24] Rhie, C. and W. Chow. "Numerical Study of the Turbulent Flow Past an Airfoil with Trailing Edge Separation." *AIAA Journal*, 21(11):1525-1532, November 1983.

[25] Patankar, S. *Numerical Heat Transfer and Fluid Flow*. Hemisphere, Washington, DC, 1980.

[26] Gebhart, B., J. Yogesh, R. Mahajan, B. Sammakia. *Buoyancy-Induced Flows and Transport*. Hemisphere Publishing Corporation, 1998. New York.

[27] Turner, J. S. *Buoyancy Effects in Fluids*. Cambridge Univerisity Press, 1973. Cambridge.

Additional Resources

Miner, A. L., E. Losina, J. N. Katz, A. H. Fossel, and R. Platt. "Deep Infection After Total Knee Replacement: Impact of Laminar Airflow Systems and Body Exhaust Suits in the Modern Operating Room." *Infection Control and Hospital Epidemiology* 2007, vol. 28, no. 2

Learmonth, I.D. "Prevention of Infection in the 1990's." *Orthopedic Clinic of North America*, 1993; 24(4); 735-741.

Memarzadeh, F. and A. Manning, 2003, "Reducing Risks of Surgery", *ASHRAE Journal*, February, 2003, pp. 28-33.